STATE OF THE CLIMATE IN 2021

GLOBAL OCEANS

G. C. Johnson and R. Lumpkin, Eds.

Special Online Supplement to the *Bulletin of the American Meteorological Society*, Vol. 103, No. 8, August 2022

https://doi.org/10.1175/ BAMS-D-22-0072.1

Corresponding author: Rick Lumpkin / rick.lumpkin@noaa.gov

STATE OF THE CLIMATE IN 2021
Global Oceans

Editors

Jessica Blunden
Tim Boyer

Chapter Editors

Freya Aldred
Peter Bissolli
Kyle R. Clenn
Howard J. Diamond
Matthew L. Druckenmiller
Robert J. H. Dunn
Catherine Ganter
Nadine Gobron
Gregory C. Johnson
Rick Lumpkin
Ademe Mekonnen
John B. Miller
Twila A. Moon
Marilyn N. Raphael
Ahira Sánchez-Lugo
Carl J. Schreck III
Sharon Stammerjohn
Richard L. Thoman
Kate M. Willett
Zhiwei Zhu

Technical Editor

Laura Ohlmann

BAMS Special Editor for Climate

Michael A. Alexander

American Meteorological Society

Cover credit:
"Ocean-Ice-Atmosphere"

Original artwork by Gregory C. Johnson–chapter co-editor. Livestock marker and pencil on oil paper painted from a reference photo by Derek Oyen.

Global Oceans is a chapter from the *State of the Climate in 2021* annual report. This chapter is available from https://doi.org/10.1175/ BAMS-D-22-0072.1. Compiled by NOAA's National Centers for Environmental Information, *State of the Climate in 2021* is based on contributions from scientists from around the world. It provides a detailed update on global climate indicators, notable weather events, and other data collected by environmental monitoring stations and instruments located on land, water, ice, and in space. The full report is available from: https://doi.org/10.1175/2022BAMSStateoftheClimate.1.

How to cite this document:

Citing the complete report:
Blunden, J. and T. Boyer, Eds., 2022: State of the Climate in 2021. *Bull. Amer. Meteor. Soc.*, **103** (8), Si–S465, https://doi.org/10.1175/2022BAMSStateoftheClimate.1.

Citing this chapter:
Johnson, G. C. and R. L. Lumpkin, Eds., 2022: Global Oceans [in "State of the Climate in 2021"]. *Bull. Amer. Meteor. Soc.*, **103** (8), S143–S191, https://doi.org/10.1175/ BAMS-D-22-0072.1.

Citing a section (example):
Franz, B. A., I. Cetinić, M. Gao, D. A. Siegel, and T. K. Westberry, 2022: Global ocean phytoplankton [in "State of the Climate in 2021"]. *Bull. Amer. Meteor. Soc.*, **103** (8), S180–S183, https://doi.org/10.1175/ BAMS-D-22-0072.1.

Editor and Author Affiliations (alphabetical by name)

Boyer, Tim, NOAA/NESDIS National Centers for Environmental Information, Silver Spring, Maryland
Bringas, Francis, NOAA/OAR Atlantic Oceanographic and Meteorological Laboratory, Miami, Florida
Cetinić, Ivona, NASA Goddard Space Flight Center, Greenbelt, Maryland, and Morgan State University, Baltimore, Maryland
Chambers, Don P., College of Marine Science, University of South Florida, St. Petersburg, Florida
Cheng, Lijing, International Center for Climate and Environment Sciences, Institute of Atmospheric Physics, Chinese Academy of Sciences, Beijing, China
Dong, Shenfu, NOAA/OAR Atlantic Oceanographic and Meteorological Laboratory, Miami, Florida
Feely, Richard A., NOAA/OAR Pacific Marine Environmental Laboratory, Seattle, Washington
Fox-Kemper, Baylor, Department of Earth, Environmental, and Planetary Sciences, Brown University, Providence, Rhode Island
Frajka-Williams, Eleanor, National Oceanography Centre, United Kingdom
Franz, Bryan A., NASA Goddard Space Flight Center, Greenbelt, Maryland
Fu, Yao, School of Earth and Atmospheric Sciences, Georgia Institute of Technology, Atlanta, Georgia
Gao, Meng, NASA Goddard Space Flight Center, Greenbelt, Maryland, and Science Systems and Application Inc., Lanham, Maryland
Garg, Jay, Science Systems and Applications, Inc., Hampton, Virginia
Gilson, John, Scripps Institution of Oceanography, University of California San Diego, La Jolla, California
Goni, Gustavo, NOAA/OAR Atlantic Oceanographic and Meteorological Laboratory, Miami, Florida
Hamlington, Benjamin D., Jet Propulsion Laboratory, California Institute of Technology, Pasadena, California
Hewitt, Helene T., Met Office Hadley Centre, Exeter, United Kingdom
Hobbs, William R., Australian Antarctic Program Partnership, Institute for Marine and Antarctic Studies, and Australian Research Council Centre of Excellence for Climate Extremes, University of Tasmania, Hobart, Tasmania
Hu, Zeng-Zhen, NOAA/NWS NCEP Climate Prediction Center, College Park, Maryland
Huang, Boyin, NOAA/NESDIS National Centers for Environmental Information, Asheville, North Carolina
Jevrejeva, Svetlana, National Oceanography Centre, Liverpool, United Kingdom
Johns, William E., Rosenstiel School of Marine and Atmospheric Science, University of Miami, Miami, Florida
Johnson, Gregory C., NOAA/OAR Pacific Marine Environmental Laboratory, Seattle, Washington
Katsunari, Sato, Japan Meteorological Agency, Tokyo, Japan
Kennedy, John J., Met Office Hadley Centre, Exeter, United Kingdom
Kersalé, Marion, Cooperative Institute for Marine and Atmospheric Studies, University of Miami, and NOAA/OAR Atlantic Oceanographic and Meteorological Laboratory, Miami, Florida; currently at Direction Générale de l'Armement, Ingénierie des projets, Paris, France
Killick, Rachel E., Met Office Hadley Centre, Exeter, United Kingdom
Leuliette, Eric, NOAA/NWS NCWCP Laboratory for Satellite Altimetry, College Park, Maryland
Locarnini, Ricardo, NOAA/NESDIS National Centers for Environmental Information, Silver Spring, Maryland
Lozier, M. Susan, School of Earth and Atmospheric Sciences, Georgia Institute of Technology, Atlanta, Georgia
Lumpkin, Rick, NOAA/OAR Atlantic Oceanographic and Meteorological Laboratory, Miami, Florida
Lyman, John M., Cooperative Institute for Marine and Atmospheric Research, University of Hawaii, Honolulu, Hawaii, and NOAA/OAR Pacific Marine Environmental Laboratory, Seattle, Washington
Merrifield, Mark A., Scripps Institution of Oceanography, University of California San Diego, La Jolla, California
Mishonov, Alexey, Earth System Science Interdisciplinary Center/Cooperative Institute for Satellite Earth System Studies Maryland, University of Maryland, College Park, Maryland, and NOAA/NESDIS National Centers for Environmental Information, Silver Spring, Maryland
Mitchum, Gary T., College of Marine Science, University of South Florida, St. Petersburg, Florida
Moat, Ben I., National Oceanography Centre, United Kingdom
Nerem, R. Steven, Colorado Center for Astrodynamics Research, Cooperative Institute for Research in Environmental Sciences, University of Colorado Boulder, Boulder, Colorado
Notz, Dirk, Center for Earth System Research and Sustainability (CEN), Universität Hamburg and Max Planck Institute for Meteorology, Hamburg, Germany
Perez, Renellys C., NOAA/OAR Atlantic Oceanographic and Meteorological Laboratory, Miami, Florida
Purkey, Sarah G., Scripps Institution of Oceanography, University of California San Diego, La Jolla, California
Rayner, Darren, National Oceanography Centre, Southampton, United Kingdom
Reagan, James, NOAA/NESDIS National Centers for Environmental Information, Silver Spring, Maryland
Schmid, Claudia, NOAA/OAR Atlantic Oceanographic and Meteorological Laboratory, Miami, Florida
Siegel, David A., University of California–Santa Barbara, Santa Barbara, California
Smeed, David A., National Oceanography Centre, United Kingdom
Stackhouse, Paul W., NASA Langley Research Center, Hampton, Virginia
Sweet, William, NOAA/NOS Center for Operational Oceanographic Products and Services, Silver Spring, Maryland
Thompson, Philip R., Cooperative Institute for Marine and Atmospheric Research, University of Hawaii, Honolulu, Hawaii
Volkov, Denis L., Cooperative Institute for Marine and Atmospheric Studies, University of Miami, and NOAA/OAR Atlantic Oceanographic and Meteorological Laboratory, Miami, Florida
Wanninkhof, Rik, NOAA/OAR Atlantic Oceanographic and Meteorological Laboratory, Miami, Florida
Weller, Robert A., Woods Hole Oceanographic Institution, Woods Hole, Massachusetts
Wen, Caihong, NOAA/NWS NCEP Climate Prediction Center, College Park, Maryland
Westberry, Toby K., Oregon State University, Corvallis, Oregon
Widlansky, Matthew J., Cooperative Institute for Marine and Atmospheric Research, University of Hawaii, Honolulu, Hawaii
Willis, Josh K., Jet Propulsion Laboratory, California Institute of Technology, Pasadena, California
Yu, Lisan, Woods Hole Oceanographic Institution, Woods Hole, Massachusetts
Zhang, Huai-Min, NOAA/NESDIS National Centers for Environmental Information, Asheville, North Carolina

Editorial and Production Team

Allen, Jessicca, Graphics Support, Cooperative Institute for Satellite Earth System Studies, North Carolina State University, Asheville, North Carolina

Hammer, Gregory, Content Team Lead, Communications and Outreach, NOAA/NESDIS National Centers for Environmental Information, Asheville, North Carolina

Love-Brotak, S. Elizabeth, Lead Graphics Production, NOAA/NESDIS National Centers for Environmental Information, Asheville, North Carolina

Misch, Deborah J., Graphics Support, Innovative Consulting and Management Services, LLC, NOAA/NESDIS National Centers for Environmental Information, Asheville, North Carolina

Ohlmann, Laura, Technical Editor, Innovative Consulting and Management Services, LLC, NOAA/NESDIS National Centers for Environmental Information, Asheville, North Carolina

Riddle, Deborah B., Graphics Support, NOAA/NESDIS National Centers for Environmental Information, Asheville, North Carolina

Veasey, Sara W., Visual Communications Team Lead, Communications and Outreach, NOAA/NESDIS National Centers for Environmental Information, Asheville, North Carolina

3. Table of Contents

*Please refer to Chapter 8 (Relevant datasets and sources) for a list of all climate variables and datasets used in this chapter for analyses, along with their websites for more information and access to the data.

3. GLOBAL OCEANS

G. C. Johnson and R. Lumpkin, Eds.

a. Overview—G. C. Johnson and R. Lumpkin

Patterns of variability in ocean properties are often closely related to large-scale climate pattern indices, and 2021 is no exception. The year 2021 started and ended with La Niña conditions, charmingly dubbed a "double-dip" La Niña. Hence, stronger-than-normal easterly trade winds in the tropical south Pacific drove westward surface current anomalies in the equatorial Pacific; reduced sea surface temperature (SST) and upper ocean heat content in the eastern tropical Pacific; increased sea level, upper ocean heat content, and salinity in the western tropical Pacific; resulted in a rim of anomalously high chlorophyll-*a* (Chl*a*) on the poleward and westward edges of the anomalously cold SST wedge in the eastern equatorial Pacific; and increased precipitation over the Maritime Continent.

The Pacific decadal oscillation remained strongly in a negative phase in 2021, with negative SST and upper ocean heat content anomalies around the eastern and equatorial edges of the North Pacific and positive anomalies in the center associated with low Chl*a* anomalies. The South Pacific exhibited similar patterns. Fresh anomalies in the northeastern Pacific shifted towards the west coast of North America.

The Indian Ocean dipole (IOD) was weakly negative in 2021, with small positive SST anomalies in the east and nearly-average anomalies in the west. Nonetheless, upper ocean heat content was anomalously high in the west and lower in the east, with anomalously high freshwater flux and low sea surface salinities (SSS) in the east, and the opposite pattern in the west, as might be expected during a negative phase of that climate index.

In the Atlantic, the only substantial cold anomaly in SST and upper ocean heat content persisted east of Greenland in 2021, where SSS was also low, all despite the weak winds and strong surface heat flux anomalies into the ocean expected during a negative phase of the North Atlantic Oscillation. These anomalies held throughout much of 2021. An Atlantic and Benguela Niño were both evident, with above-average SST anomalies in the eastern equatorial Atlantic and the west coast of southern Africa. Over much of the rest of the Atlantic, SSTs, upper ocean heat content, and sea level anomalies were above average.

Anthropogenic climate change involves long-term trends, as this year's chapter sidebars emphasize. The sidebars relate some of the latest IPCC ocean-related assessments (including carbon, the section on which is taking a hiatus from our report this year). This chapter estimates that SST increased at a rate of 0.16–0.19°C decade^{-1} from 2000 to 2021, 0–2000-m ocean heat content warmed by 0.57–0.73 W m^{-2} (applied over Earth's surface area) from 1993 to 2021, and global mean sea level increased at a rate of 3.4 ± 0.4 mm yr^{-1} from 1993 to 2021. Global mean SST, which is more subject to interannual variations than ocean heat content and sea level, with values typically reduced during La Niña, was ~0.1°C lower in 2021 than in 2020. However, from 2020 to 2021, annual average ocean heat content from 0 to 2000 dbar increased at a rate of ~0.95 W m^{-2}, and global sea level increased by ~4.9 mm. Both were the highest on record in 2021, and with year-on-year increases substantially exceeding their trend rates of recent decades. A haiku form summary follows:

Ocean climate change,
varies with La Niña, yet,
warming trends are clear.

b. Sea surface temperatures—B. Huang, Z.-Z. Hu, J. J. Kennedy, and H.-M. Zhang

Sea surface temperature (SST) changes and their uncertainties are assessed over the global oceans including seas and large lakes in 2021 using three updated SST products: the Extended Reconstruction Sea-Surface Temperature (ERSSTv5; Huang et al. 2017, 2020), U.K. Met Office Hadley Centre SST (HadSST.4.0.1.0; Kennedy et al. 2019), and Daily Optimum Interpolation SST (DOISST v2.1; Huang et al. 2021a). SST anomalies (SSTAs) are calculated relative to their 1991–2020 baseline period climatologies. The magnitudes of SSTAs are compared against SST standard deviations (std. dev.) for 1991–2020.

Over the global oceans, ERSSTv5 analysis shows that average SSTA decreased from +0.41° ± 0.02°C in 2019 and +0.39° ± 0.01°C in 2020, to +0.29° ± 0.01°C in 2021, due to continued La Niña conditions in the tropical Pacific (detailed later in this section). Here, the uncertainty is estimated by a Student's t-test using a 500-member ensemble based on ERSSTv5 with randomly drawn parameter values within reasonable ranges in the SST reconstructions (Huang et al. 2015, 2020).

Annually averaged SSTAs in 2021 (Fig. 3.1a) have a pattern typical of La Niña in the Pacific: SSTAs were between +0.2°C and +1.0°C in the western North Pacific and western South Pacific and between −0.2°C and −0.5°C in the tropical Pacific east of 165°E, and the eastern South Pacific south of 45°S. SSTAs were between +0.2°C and +1.0°C in most of the North Atlantic and between +0.2°C and +0.5°C in the tropical and South Atlantic. SSTAs were weak (within ±0.2°C) in the Indian Ocean and the coastal Arctic.

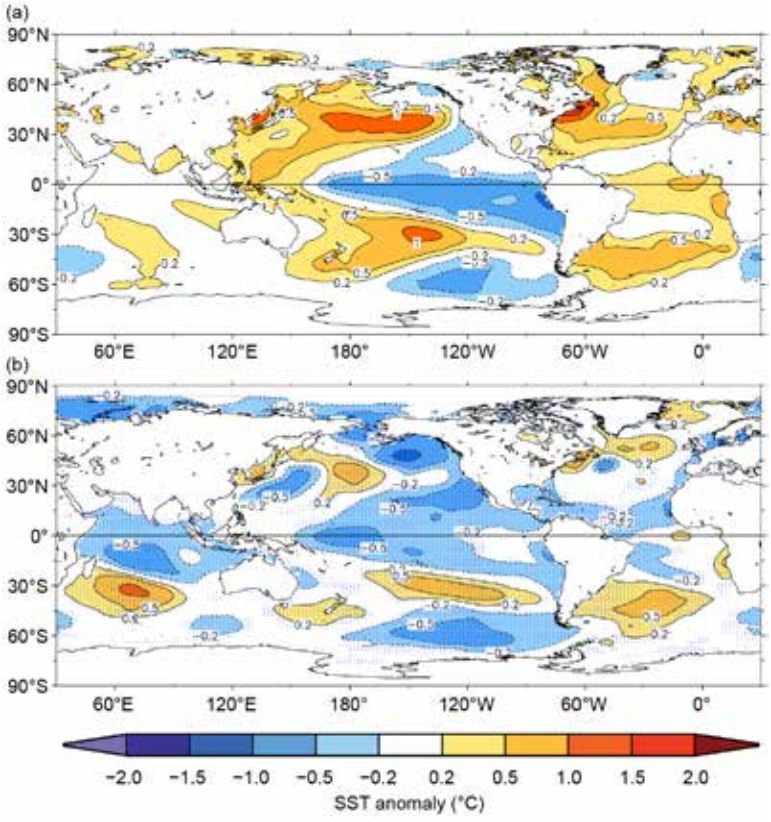

Fig. 3.1. (a) Annually-averaged SSTAs in 2021 and (b) difference of annually-averaged SSTAs between 2021 and 2020. Values (°C) are relative to 1991–2020 climatology and the SSTA difference is significant at 95% confidence in stippled areas.

Averaged SSTs in 2021 compared with 2020 values (Fig. 3.1b) decreased in most of the global oceans by −0.2°C to −0.5°C, except for localized increases in the southern Indian Ocean near 30°S, the central North Pacific near 35°N and 180°, the central South Pacific near 30°S, the South Atlantic near 45°S, and the North Atlantic north of 45°N.

Cooling in the tropical Pacific (Fig. 3.1b) is associated with the evolution of a sustained La Niña, which weakened from November 2020 to May 2021, then reformed in July 2021, and strengthened through the end of the year (Li et al. 2022). The negative SSTAs along the west coast of North America and large positive SSTAs in the central and western North Pacific (Fig. 3.1a) are consistent with the negative phase of the Pacific decadal oscillation (PDO; Mantua and Hare 2002). The PDO index became more negative between 2020 and 2021. The Indian Ocean dipole (IOD) index (Saji et al. 1999), which is correlated with the east–west SSTA gradient in the Indian Ocean, was weakly

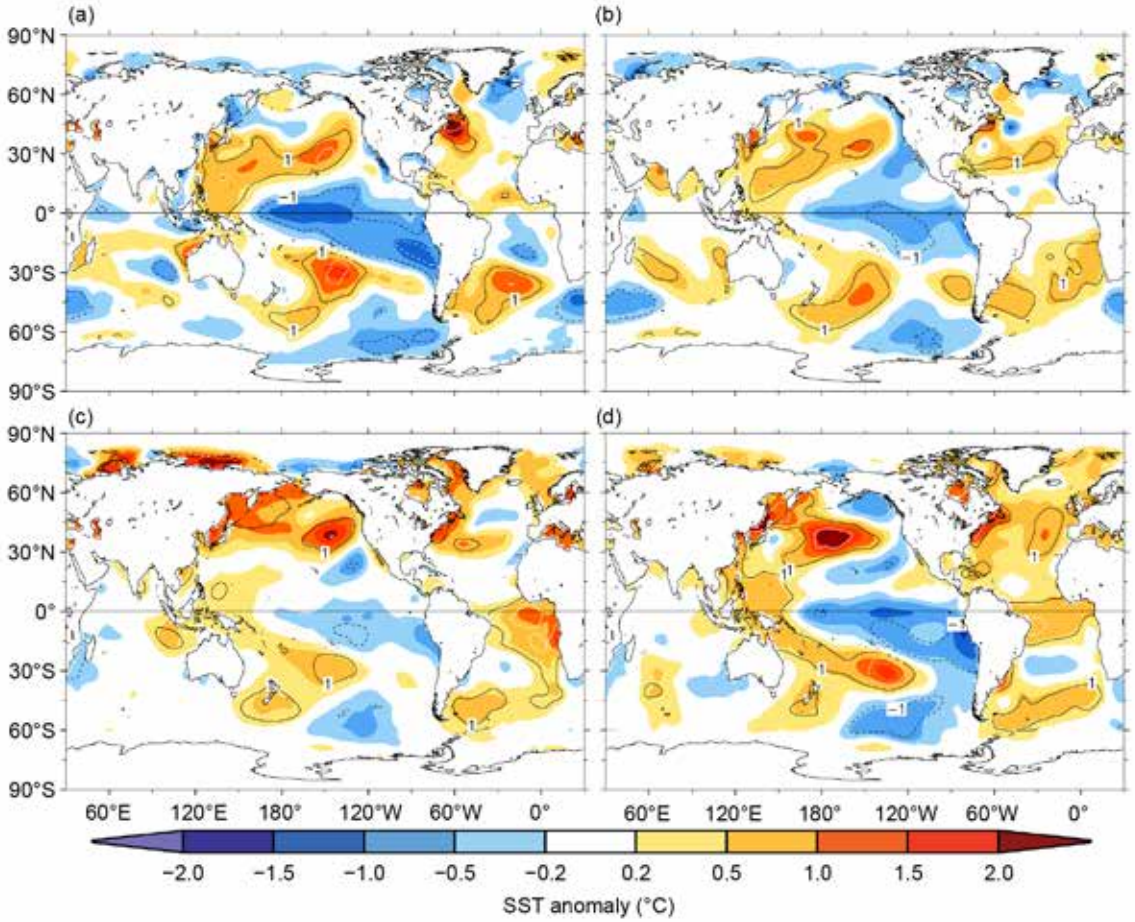

Fig. 3.2. Seasonally-averaged SSTAs of ERSSTv5 (°C, shading) for (a) Dec 2020–Feb 2021, (b) Mar–May 2021, (c) Jun–Aug 2021, and (d) Sep–Nov 2021. Normalized seasonal mean SSTAs relative to seasonal mean standard deviations over 1991–2020 are indicated by contours of –2 (dashed white), –1 (dashed black), 1 (solid black), and 2 (solid white).

negative, but near-neutral (within ±0.5°C) in 2021. The Atlantic Niño index (ATL3; Zebiak 1993), which was associated with the evolution of an Atlantic Niño represented by the positive SSTA in the central-eastern tropical Atlantic in JJA and SON (Figs. 3.2c,d). There was also a substantial positive SSTA off the west coast of southern Africa in JJA, indicating a substantial Benguela Niño (Fig. 3.2c). The overall pattern of SSTAs in the four seasons of 2021 (Fig. 3.2) is similarly reflective of the sustained La Niña and close to that of annually-averaged SSTA in Fig. 3.1. The negative SSTAs in the central-eastern tropical Pacific were strong (–1.0°C to –1.5°C; 1 to 2 std. dev. below average) in DJF and SON, but weaker in JJA. The positive SSTAs in the North and South Pacific were strong (+1.0°C to +1.5°C; 1 to 2 std. dev. above average) in DJF and SON but weaker in JJA. These seasonal SST patterns are directly associated with the weakening La Niña in the first half of 2021 and the emerging second year La Niña in the latter half of 2021, a typical double-dip La Niña event (Okumura and Deser 2010; Hu et al. 2014).

The large positive SSTAs resulted in a series of marine heatwaves in the past few years (Oliver et al. 2017; Perkins-Kirkpatrick et al. 2019; Babcock et al. 2019; Huang et al. 2021b). In 2021, marine heatwaves were observed in the North Pacific in JJA, the regions of the Maritime Continent in JJA and SON, the western boundary of the North Atlantic in JJA, and the Arctic coast of Eurasia in JJA (see section 2b4 for more information on global marine heatwaves).

Long-term warming of global ocean SSTs since the 1950s is clear. The averaged SST reached its record high in 2016 (SSTA of +0.44°C; Figs. 3.3a,b) and decreased slightly after 2016. The averaged SSTAs were +0.39°C in 2020 and +0.29°C in 2021. The linear trend of globally annually-averaged ERSSTv5 SSTAs is 0.10° ± 0.01°C decade^{-1} over 1950–2021 (Table 3.1). The warming remained largest in the tropical Indian Ocean (Fig. 3.3e; 0.14° ± 0.02°C decade^{-1}) and smallest in the North Pacific

(Fig. 3.3d; 0.09° ± 0.04°C decade^{-1}). In contrast, the warming trend was high in the North Pacific (0.36° ± 0.13°C) and low in the tropical Pacific (0.14° ± 0.16°C) in the more recent period (2000–21).

Variations of SSTAs in the North Atlantic (Fig. 3.3f) are evident at interannual and interdecadal time scales and in long-term trends (Li et al. 2020). The interdecadal component is mainly

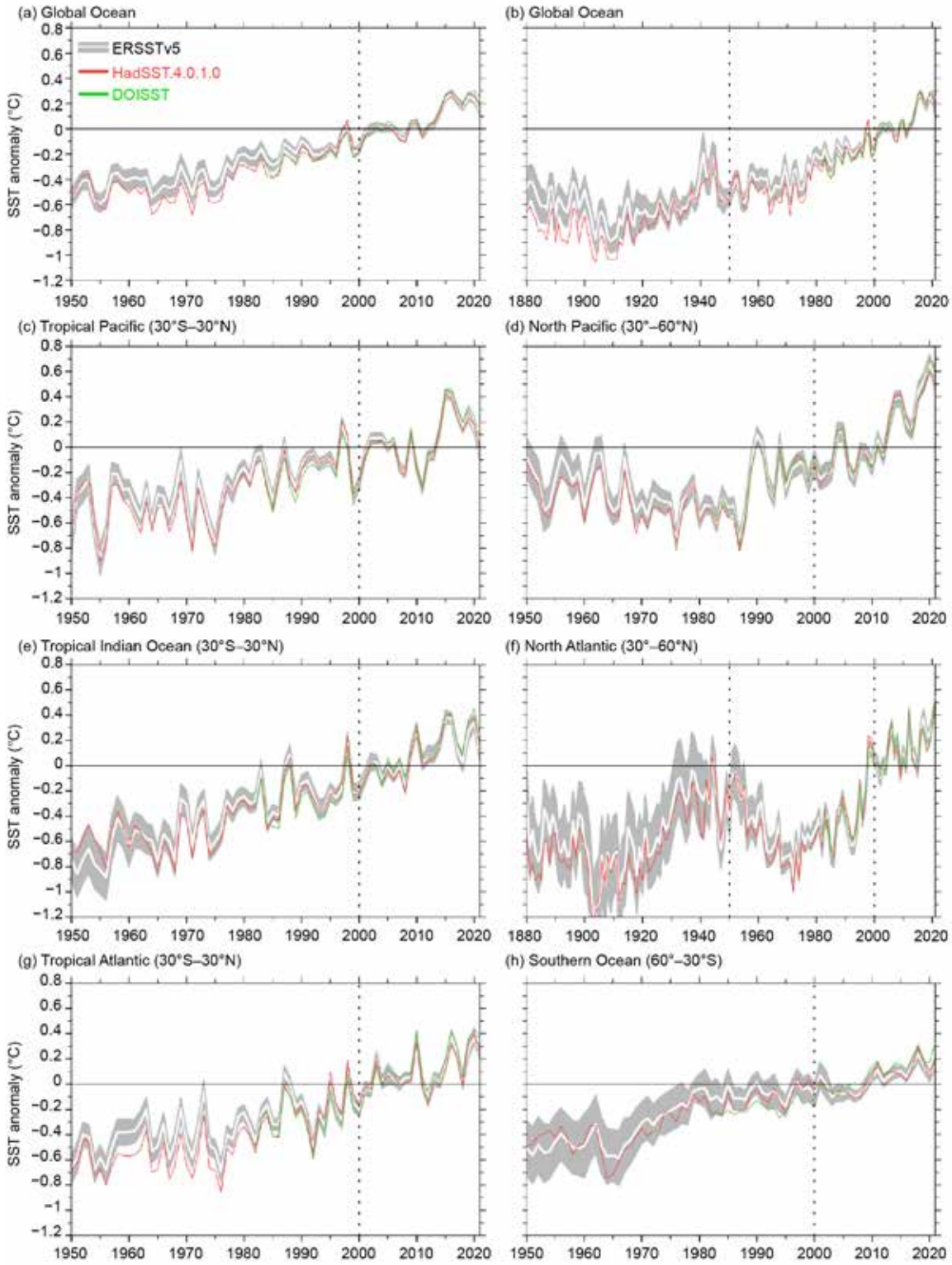

Fig. 3.3. Annually-averaged SSTAs (°C) of ERSSTv5 (solid white) and 2 std. dev. (gray shading) of ERSSTv5, SSTAs of HadSST.4.0.1.0 (solid red), and SSTAs of DOISST v2.1 (solid green) for 1950–2021 except for (b,f). (a) Global, (b) global for 1880–2021, (c) tropical Pacific, (d) North Pacific, (e) tropical Indian, (f) North Atlantic for 1880–2021, (g) tropical Atlantic, and (h) Southern Oceans. The 2 std. dev. envelope was derived from a 500-member ensemble analysis based on ERSSTv5 (Huang et al. 2020) and centered to SSTAs of ERSSTv5. The years 2000 and 1950 in (b) and (f) are indicated by vertical black dotted lines.

Table 3.1. Linear trends (°C decade^{-1}) of annually and regionally averaged SSTAs from ERSSTv5, HadSST4.0.1.0, and DOISST v2.1. Uncertainties at 95% confidence level are estimated accounting for the effective degrees of freedom estimated using lag-1 autocorrelations of annually-averaged SST time series.

Product	Region	2000–2021 (°C decade^{-1})	1950–2021 (°C decade^{-1})
HadSST.4.0.1.0	Global	0.175 ± 0.067	0.117 ± 0.018
DOISST v2.1	Global	0.190 ± 0.057	N/A
ERSSTv5	Global	0.158 ± 0.065	0.102 ± 0.013
ERSSTv5	Tropical Pacific (30°S–30°N)	0.141 ± 0.163	0.099 ± 0.026
ERSSTv5	North Pacific (30°–60°N)	0.364 ± 0.127	0.086 ± 0.040
ERSSTv5	Tropical Indian Ocean (30°S–30°N)	0.184 ± 0.083	0.141 ± 0.017
ERSSTv5	North Atlantic (30°–60°N)	0.158 ± 0.088	0.115 ± 0.046
ERSSTv5	Tropical Atlantic (30°S–30°N)	0.151 ± 0.084	0.112 ± 0.020
ERSSTv5	Southern Ocean (30°–60°S)	0.117 ± 0.053	0.098 ± 0.015

associated with the Atlantic Multidecadal Variability (AMV; Schlesinger and Ramankutty 1994). The AMV may have in turn resulted from some internal and external factors such as aerosol emissions and variations in the strength of the Atlantic meridional overturning circulation (Wang and Yang 2017; Zhang et al. 2019). In the North Atlantic, there were warm periods in the AMV from the 1930s to the 1950s and from the late 1990s to the 2010s, and cold periods before the 1930s and from the 1960s to the early 1990s (Li et al. 2020). In the North Pacific (Fig. 3.3d), SSTAs decreased from the 1960s to the late 1980s, followed by an increase from the later 1980s to the 2010s.

ERSSTv5 SSTAs were compared with those from HadSST.4.0.1.0 and DOISST v2.1. All datasets were annually averaged and interpolated to a 2° × 2° grid for comparison purposes. Departures of DOISST v2.1 and HadSST.4.0.1.0 annual anomalies from those of ERSSTv5 are largely within ±2 std. dev. (gray shading in Fig. 3.3) except in the 1960s–1970s and before the 1910s. The ±2 std. dev. envelope was derived from a 500-member ensemble analysis based on ERSSTv5 (Huang et al. 2020) and centered on SSTAs of ERSSTv5. In the 2000s–2010s, SSTAs were slightly higher in DOISST v2.1 than in ERSSTv5 in the southern, tropical Atlantic, tropical Indian, and tropical Pacific Oceans. As a result, SST trends were slightly higher in DOISST v2.1 over 2000–21 than in ERSSTv5. Previous studies (Huang et al. 2015; Kent et al. 2017) have indicated that these SSTA differences are mostly attributable to the differences in bias corrections applied to ship observations in those products and represent structural uncertainty among different SST products (Kennedy 2013).

c. Ocean heat content—G. C. Johnson, J. M. Lyman, T. Boyer, L. Cheng, J. Gilson, S. Katsunari, R. E. Killick, R. Locarnini, A. Mishonov, S. G. Purkey, and J. Reagan

Owing to increases in greenhouse gases in the atmosphere, the oceans have been warming for decades, storing about 91% of the energy gained by Earth's climate system from 1971 to 2018 (IPCC 2021). Ocean thermal expansion from warming accounted for about 50% of the increase in global average sea level during this same period (IPCC 2021). This warming, while surface intensified, has also been observed from 4000 to 6000-m depth in the coldest, densest bottom waters that sink from the surface to the abyss around Antarctica (Purkey and Johnson 2010). Regional climate patterns such as ENSO effect changes in ocean heating through air–sea heat flux and wind-driven thermocline depth variations. The overall warming trend has become increasingly widespread with time (Johnson and Lyman 2020). This trend has increased the frequency and intensity of marine heat waves (Laufkötter et al. 2020), at least relative to a fixed historical base period. Additionally, warmer upper ocean waters can drive stronger hurricanes (Goni et al. 2009). Ocean warming has also been shown to increase melting rates of ice sheet outlet glaciers around Greenland (Castro de la Guardia et al. 2015) and Antarctica (Schmidtko et al. 2014).

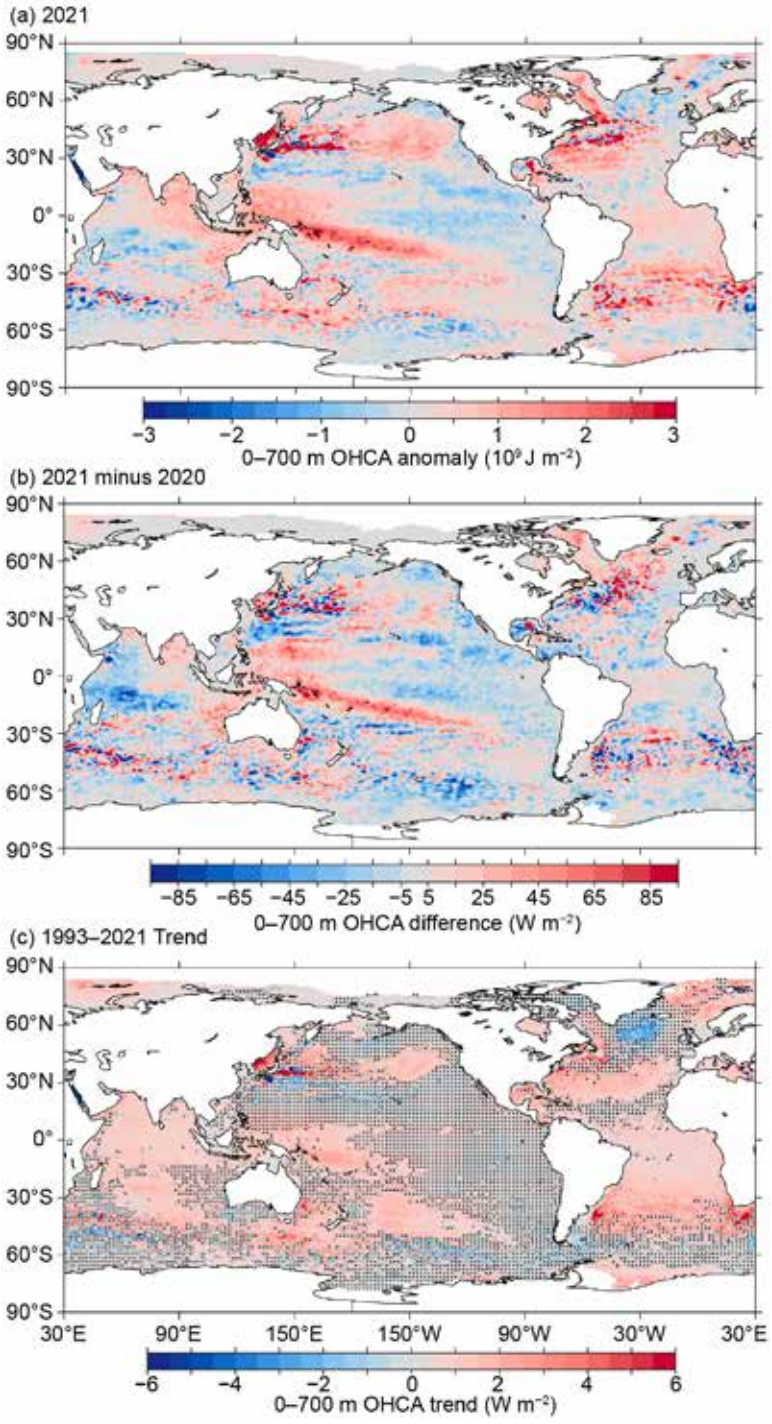

Fig. 3.4. (a) Combined satellite altimeter and in situ ocean temperature data estimate of upper (0–700 m) OHCA (× 10^9 J m^{-2}) for 2021 analyzed following Willis et al. (2004) but using an Argo monthly climatology and displayed relative to a 1993–2021 baseline. (b) 2021 minus 2020 combined estimates of OHCA expressed as a local surface heat flux equivalent (W m^{-2}). For (a) and (b) comparisons, note that 95 W m^{-2} applied over one year results in a 3 × 10^9 J m^{-2} change of OHCA. (c) Linear trend from 1993–2021 of the combined estimates of upper (0–700 m) annual OHCA (W m^{-2}). Areas with statistically insignificant trends are stippled.

Maps of annual (Fig. 3.4) upper (0–700 m) ocean heat content anomaly (OHCA) relative to a 1993–2021 baseline mean are generated from a combination of in situ ocean temperature data and satellite altimetry data following Willis et al. (2004), but using Argo (Riser et al. 2016) data downloaded from an Argo Global Data Assembly Centre in January 2022. Near-global average seasonal temperature anomalies (Fig. 3.5) versus pressure from Argo data (Roemmich and Gilson 2009, updated) since 2004 and in situ global estimates of OHCA (Fig. 3.6) for three pressure layers (0–700 m, 700–2000 m, and 2000–6000 m) from five different research groups are also discussed.

La Niña conditions existed from August 2020 through May 2021, and then again from August 2021 through at least December 2021 (see section 4b). Thus, the 2021 minus 2020 difference of 0–700-m OHCA (Fig. 3.4b) in the tropical Pacific is much like that for 2020 minus 2019 (Johnson et al. 2021), showing a continued increase in the western tropical Pacific and a continued decrease in the central to eastern equatorial Pacific. This pattern exists because anomalously strong easterly trade winds (see Fig. 3.13a) associated with La Niña drive anomalous westward surface currents on the equator (see Figs. 3.18 and 3.19b–d) linked to a shoaling of the equatorial thermocline in the central and eastern equatorial Pacific and a deepening of the western tropical Pacific warm pool, which also shifts warm anomalies from 0–100 dbar down to 100–400 dbar in the global average (Fig. 3.5a). As a result of these prolonged La Niña conditions, the 2021 upper ocean heat content anomalies (Fig. 3.4a) in the equatorial Pacific are negative in the east and positive in the west, with a remarkable warm band extending east-southeastward from about 5°S, 150°E to 25°S, 120°W. Outside of the tropics, higher 2021 minus 2020 differences exist in the centers of the North and South Pacific basins, with some lower values in the eastern portions of the basins consistent with a continued intensified negative phase of

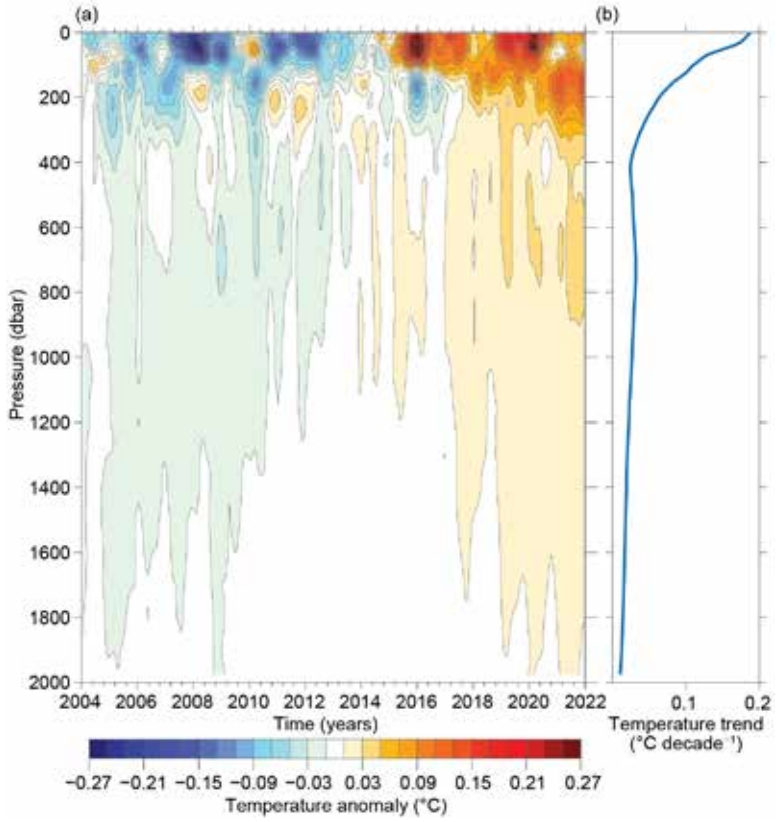

Fig. 3.5. (a) Near-global (65°S–80°N, excluding continental shelves, the Indonesian seas, and the Sea of Okhostk) average monthly ocean temperature anomalies (°C; updated from Roemmich and Gilson [2009]) relative to record-length average monthly values, smoothed with a 5-month Hanning filter and contoured at odd 0.02°C intervals (see color bar) vs. pressure and time. (b) Linear trend of temperature anomalies over time for the length of the record in (a) plotted vs. pressure in °C decade^{-1} (blue line).

the Pacific decadal oscillation index in 2021 (section 3b). The center of the Pacific sector of the Southern Ocean cooled from 2020 to 2021. The Kuroshio extension was anomalously warm in 2021, consistent with a northward shift of that current (see Fig. 3.18), as was the center of the North Pacific basin.

In the Indian Ocean, the 2021 minus 2020 difference of 0–700-m OHCA (Fig. 3.4b) exhibits decreases from about 15°N to 15°S in the western third of the basin, extending into the central third in a band from about 5°S to 15°S. Much of the rest of the basin warmed in 2021 relative to 2020. These changes were consistent with a weakly negative phase of the Indian Ocean dipole index for much of 2021. Upper OHCA values for 2021 were above the 1993–2021 mean in much of the Indian Ocean (Fig. 3.4a), but a band of values below the mean was evident in the western two-thirds of the basin from about 5°S to 15°S.

The 2021 minus 2020 differences of 0–700-m OHCA (Fig. 3.4b) in the Atlantic Ocean are positive in the Labrador Sea, the Irminger Sea, much of the Greenland Sea, and much of the North Atlantic Current. The equatorial Atlantic region also exhibited a warming, but weaker than the northern warming over this time period. The Caribbean Sea and Gulf of Mexico exhibited mostly cooling, except in the region of the Loop Current in the Gulf, which warmed substantially. In 2021, much of the Atlantic Ocean exhibited upper OHCA above the 1993–2021 average (Fig. 3.4a) with the main exception being cooler-than-average conditions southeast of Greenland and in the center of the Greenland-Iceland-Norwegian Seas. The western North Atlantic and southern portions of the subtropical South Atlantic warm anomalies were especially large in 2021.

As expected, the large-scale statistically significant (Fig. 3.4c) regional patterns in the 1993–2021 local linear trends of upper OHCA were quite similar to those from 1993–2020 (Johnson et al. 2021) and earlier reports. Warming trends that were statistically significantly greater than zero occupy 49% of the global ocean surface area, including much of the Indian Ocean and South Atlantic Ocean, the subtropical North Atlantic, the center of the North Pacific, and the western South Pacific. The western boundary current extensions all exhibited strong warming trends, which may be attributed to their intensification and poleward shift under greenhouse gas warming (Wu et al. 2012; Yang et al. 2016). Statistically significant cooling trends occupied only 3% of the ocean area, with the most prominent region being southeast of Greenland in the North Atlantic, linked to a decrease in the Atlantic meridional overturning circulation (AMOC; Dima and Lohmann 2010; Caesar et al. 2018) as well as aerosol-shortwave-cloud feedbacks (Josey et al. 2018). In general, the longer the period over which these trends are estimated, the more of the ocean surface area warms and the less of it cools at statistically significant rates (Johnson and Lyman 2020).

Near-global average seasonal temperature anomalies (Fig. 3.5a) from the start of 2004 through the end of 2021 exhibit a clear surface-intensified, record-length warming trend (Fig. 3.5b) that approaches +0.2°C decade^{-1} at the surface, matching well with SST trends from 2001 to 2021 (section 3b). This trend generally decreases with increasing pressure (depth), but is positive from the surface to the 2000-dbar target maximum sampling pressure of Core Argo. The reduction of warm anomalies during 2020 and 2021 in the upper 100 dbar, with increases in warming from 100 to 400 dbar, is consistent with the presence of La Niña conditions in 2020 and 2021. The opposite pattern is evident during El Niño years (e.g., 2009/10, 2015/16, and 2018/19).

As noted in previous reports, the analysis is extended back in time from the Argo period to 1993 and expanded to examine greater depths, using sparser, more heterogeneous historical data collected mostly from ships (e.g., Abraham et al. 2013). The different estimates of annual globally integrated 0–700-m OHCA (Fig. 3.6a) all reveal a large increase since 1993, with all of the five analyses reporting 2021 as a record high. All five of the globally integrated 700–2000-m OCHA annual analyses (Fig. 3.6b) also report 2021 as a record high, and the long-term warming trend in this layer is also clear. The water column from 0–700 m and 700–2000 m gained 10.2 (±1.6) and 5.1 (±1.1) ZJ, respectively (means and standard deviations given) from 2020 to 2021. Causes of differences among estimates are discussed in Johnson et al. (2015).

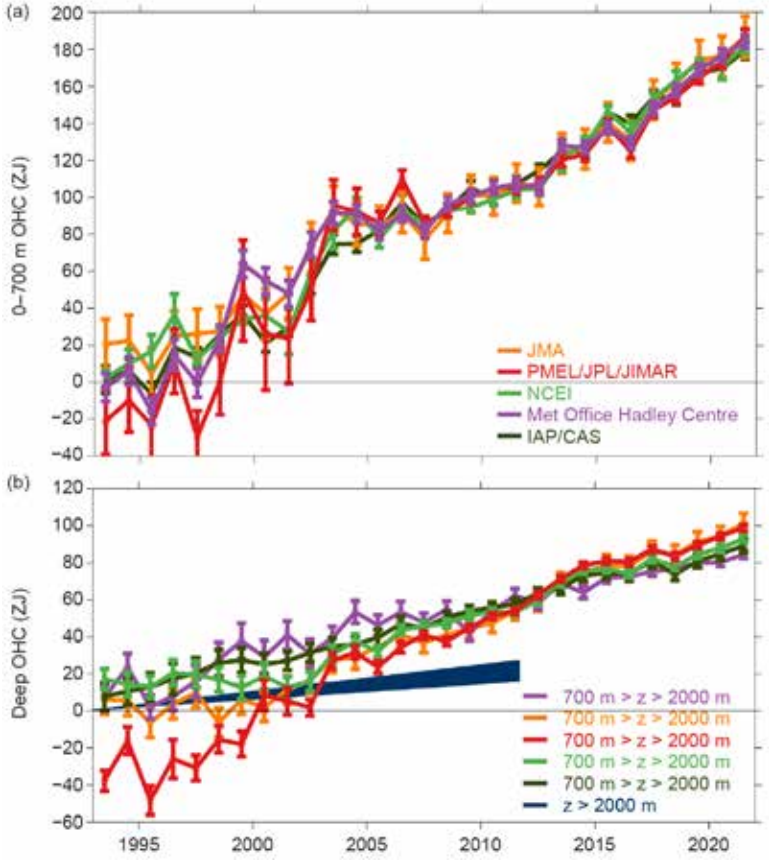

Fig. 3.6. (a) Annual average global integrals of in situ estimates of upper (0–700 m) OHCA (ZJ; 1 ZJ = 10^{21} J) for 1993–2021 with standard errors of the mean. The MRI/JMA estimate is an update of Ishii et al. (2017). The PMEL/JPL/JIMAR estimate is an update and refinement of Lyman and Johnson (2014). The Met Office Hadley Centre estimate is computed from gridded monthly temperature anomalies (relative to 1950–2019) following Palmer et al. (2007) and Good et al. (2013). Both the PMEL and Met Office estimates use Cheng et al. (2014) XBT corrections and Gouretski and Cheng (2020) MBT corrections. The NCEI estimate follows Levitus et al. (2012). The IAP/CAP estimate is reported in Cheng et al. (2021). See Johnson et al. (2014) for details on uncertainties, methods, and datasets. For comparison, all estimates have been individually offset (vertically on the plot), first to their individual 2005–21 means (the best sampled time period), and then to their collective 1993 mean. (b) Annual average global integrals of in situ estimates of intermediate (700–2000 m) OHCA for 1993–2021 with standard errors of the mean, and a long-term trend with one standard error uncertainty shown from September 1992 to January 2012 for deep and abyssal (z > 2000 m) OHCA following Purkey and Johnson (2010) but updated using all repeat hydrographic section data available from https://cchdo.ucsd.edu/ as of Jan 2022

The estimated linear rates of heat gain for each of the five global integral estimates of 0–700-m OHCA from 1993 through 2021 (Fig. 3.6a) range from 0.37 (±0.05) to 0.44 (±0.12) W m^{-2} applied over the surface area of Earth (Table 3.2), rather than the surface area of the ocean, the better to compare to top-of-the-atmosphere energy imbalance (e.g., Loeb et al. 2021). These results are not much different from those in previous reports, although with an increasing record length, trend uncertainties tend to decrease and differences among analyses tend to grow smaller. Linear trends from the 700–2000-m layer over the same time period range from 0.17 (±0.03) to 0.29 (±0.03) W m^{-2}.

Table 3.2. Trends of ocean heat content increase (in W m^{-2} applied over the 5.1×10^{14} m^2 surface area of Earth) from six different research groups over three depth ranges (see Fig. 3.6 for details). For the 0–700-m and 700–2000-m depth ranges, estimates cover 1993–2021, with 5%–95% uncertainties based on the residuals taking their temporal correlation into account when estimating degrees of freedom (Von Storch and Zwiers 1999). The 2000–6000-m depth range estimate, an update of Purkey and Johnson (2010), uses data from 1981 to 2021, having a global average start and end date of September 1992 to January 2012, again with 5%–95% uncertainty.

	Global ocean heat content trends (W m^{-2}) for three depth ranges		
Research Group	0–700 m	700–2000 m	2000–6000 m
MRI/JMA	0.37 ± 0.05	0.24 ± 0.04	
PMEL/JPL/JIMAR	0.44 ± 0.12	0.29 ± 0.03	
NCEI	0.39 ± 0.05	0.19 ± 0.05	
Met Office Hadley Centre	0.40 ± 0.08	0.17 ± 0.03	
IAP/CAS	0.41 ± 0.04	0.18 ± 0.01	
Purkey and Johnson			0.07 ± 0.03

Trends in the 0–700-m layer all agree within their 5%–95% confidence intervals. However, as noted in previous reports, the trends in the 700–2000-m layer, which is quite sparsely sampled prior to the start of the Argo era (circa 2005), do not all overlap within uncertainties. Different methods for dealing with under-sampled regions likely cause this disagreement. Using repeat hydrographic section data collected from 1981 to 2021 to update the estimate of Purkey and Johnson (2010) for 2000–6000 m, the linear trend is 0.07 (±0.03) W m^{-2} from September 1992 to January 2012 (these dates are global average times of first and last sampling of the sections). Summing the three layers (despite their slightly different time periods as given above), the full-depth ocean heat gain rate ranges from 0.64 to 0.80 W m^{-2} applied to Earth's entire surface.

d. Salinity—G. C. Johnson, J. Reagan, J. M. Lyman, T. Boyer, C. Schmid, and R. Locarnini

1) INTRODUCTION

Salinity is the mass of dissolved salts per unit mass of sea water, and a nearly conservative tracer. Climatological mean salinity values fall below 28.0 or above 37.4 g kg^{-1} for only 1% of the ocean surface area each. Temperature and salinity are used in tandem to identify water masses and assess water mass mixing throughout the global ocean. Surface mixed layer salinity is modified through evaporation, precipitation, advection, mixing, entrainment, river runoff, and ice freezing or melting (Ren et al. 2011; Yu et al. 2011). Large-scale salinity patterns generally reflect large-scale evaporation and precipitation patterns (Wüst 1936), with precipitation-dominated regions (e.g., the ITCZ) exhibiting low values and evaporation-dominated regions (e.g., subtropics) exhibiting high values. Roughly 86% of global evaporation and 78% of global precipitation occurs over the ocean (Baumgartner and Reichel 1975; Schmitt 1995). Changes in salinity have been used to estimate changes in the hydrological cycle (e.g., Durack et al. 2012; Skliris et al. 2014, 2016).

Seawater density is a function of temperature, salinity, and pressure. Thus, any changes to salinity distributions potentially impact a water parcel's ability to sink. Relatively cold, salty, dense waters that sink at high latitudes comprise the lower limb of the global thermohaline circulation (Gordon 1986; Broecker 1991). Numerical model experiments have shown that the Atlantic meridional overturning circulation (section 3h) generally weakens in response to surface freshening (e.g., Stouffer et al. 2006; Smith and Gregory 2009). It is therefore critical that surface and subsurface salinity changes are monitored since they can act as a proxy for changes in the hydrological cycle and can impact the global ocean circulation.

To investigate interannual changes of subsurface salinity, all available salinity profile data are quality controlled following Boyer et al. (2018) and then used to derive 1° monthly mean gridded salinity anomalies relative to a long-term monthly mean for years 1955–2017 (World Ocean Atlas 2018, WOA18; Zweng et al. 2018) at standard depths from the surface to 2000 m (Boyer et al. 2018). In recent years, the largest source of salinity profiles is the profiling floats of the Argo program (Riser et al. 2016). These data are a mix of real-time (preliminary) and delayed-mode (scientific quality controlled) observations. Hence, the estimates presented here may be subject to instrument biases such as a positive salinity drift identified in a subset of Argo CTDs, and will change after all data are subjected to scientific quality control. The SSS analysis relies on Argo data downloaded in January 2022, with annual anomaly maps relative to a seasonal climatology generated following Johnson and Lyman (2012), as well as monthly maps of bulk (as opposed to skin) SSS data from the Blended Analysis of Surface Salinity (BASS; Xie et al. 2014). BASS blends in situ SSS data with data from the *Aquarius* (Le Vine et al. 2014; mission ended in June 2015), Soil Moisture and Ocean Salinity (SMOS; Font et al. 2013), and the Soil Moisture Active Passive (SMAP; Fore et al. 2016) satellite missions. Despite the larger uncertainties of satellite data relative to Argo data, their higher spatial and temporal sampling allows higher spatial and temporal resolution maps than are possible using in situ data alone at present. All salinity values used in this section are reported as observed, on the dimensionless Practical Salinity Scale-78 (PSS-78; Fofonoff and Lewis 1979).

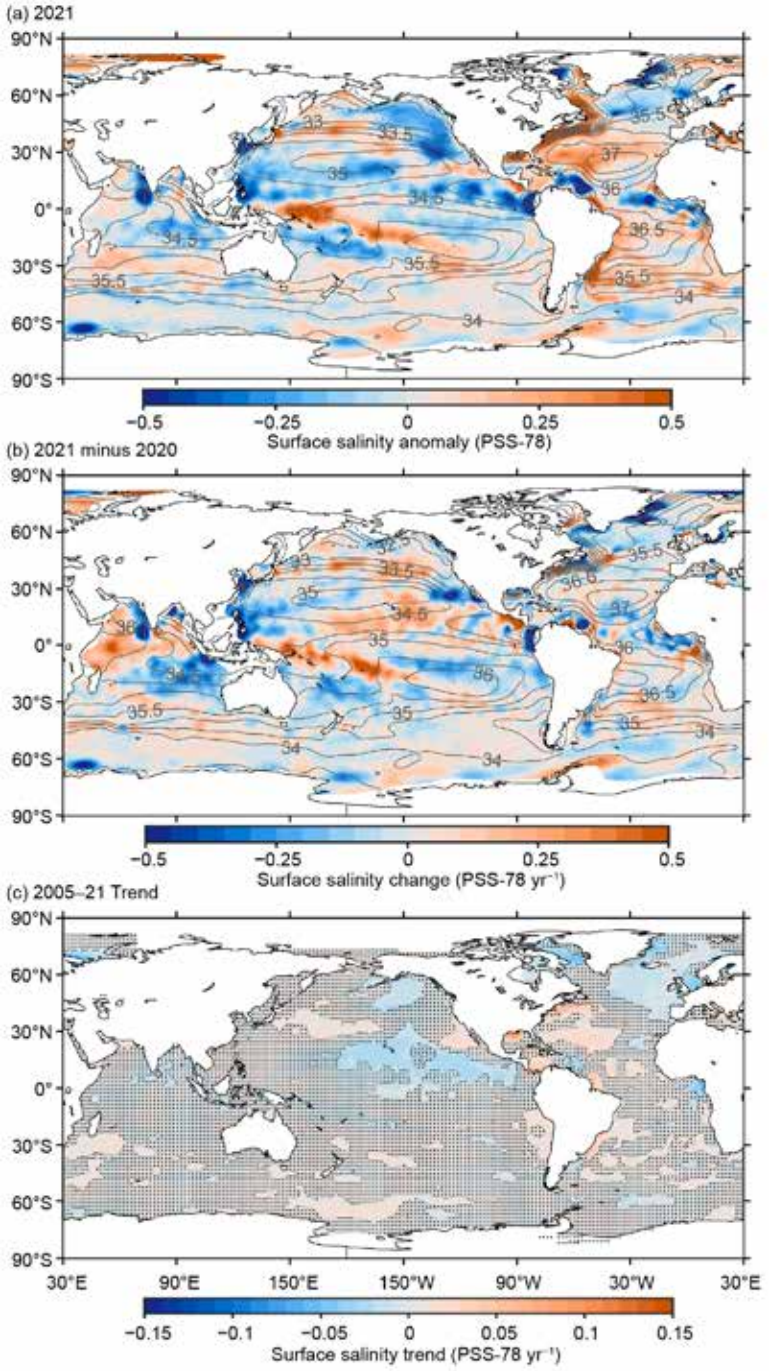

Fig. 3.7. (a) Map of the 2021 annual surface salinity anomaly (colors, PSS-78) with respect to monthly climatological 1955–2012 salinity fields from WOA13v2 (yearly average, gray contours at 0.5 intervals, PSS-78). (b) Difference of 2021 and 2020 surface salinity maps (colors, PSS-78 yr^{-1}). White ocean areas are too data-poor (retaining < 80% of a large-scale signal) to map. (c) Map of local linear trends estimated from annual surface salinity anomalies for 2005–21 (colors, PSS-78 yr^{-1}). Areas with statistically insignificant trends at 5%–95% confidence are stippled. All maps are made using Argo data.

2) SEA SURFACE SALINITY—

G. C. Johnson and J. M. Lyman

As noted in previous reports, since salinity has no direct feedback to the atmosphere, large-scale SSS anomalies can be quite persistent. (In contrast, SST anomalies are often damped by air–sea heat exchange.) For instance, the large fresh SSS anomaly in 2021 in the northeastern Pacific (Fig. 3.7a) began around 2016 in the central North Pacific (near 40°N between Hawaii and the Aleutian

Islands), shifting slowly eastward and then southward over time (see previous *State of the Climate* reports), in the same direction as the prevailing currents. This upper ocean fresh anomaly increased density stratification, a condition conducive to prolonging and amplifying a marine heatwave in the region that started in 2019 (Scannell et al. 2020), and persisted through much of 2021 (see Figs. 3.2, 3.4a). Elsewhere in the Pacific Ocean, the 2021 fresh SSS anomalies (Fig. 3.7a) observed over much of the ITCZ and SPCZ (South Pacific Convergence Zone) and extending north of Hawaii in the central Pacific began around 2015 (see previous *State of the Climate* reports) but were generally somewhat reduced from previous years in 2021. In contrast, the salty anomalies along and just south of the equator in the western and central Pacific, respectively, strengthened in 2021 (Figs. 3.7a,b), again owing to the westward migration of the eastern edge of the fresh pool with the persistence of La Niña in much of 2021 (section 4b), linked to the anomalous westward currents across the equator in 2021 (Fig. 3.18a) as well as westward shifts in precipitation in the region (Fig. 3.12d).

There was mostly freshening of SSS from 2020 to 2021 in the tropical Atlantic ITCZ, salinification over much of the South Atlantic, and freshening in much of the Labrador Sea and off the east coast of Greenland (Fig. 3.7b). In the Atlantic in 2021, as in many previous years, the relatively fresh regions (the subpolar North Atlantic, subantarctic South Atlantic, under the ITCZ, and off northern Brazil and Venezuela) were fresher than climatology, and the relatively saltier regions (the subtropics) were saltier than climatology (Fig. 3.7a). In 2021 conditions were anomalously salty offshore of the east coast of North America from the Gulf of Mexico to Labrador as well as offshore of much of the South American east coast.

Freshening in the southeastern tropical Indian Ocean and salinification in much of the north and west from 2020 to 2021 (Fig. 3.7b) is consistent with a weak negative Indian Ocean dipole index for much of 2021, with increased precipitation in the southeast and reduced precipitation to the north and west (see Fig. 3.12). A pronounced freshening west of India from 2020 to 2021 left that region fresher than climatology in 2021 (Fig. 3.7a).

As discussed in previous reports, in a warming climate the atmosphere can hold more water, leading to expectations of more evaporation in regions where evaporation is dominant over

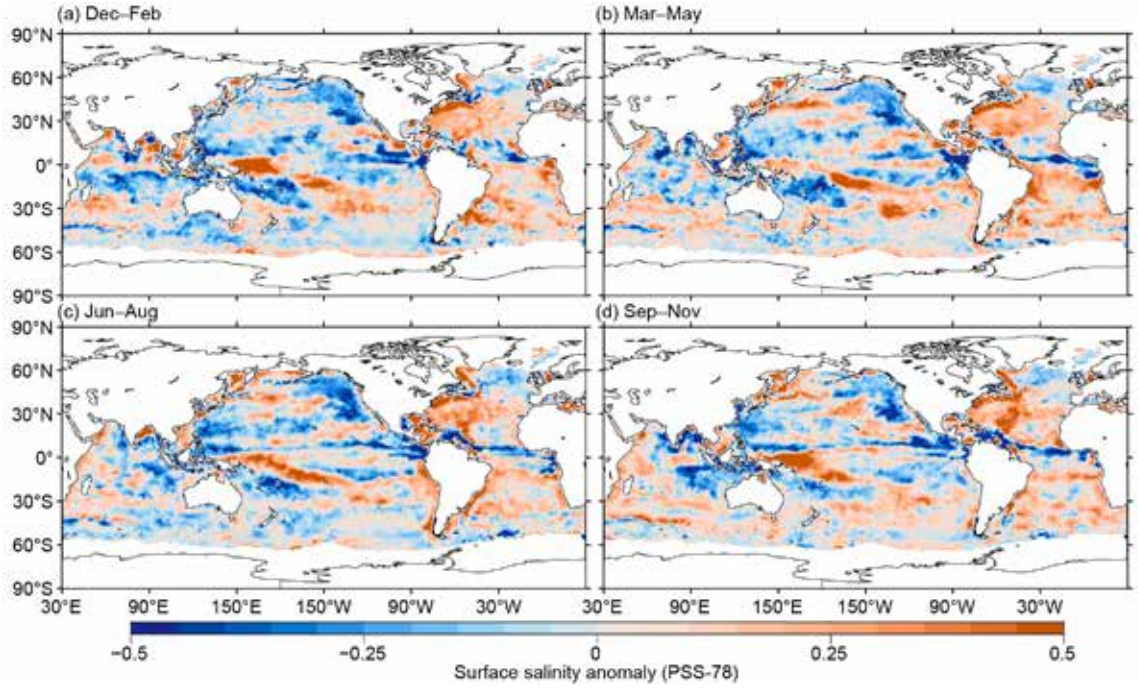

Fig. 3.8. Seasonal maps of SSS anomalies (colors) from monthly blended maps of satellite and in situ salinity data (BASS; Xie et al. 2014) relative to monthly climatological 1955–2012 salinity fields from WOA13v2 for (a) Dec 2020–Feb 2021, (b) Mar–May 2021, (c) Jun–Aug 2021, and (d) Sep–Nov 2021. Areas with maximum monthly errors exceeding 10 PSS-78 are left white.

precipitation and more precipitation where precipitation exceeds evaporation (Held and Soden 2006; Durack and Wijffels 2010). In the ocean this translates roughly to "Salty gets saltier and fresh gets fresher." This pattern has been evident in *State of the Climate* reports going back as far as 2006, the first year of the salinity section. In 2021 this pattern held (Fig. 3.7a), with salty SSS anomalies in most of the subtropical salinity maxima and fresh SSS anomalies in the eastern subpolar North Pacific and North Atlantic, as well as the ITCZs of the Pacific and Atlantic. The 2005–21 SSS trends (Fig. 3.7c) reflect this pattern to some extent as well, with statistically significant (unstippled areas) freshening trends evident in the eastern subpolar North Pacific and North Atlantic, the Pacific ITCZ, and the Gulf of Guinea, as well as statistically significant salty trends in parts of the subtropics in all basins.

In 2021, the seasonal BASS (Xie et al. 2014) SSS anomalies (Fig. 3.8) show the seasonal progressions of many of the features in the annual anomaly map using Argo data alone (Fig. 3.7a), and with higher spatial resolution, albeit with somewhat less accuracy. Iceberg A-68A drifted from the Weddell Sea northward and approached South Georgia Island in late 2020 and had broken up and nearly completely melted by April 2021. It left behind a fresh SSS anomaly near South Georgia Island (54°S, 37°W) in December 2020–February 2021 that drifted slowly eastward during 2021 and was still visible, although diminished somewhat, in September–November 2021 (Fig. 3.8).

3) SUBSURFACE SALINITY—J. Reagan, T. Boyer, C. Schmid, and R. Locarnini

For the second straight year, all monthly basin-averaged salinity anomalies for 0–1000-m depth in the Atlantic were positive in 2021 (Fig. 3.9a). Salinity anomalies > 0.01 reached from 300 to 500 m during 2012–16, but have increased with depth since, reaching 800 m in 2021. Larger salinity

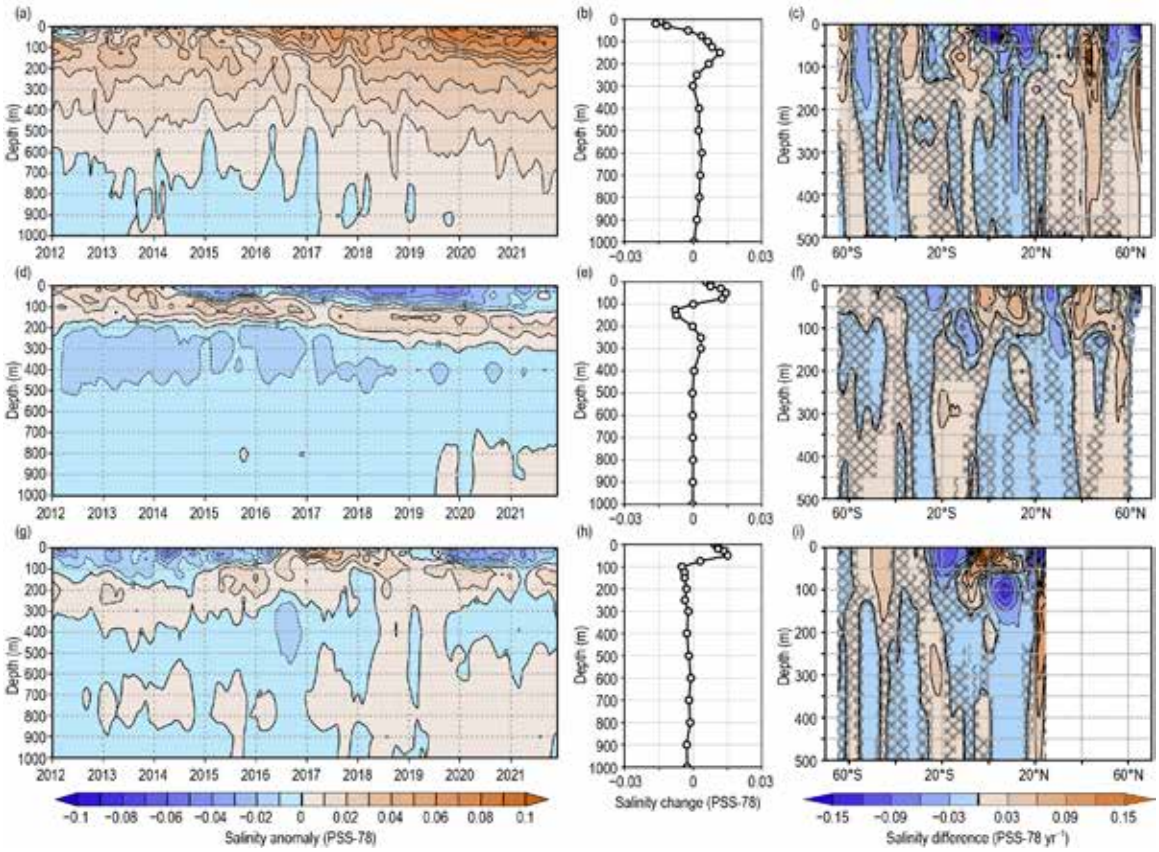

Fig. 3.9. Average monthly salinity anomalies from 0–1000 m for 2012–21 for the (a) Atlantic, (d) Pacific, and (g) Indian Oceans. Change in salinity from 2020 to 2021 for the (b) Atlantic, (e) Pacific, and (h) Indian Oceans. Change in the 0–500 m zonal-average salinity from 2020 to 2021 in the (c) Atlantic, (f) Pacific, and (i) Indian Oceans with areas of statistically insignificant change, defined as < ±1 std. dev. and calculated from all year-to-year changes between 2005 and 2021, stippled in dark gray. Data were smoothed using a 3-month running mean. Anomalies are relative to the long-term (1955–2017) WOA18 monthly salinity climatology (Zweng et al. 2018).

anomalies have followed suit and have also deepened since 2017. This increase is reflected in the 2020 to 2021 Atlantic salinity changes (Fig. 3.9b), with the Atlantic increasing in salinity from 75 to 1000 m. The maximum increase of ~0.013 at 150 m coincides with an increase in zonally-averaged salinity between 2020 and 2021 at 43°N and 65°N (Fig. 3.9c). In contrast to what was seen between 2019 and 2020 (Reagan et al. 2021), the upper 50 m of the Atlantic freshened by ~−0.015 (Fig. 3.9b) from 2020 to 2021, which is largely a result of freshening just north of the equator and north of 50°N (Fig. 3.9c).

The basin-averaged monthly salinity anomalies from 0–1000 m in the Pacific (Fig. 3.9d) have followed a similar pattern since 2015 (see Reagan et al. 2020, 2021). The changes from 2020 to 2021 (Fig. 3.9e) are largely similar to the changes from 2019 to 2020 (Reagan et al. 2021), with increasing salinity in the upper 100 m (max of ~0.015 at 50 m) and freshening from 100 to 200 m (max of ~−0.0075 at 125 m). The near-surface salinification is visible in the 2020 to 2021 zonally-averaged Pacific salinity change (Fig. 3.9f), with increases (> 0.03) confined to the upper 100 m between 5°S and 20°N and between 35°N and 43°N with the tropical region's salinification likely due to a precipitation decrease (Fig. 3.12) associated with transitioning from a neutral (early 2020) to a La Niña phase (late 2020 into 2021) in the Pacific. The freshening from 100 to 200 m (Fig. 3.9e) is primarily associated with the subsurface freshening < ~−0.03 at 10°S and 30°N (Fig. 3.9f).

The 2021 0–1000-m Indian basin-average monthly salinity anomalies look similar to those in 2020 (Fig. 3.9g; Reagan et al. 2021). However, unlike the 2019 to 2020 freshening that took place in the upper 100 m (see Fig. 3.9h in Reagan et al. 2021), there was salinification from 2020 to 2021 in this layer (Fig. 3.9h), which appears to be related to the strong (> 0.06) near-surface equatorial salinification (Figs. 3.7b and 3.9i). On the other hand, for depths 100 to 1000 m, there was very weak (> −0.005) freshening (Fig. 3.9h) from 2020 to 2021.

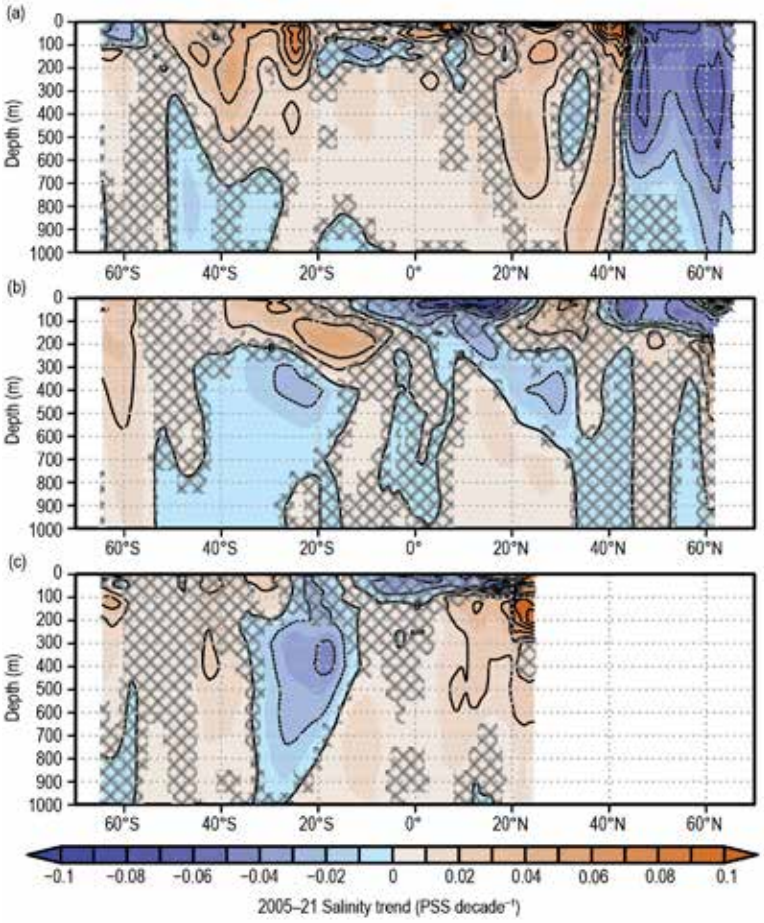

Fig. 3.10. The linear trend of zonally-averaged salinity from 2005 to 2021 over the upper 1000 m for the (a) Atlantic, (b) Pacific, and (c) Indian Oceans. The salinity trend is per decade and computed using least squares regression. Areas that are stippled in dark gray are not significant at the 95% confidence interval. SST differences are significant at 95% level in stippled areas.

Zonally-averaged 2005–21 salinity trends, with 95% confidence intervals, reveal that salinification trends dominate much of the Atlantic south of 45°N (Fig. 3.10a). There is a broad area of salinification (> 0.02 decade^{-1}) from ~50°S to 20°S, extending from the surface to 500 m at 38°S. There are pockets of strong near-surface salinification trends (> 0.08 decade^{-1}) at 7°N, 27°N, and 40°N, with the latter two locations having salinification trends extending down to 750 and 1000 m, respectively. Despite basin-wide salinification trends from 2005 to 2020 (see Fig. 3.10a in Reagan et al. 2021), which are driven by both large-scale and intense small-scale salinification trends between 50°S and 45°N, a freshening trend from 0 to 1000 m in the subpolar North Atlantic between 45°N and 65°N from 2005 to 2021 is observed (Fig. 3.10a). This subpolar North Atlantic freshening may increase stratification and decrease density (Gelderloos et al.

2012), which may affect overflow waters and the deep western boundary current, thus decreasing the Atlantic meridional overturning circulation.

The positive and negative zonally-averaged salinity trends are more randomly distributed in the Pacific than the Atlantic (Fig. 3.10b). Salinification trends (> 0.02 decade^{-1}) are primarily found in the South Pacific centered at 60°S to a depth of 550 m, and at the surface at 30°S extending downward and equatorward to ~300 m at 10°S. Near-surface freshening trends (< −0.06 decade^{-1}) are found between the equator and 20°N, as well as between 45°N and 60°N.

Finally, the Indian Ocean's zonally-averaged salinity trends from 2005 to 2021 primarily involve the subsurface. The only region that experienced a freshening trend is between 200 and 900 m, centered at 18°S and 350 m. Salinification trends dominate much of the subsurface centered at ~65°S, 40°S, and 22°N, with the latter exhibiting trends greater than 0.10 decade^{-1} at 200 m (Fig. 3.10c).

e. Global ocean heat, freshwater, and momentum fluxes—L. Yu, P. W. Stackhouse, J. Garg, C. Wen, and R. A. Weller

The ocean and the atmosphere communicate physically via interfacial exchanges of heat, freshwater, and momentum. Most of the shortwave radiation (SW) absorbed by the ocean's surface is returned to the atmosphere by three processes: longwave radiation (LW), turbulent heat loss by evaporation (latent heat flux, or LH), and by conduction (sensible heat flux, or SH). The residual heat is stored in the warming ocean and transported by the ocean's circulation, forced primarily by the momentum transferred to the ocean by wind stress. Evaporation connects heat and moisture transfers; and the latter, together with precipitation and continental runoff, determines the local surface freshwater flux. Identifying changes in air–sea fluxes is essential to deciphering observed changes in ocean circulation and its transport of heat and salt from the tropics to the poles.

Here we examine air–sea heat fluxes, freshwater fluxes, and wind stress in 2021 and their relationships with ocean surface variables. Anomalies for 2021 are relative to a 2001–15 climatology, which spans from the first full year available, 2001, to 2015, just before the strong El Niño that followed. The net surface heat flux, Q_{net}, is the sum of four terms: SW+LW+LH+SH. The net surface freshwater flux into the ocean (neglecting riverine and glacial fluxes from land) is precipitation (P) minus evaporation (E), or the $P - E$ flux. Wind stress is computed from satellite wind retrievals using the bulk parameterization COARE version 3.5 (Fairall et al. 2003). The production of the global maps of Q_{net}, $P - E$, and wind stress (Figs. 3.11–3.13) and the long-term perspective of the change of the forcing functions (Fig. 3.14) is made possible by integrating multi-group efforts. Ocean surface LH, SH, E and wind stress values are from the Objectively Analyzed air–sea Fluxes (OAFlux) project (Yu and Weller 2007). Surface SW and LW radiative fluxes are from the Clouds and the Earth's Radiant Energy Systems (CERES) Fast Longwave And Shortwave Radiative Fluxes (FLASHFlux) version 4A product (Stackhouse et al. 2006). Global P is derived from the Global Precipitation Climatology Project (GPCP) version 2.3 products (Adler et al. 2018). The CERES Energy Balanced and Filled (EBAF) surface SW and LW version 4.1 products (Loeb et al. 2018; Kato et al. 2018) are used in the time series analysis.

1) SURFACE HEAT FLUXES

The 2021 Q_{net} anomaly pattern (Fig. 3.11a) has predominant positive anomalies (anomalously downward heat input; a warming effect on the ocean) in the equatorial and South Pacific and Indian Oceans. In the North Pacific, positive anomalies occurred along the Kuroshio extension near 35°N, perhaps associated with a northward shift in that current (Fig. 3.18a), resulting in less heat flux out of the ocean (positive anomalous fluxes into the ocean) in the region where the current vacated. In the North Atlantic, positive anomalies occurred at two locations: the Gulf of Mexico and the Sargasso Sea (10°–30°N), and the subpolar gyre including the Labrador and the Irminger Seas (40°–65°N). Negative Q_{net} anomalies (anomalously upward heat release; a cooling

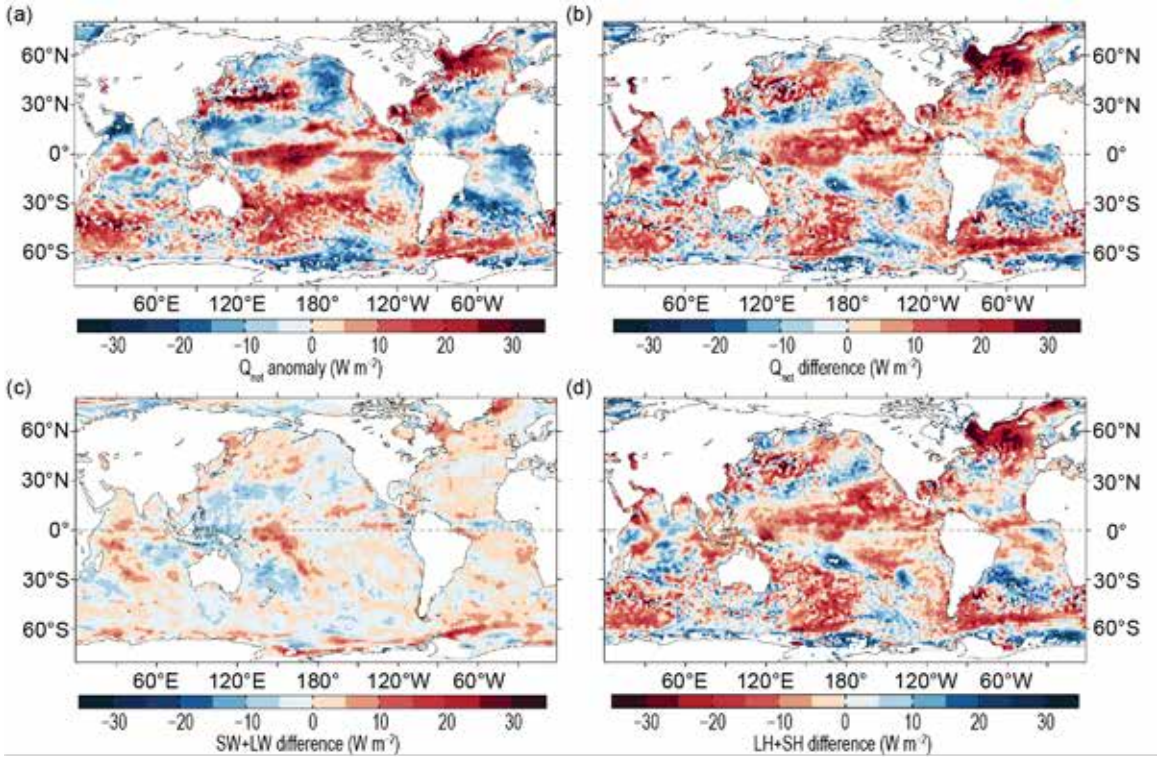

Fig. 3.11. (a) Surface heat flux (Q_{net}) anomalies (W m^{-2}) for 2021 relative to a 2001–15 climatology. Positive values denote ocean heat gain. 2021 minus 2020 difference for (b) Q_{net} and (c) surface radiation (SW+LW), and (d) turbulent heat fluxes (LH+SH), respectively. Positive differences denote more ocean heat gain in 2021 than in 2020, consistent with the reversal of the color scheme in (d). LH+SH are from OAFlux, and SW+LW is the NASA FLASHFlux version 4A.

effect on the ocean) dominated the tropical Atlantic from 30°S to 30°N, and also the subtropical (5°–20°N) and eastern (30°–60°N) North Pacific. The magnitude of maximum positive and negative anomalies exceeded 20 W m^{-2} in some localized bands.

The 2021 minus 2020 Q_{net} differences (Fig. 3.11b) have a spatial structure similar to the 2021 anomalies (Fig. 3.11a) in the extratropical region but different in the tropical ocean. There are more positive Q_{net} 2021 minus 2020 differences in the tropical basins, which are attributable to the reduced LH+SH differences (negative in reddish colors). Here, increased LH+SH (positive anomalies) have a cooling effect (blue colors) on the ocean and conversely, reduced LH+SH (negative anomalies) have a warming effect (red colors). In regions where winds are moderate and less variable, LH+SH heat release generally decreases with decreasing SST and increases with increasing SST. During this double-dip La Niña, LH+SH weakened accordingly associated with negative SSTA in the central and eastern tropical Pacific, resulting in an increase of Q_{net} input to the ocean. In general, SW+LW 2021 minus 2020 differences (Fig. 3.11c) are comparably weaker than LH+SH differences, with maximum magnitude around 10 W m^{-2}. However, SW+LW and LH+SH differences have similar spatial structures over most of the global ocean.

Outside of the tropical ocean, the LH+SH anomalies are most pronounced in the subpolar North Atlantic (40°–65°N), including the Labrador and Irminger Seas, with magnitude reduced by more than 25 W m^{-2}. The subdued turbulent heat release was associated with marked weakening of surface winds (Fig. 3.13b) and surface warming (see Fig. 3.1b) in the region.

2) SURFACE FRESHWATER FLUXES

The spatial structure of the 2021 $P - E$ anomaly field (Fig. 3.12a) has an interesting correlation with the 2021 SSTA pattern (Fig. 3.1a). In the Pacific, the SSTA horseshoe pattern is shaped by a strong negative Pacific decadal oscillation (PDO) phase and a double-dip La Niña, with positive SSTA in the western Pacific and negative SSTA in the central and eastern Pacific. $P - E$ had positive anomalies (green colors in Fig. 3.12; a freshening effect on the ocean surface) in regions

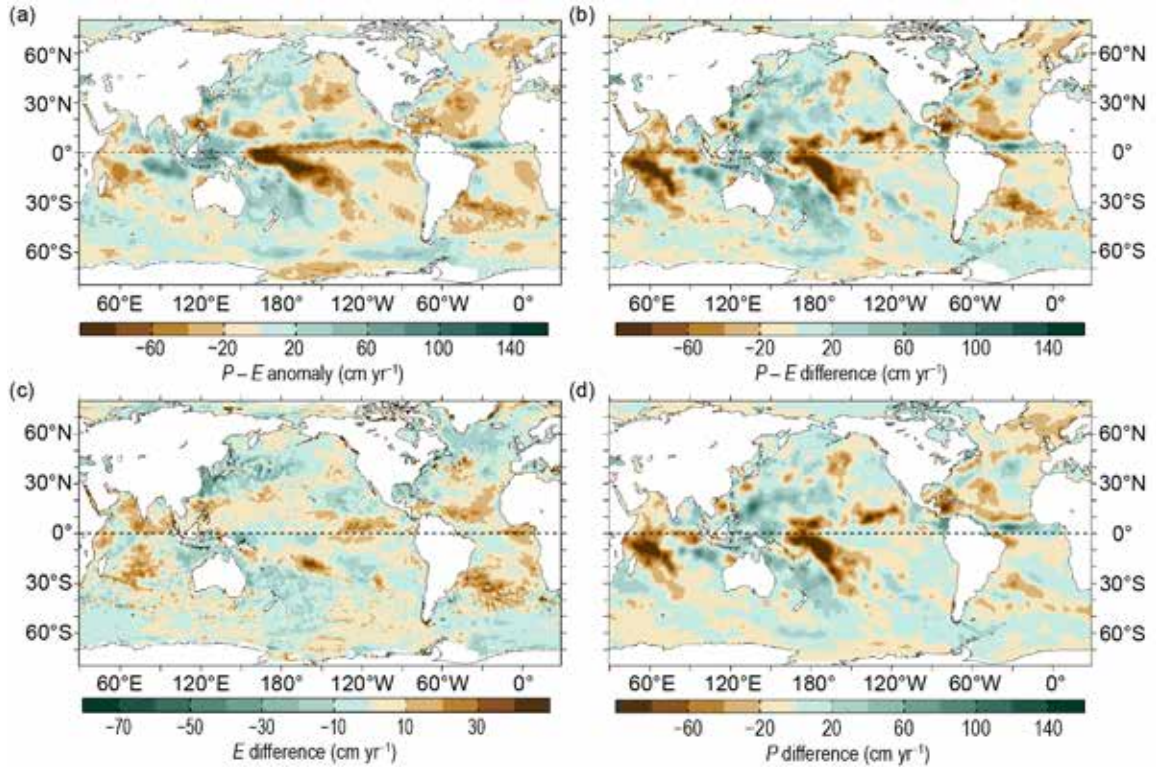

Fig. 3.12. (a) Surface freshwater (*P* – *E*) flux anomalies (cm yr^{-1}) for 2021 relative to a 1988–2015 climatology. 2021 minus 2020 differences for (b) *P* – *E*, (c) evaporation (*E*), and (d) precipitation (*P*). Green colors denote anomalous ocean moisture gain, and browns denote loss, consistent with the reversal of the color scheme in (c). *P* is the GPCP version 2.3rB1 product, and *E* is from OAFlux.

of positive SSTA and negative anomalies (brown colors in Fig. 3.12; a salinification effect on the ocean surface) in regions of negative SSTA. The reduced net freshwater input (> 60 cm yr^{-1}) in the central and eastern equatorial Pacific was caused by the westward retreat of tropical rainfall during La Niña.

The relationship between *P* – *E* and SSTA in the Atlantic Ocean, however, differs from that in the Pacific. The Atlantic Ocean was abnormally warm in 2021 across almost all latitudes except for a limited cool region in the Irminger Sea near 60°N. The positive SSTA pattern corresponds with negative (dry) *P* – *E* anomalies, excluding the equatorial band. The drying condition was caused primarily by the reduction in *P*, leading to a net freshwater deficit of about 20 cm yr^{-1}.

The 2021 minus 2020 *P* – *E* difference pattern (Fig. 3.12b) is similar to the 2021 *P* – *E* anomaly pattern (Fig. 3.12a), with the tropical Indian Ocean being the only region where the differences are substantially larger than anomalies. Bands of reduced *P* – *E* differences (negative anomalies with magnitude greater than 60 cm yr^{-1}) dominated the equatorial and western tropical Indian Ocean. These changes were induced primarily by *P* (Fig. 3.12d) and secondarily by *E* (Fig. 3.12c). These *P* – *E* differences coincided with the bands of increased SW+LW differences (Fig. 3.11c), indicating that SW+LW increased in areas of reduced rainfall when the region was subject to a negative Indian Ocean dipole (IOD) index with predominant negative SSTA.

3) WIND STRESS

The 2021 wind stress anomaly pattern (Fig. 3.13a) is dominated by wind changes at mid- to high latitudes. In the Southern Hemisphere, the westerlies strengthened substantially over the Antarctic Circumpolar Current (ACC) region between 50° and 60°S, featuring positive anomalies across the entire belt with varying magnitudes. The center of the maximum enhancement occurred in the Pacific sector (from the dateline to 80°E), with the anomalies reaching up to 0.05 N m^{-2}, whereas anomalies in the Atlantic and Indian Ocean sectors were 0.03 N m^{-2}. In the North Pacific and North Atlantic Oceans, the midlatitude westerlies became weaker, with negative wind

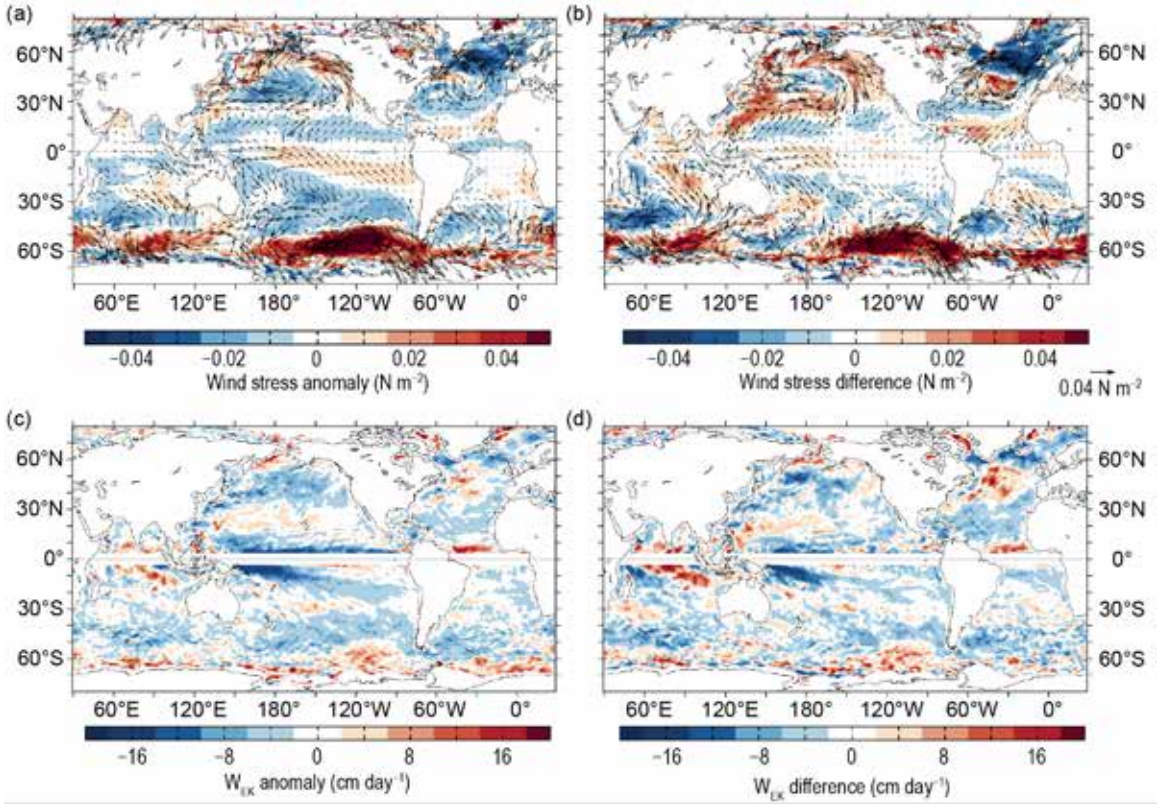

Fig. 3.13. (a) Wind stress magnitude (colors) and vector anomalies (N m^{-2}) for 2021 relative to a 1988–2015 climatology, (b) 2021 minus 2020 differences in wind stress, (c) Ekman vertical velocity (W_{EK}; cm day^{-1}) anomalies for 2021 relative to a 1988–2015 climatology, and (d) 2021 minus 2020 differences in W_{EK}. In (c) and (d), positive values denote upwelling tendency, and negative downwelling tendency. Winds are computed from the OAFlux.

anomalies predominating in the mid- to high latitudes (30°–70°N). The westerlies in the North Pacific weakened in the central basin and strengthened in the peripheral areas. By comparison, the westerlies in the North Atlantic weakened considerably around a slightly strengthened core near 50°N, and the reduction in wind magnitude was particularly pronounced in the northern North Atlantic between 50° and 65°N, with anomalies exceeding −0.05 N m^{-2}. Wind changes in the tropical oceans were small, where northeasterlies decreased slightly and southeasterlies increased slightly in the Pacific. The extratropical wind stress anomaly pattern in 2021 is further amplified in the 2021 minus 2020 wind stress difference map (Fig. 3.13b), most evidently in the North Atlantic and over the southern ACC. The westerlies in the North Pacific were mostly stronger than those in 2020, though weaker than those in 2020 in the center of the basin.

Spatial variations of winds cause divergence and convergence of the Ekman transport, leading to a vertical velocity, termed Ekman pumping (downwelling; directed downward) and suction (upwelling; directed upward) velocity, W_{EK}, at the base of the Ekman layer. $W_{EK} = 1/p\Delta\times(\tau/f)$, where p is the density and f the Coriolis force. The 2021 W_{EK} anomaly pattern (Fig. 3.13c) shows marked downwelling (negative) anomalies in the off-equatorial Pacific and marked upwelling (positive) anomalies in the off-equatorial Indian Ocean with magnitudes exceeding 16 cm yr^{-1} in both regions. These anomalies represent an enhancement of the regional mean conditions. On the other hand, the upwelling (positive) anomalies north of the equatorial Atlantic were a reduction of the typical downwelling condition. Outside of the equatorial zones, W_{EK} anomalies of substantial magnitude are observed at higher latitudes. The strengthened westerlies over the ACC induced larger upwelling (positive) anomalies, further amplifying the typical upper Ekman suction. The weakened westerlies in the North Atlantic produced downwelling anomalies to the north and upwelling anomalies to the south, which weakened the mean conditions. The 2021 W_{EK} 2021 minus 2020 difference pattern (Fig. 3.13d) suggests that there was an enhanced mean upwelling in the southeastern equatorial Indian Ocean during this weakly negative IOD index year,

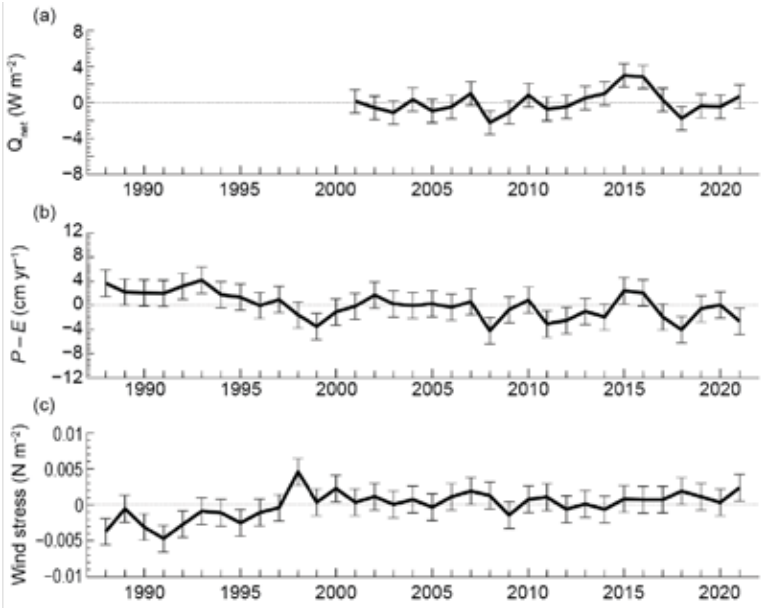

Fig. 3.14. Annual mean time series of global averages of (a) net surface heat flux (Q_{net}; W m^{-2}) from the combination of CERES EBAF4.1 SW+LW and OAFlux LH+SH. The 2021 Q_{net} estimate is based on FLASHFlux and OAFlux. Qnet anomalies are relative to the 2001–15 climatology, and positive anomalies denote increased net downward heat flux into the ocean that has a warming effect on the ocean surface. (b) Net freshwater flux ($P - E$; cm yr^{-1}) from the combination of GPCP P and OAFlux E. P $P - E$ and anomalies are relative to a 1988–2015 climatology, and positive anomalies denote increased freshwater flux into the ocean that causes sea surface freshening. (c) Wind stress magnitude (N m^{-2}) from OAFlux. Wind stress anomalies are relative to a 1988–2015 climatology, and positive anomalies denote increased wind stress magnitude over the ocean. Error bars denote one standard deviation of annual mean variability.

an enhanced mean downwelling in the western equatorial Pacific during the double-dip La Niña, and a weakened mean downwelling in the equatorial Atlantic when a strong Atlantic Niño prevailed.

4) LONG-TERM PERSPECTIVE

Multi-decade annual mean time series of Q_{net}, $P - E$, and wind stress averaged over the global ice-free oceans (Figs. 3.14a–c) provide a long-term perspective on the 2021 ocean surface forcing functions. The Q_{net} time series commenced in 2001, when CERES EBAF4.1 surface radiation products became available. The $P - E$ and wind stress time series both start in 1988 when modern flux data records can be assembled with the availability of Special Sensor Microwave/Imager (SSM/I) satellite retrievals.

Q_{net} was less variable between 2001 and 2007 but had large interannual fluctuations thereafter. The total downward heat flux into the global ocean increased by about 3 W m^{-2} during 2011–16, when the tropical Pacific underwent a strong La Niña event in 2011 and a strong El Niño event in 2016. This period of increased oceanic heat gain coincided with an increase of the global mean SST by about 0.35°C (see Fig. 3.3). Q_{net} went down during the 2017–18 La Niña and has slowly built up since then. The 2021 Q_{net} was up slightly from the 2020 Q_{net}. The $P - E$ time series shows similar interannual variability to that of the Q_{net} time series, and the 2021 level was down slightly from the 2020 level. The data record of wind stress is largely flat in the recent two decades after a regime shift around 1999. The 2021 winds were up slightly from the 2020 level. The error bars in the time series represent one standard deviation of year-to-year variability.

Sidebar 3.1: **Ocean, cryosphere, and sea level change in the IPCC AR6**—B. FOX-KEMPER, H. T. HEWITT, AND D. NOTZ

The Sixth Assessment Report (AR6) of the United Nations Intergovernmental Panel on Climate Change (IPCC) was approved and released in 2022. We were authors of the "Ocean, Cryosphere, and Sea Level Change" chapter (Fox-Kemper et al. 2021a). The AR6 differs from past reports in format: previous topics are recombined into global chapters, process chapters (including ours), regional chapters, and an interactive atlas. The AR6 cycle also includes two special reports with significant oceanic content (IPCC 2018, 2019).

The AR6 covers observations and projections of key climate metrics, including two new ones: upper ocean stratification and mixed layer depth (Figs. SB 3.1b,c). These metrics link climate change with ocean ecosystem impacts (IPCC 2019) and air–sea transfer biases. Rapid progress in analyzing these metrics is

reflected by the AR6 assessment of a 4.9 ± 1.5% increase in 0–200 m stratification from 1970 to 2018, roughly double the rate reported by IPCC (2019).

New and continuing monitoring—by tide gauges, Argo, satellites, moorings, and glacier and ice sheet inventories—lengthened and improved on observations in previous reports. Notably, loss of ice mass from the ice sheets in Greenland and the Antarctic over the period 1992–2020 accounts for more than 20 mm of global sea level rise. The combined ice mass loss during 2010–19 quadruples the loss over 1992–99, contributing alongside increased thermosteric expansion to a rate of sea level rise over 2006–18 more than double the 1901–2018 rate.

New model intercomparison projects (MIPs; Eyring et al. 2016), including the latest CMIP6 ensemble of traditional climate models, but also eddy-permitting ocean models, process MIPs, and emulators of these MIPs (e.g., Edwards et al. 2021) build upon past approaches but allow for more revealing projections in AR6, including anthropogenic attribution of regional and extreme events. High-resolution models often improve SST, ocean overturning circulation, ocean heat content change, and sea ice cover considerably over coarser resolution models.

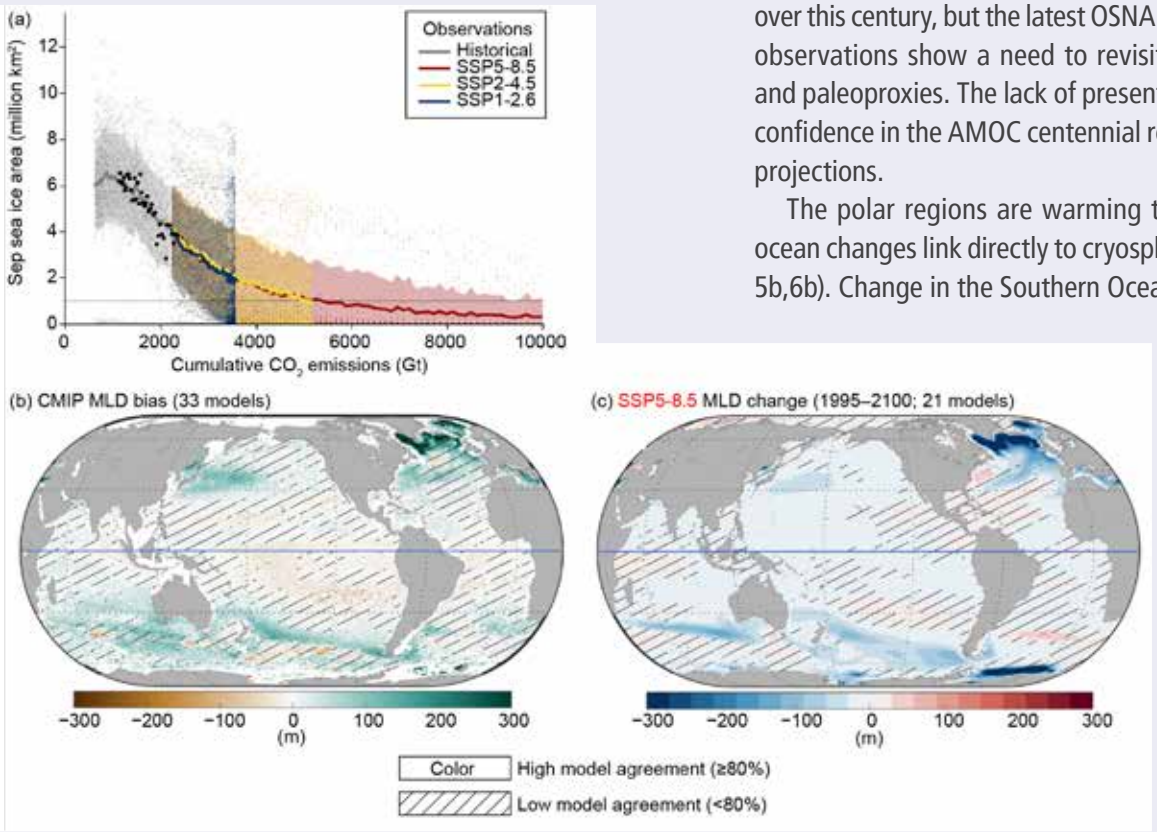

Fig. SB3.1. New scaling and metrics from the IPCC (Fox-Kemper et al. 2021). (a) Arctic September sea ice area (million km^2) as a function of cumulative CO_2 emissions from observations and projections (SSPs). (b) CMIP6 33-model winter (Dec–Feb) mixed layer depth ensemble mean bias vs. an Argo climatology (m; Holte et al. 2017). (c) CMIP6 22-model ensemble mean winter (Dec–Feb) mixed layer depth change (m) from 1995 to 2100 following the SSP5-8.5 scenario.

Over all assessed time windows, the oceans retain over 90% of the anthropogenic warming in Earth's energy budget, over 30% of the anthropogenic carbon in Earth's carbon budget, and over 40% of anthropogenic sea level rise can be attributed to thermosteric expansion (Canadell et al. 2021; Forster et al. 2021; Fox-Kemper et al. 2021a). CMIP6 models tended toward higher climate sensitivity than CMIP5 models, highlighting the need to use observations to constrain the assessment (Sherwood et al. 2020) and motivating a new AR6 method for assessing temperature, energy, and sea level budgets (Forster et al. 2021; Fox-Kemper et al. 2021a). Using consistent emulators in the energy and sea level assessments proved possible and transparent (Palmer et al. 2018; Smith et al. 2021; Fox-Kemper et al. 2021b). Measured changes in contributing processes in the observed sea level and energy budgets consistently sum to agree with observed total rise and warming. The oceanic carbon and energy uptake are understood through shared processes and circulations (Canadell et al. 2021, IPCC Cross-Chapter Box 5.3), such as the Atlantic meridional overturning circulation (AMOC, section 3h), Southern Ocean overturning, and water mass transformations. Both low-resolution and high-resolution models consistently project steady decline in AMOC strength over this century, but the latest OSNAP data and selected earlier observations show a need to revisit AMOC in these models and paleoproxies. The lack of present agreement lowered AR6 confidence in the AMOC centennial reconstructions and model projections.

The polar regions are warming the fastest and there the ocean changes link directly to cryospheric change (see sections 5b,6b). Change in the Southern Ocean and adjacent shelves is intimately linked to the future of the Antarctic ice sheet, oceanic and atmospheric drivers of ice melt, and thus sea level rise uncertainty. Even high-resolution models do not capture important coastal, submesoscale, and sub-ice shelf processes. Overall oceanic Antarctic change has not emerged as clearly as Arctic change, but regional Antarctic changes are increasingly apparent in observations

and high-resolution models. Arctic September sea ice loss is noted in AR6 to be a near-linear function of warming level rather than related to a possible tipping point (Fig. SB3.1a).

The observed rate of sea level rise (section 3f) continues to increase, assessed in the AR6 as 3.69 [3.21–4.17] mm yr^{-1} over 2006 to 2018, compared to 1.73 [1.28–2.17] mm yr^{-1} from 1901 to 2018. Overall, projected sea level rise ranges in AR6 are consistent with past reports (IPCC 2013, 2019), although emulators of ice sheet model comparisons (ISMIP6 and LARMIP-2) and ocean thermosteric expansion allow a greater and more transparent exploration of the impacts of ice sheet instabilities, and scenario and model uncertainties on the ranges. For example, considering only processes projectable with medium confidence, global mean sea level (GMSL) will likely rise by 2100 between 0.38 [0.28–0.55] m in the low-emission SSP1-1.9 scenario and 0.77 [0.63–1.02] m in the high-emission SSP5-8.5 from 1995–2014 levels. By contrast, an AR6 low-likelihood, high-impact storyline building upon emulators of models including ice sheet instabilities and structured expert judgment has roughly double the upper limit of the likely range of sea level increase. The potential contribution of processes that cannot be ruled out are quantified in AR6 even while still clouded by deep uncertainty.

Building on the IPCC (2018) warming level approach, we also sketched outcomes as a function of future potential warming. Under 1.5–2°C global warming, a practically sea ice-free Arctic Ocean is expected in September at least in some years as is the loss of up to half of today's glacier mass and top 3 m of permafrost volume. In the long term, committed GMSL rise over 2000 years is projected to be 2–6 m with 2°C of peak warming. By contrast, warming between 3° and 5°C causes the Arctic Ocean to be sea ice-free for several months in most years, irreversible loss of the West Antarctic Ice Sheet and most of the Greenland Ice Sheet, complete loss of nearly all alpine glaciers, and committed GMSL rise over 2000 years of 4–22 m will likely occur after this level of peak warming.

In summary, the most recent IPCC report (IPCC 2021) highlights yet again the vulnerability and fragility of the world's ocean and cryosphere. Our increasing skill in projecting oceanic and cryospheric changes and attributing them to anthropogenic climate change foretells millennia of consequences for the oceans and cryosphere.

f. Sea level variability and change—P. R. Thompson, M. J. Widlansky, E. Leuliette, D. P. Chambers, W. Sweet, B. D. Hamlington, S. Jevrejeva, M. A. Merrifield, G. T. Mitchum, and R. S. Nerem

Annual average global mean sea level (GMSL) from satellite altimetry (1993–present) reached a new high during 2021, rising to 97.0 mm above 1993 (Fig. 3.15a). This marks the 10th consecutive year (and 26th out of the last 28) that GMSL increased relative to the previous year, reflecting an ongoing multi-decadal trend of 3.4 ± 0.4 mm yr^{-1} in GMSL during the satellite altimetry era (Fig. 3.15a). A quadratic fit with corrections for the eruption of Mount Pinatubo (Fasullo et al. 2016) and ENSO effects (Hamlington et al. 2020) yields a climate-driven trend of 3.0 ± 0.4 mm yr^{-1} and acceleration of 0.081 ± 0.025 mm yr^{-2} (updated from Nerem et al. 2018).

Independent observing systems measure the contributions to GMSL rise from increasing ocean mass, primarily due to melting of glaciers and ice sheets (see sections 5e, 6d, 6e), and decreasing ocean density, primarily due to ocean warming (section 3c). Data from Argo profiling floats analyzed by Scripps Institution of Oceanography (SIO; Roemmich and Gilson 2009) show a global mean steric (i.e., density-related) sea level trend of 1.4 ± 0.2 mm yr^{-1} during 2005–21 (Fig. 3.15a). Global ocean mass (excluding regions within 300 km of land), produced by the NASA Jet Propulsion Laboratory (JPL) using mass concentration anomalies from the Gravity Recovery and Climate Experiment (GRACE) and GRACE Follow-On (GRACE-FO) missions, show a global mean ocean mass trend of 2.2 ± 0.4 mm yr^{-1} during 2005–21 (Fig. 3.15a). The sum of these trend contributions agrees within uncertainties with the GMSL trend of 3.9 ± 0.4 mm yr^{-1} measured by satellite altimetry since 2005 (Leuliette and Willis 2011; Chambers et al. 2017). Consistency among trends from these independent observing systems is a significant achievement and increases confidence in estimates of Earth's energy imbalance (e.g., Hakuba et al. 2021; Marti et al. 2022).

Annually averaged GMSL from satellite altimetry increased 4.9 mm from 2020 to 2021, exceeding the sum of year-over-year increases in global mean steric sea level from Argo, 1.0 mm,

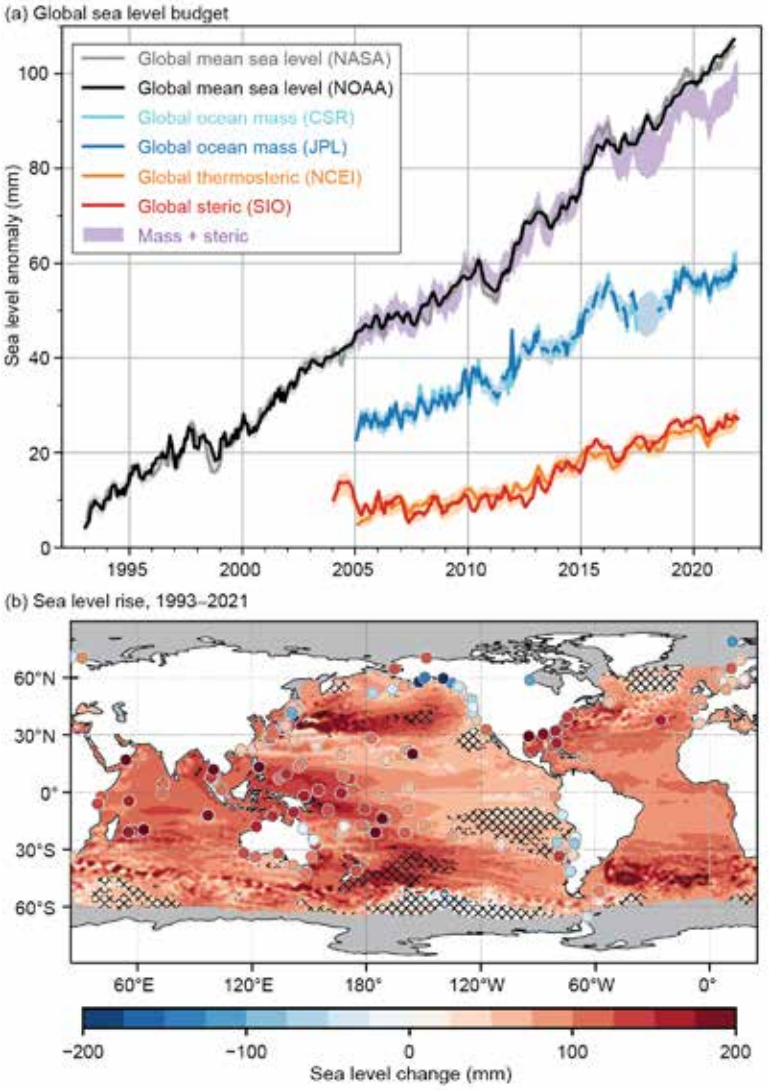

Fig. 3.15. (a) Monthly averaged GMSL (mm) observed by satellite altimeters (1993–2021) from the NOAA Laboratory for Satellite Altimetry (black) and NASA Sea Level Change Program (gray). Monthly global ocean mass (2005–21) from GRACE and GRACE-FO calculated from mascons produced by NASA JPL (blue) and University of Texas Center for Space Research (CSR, cyan). Mascons fewer than 300 km from land were excluded in both ocean mass time series. Monthly global mean steric sea level (2004–21) from SIO Argo data (red). Monthly global mean thermosteric sea level from NCEI Argo and hydrographic data (orange). Monthly global ocean mass plus steric (purple). Shading around all data sources represents a 95% confidence range based on Gaussian process regressions onto each pair of time series. (b) Total local sea level change during 1993–2021 as measured by satellite altimetry (contours) and tide gauges (circles). Hatching indicates local changes that differ from the change in GMSL by more than one standard deviation.

and global mean ocean mass from GRACE-FO, 1.2 mm. The discrepancy is a continuation of misclosure in the sea level budget since 2016 (Fig. 3.15a; Chen et al. 2020), and its cause is an area of active research. Misclosure in the sea level budget is unlikely to be predominantly due to errors in estimating the global mass component of the budget (Hakuba et al. 2021). However, uncertainties in estimating changes in global ocean mass (e.g., leakage near land, geocenter, and glacial isostatic adjustment) warrant investigation (Chen et al. 2020). Likewise, error sources in the altimeter measurements, such as the wet tropospheric correction, may contribute but are unlikely to completely account for the discrepancy (Barnoud et al. 2021). Drift in Argo salinity measurements, the cause of which is still being investigated (Roemmich et al. 2019) can artificially suppress increasing global mean steric sea level, but quality control procedures applied in the SIO data product used here mitigate the impact of salinity drift (Barnoud et al. 2021). The SIO time series of steric sea level also compares favorably with a time series of global mean thermosteric sea level from the NOAA National Centers for Environmental Information (NCEI; Fig. 3.15a). Undersampling of the ocean by Argo, especially around the Malay Archipelago between Asia and Australia (von Schuckmann et al. 2014), could also lead to underestimates of global mean steric rise.

Spatial structure in sea level changes over the 29-year altimeter record (Fig. 3.15b) is due to a combination of natural fluctuations in coupled modes of atmosphere–ocean variability (Han et al. 2017) and the oceanic response to anthropogenic radiative forcing (Fasullo and Nerem 2018). It is difficult to disentangle these contributions to regional differences in long-term sea level change (Hamlington et al. 2019), but as the altimetry record grows in length, the impact of natural fluctuations on regional sea level trends decreases. At present, only a small fraction of the global ocean has experienced sea level trends that differ from the global mean trend by more than one standard deviation (hatched areas, Fig. 3.15b). Reduced sea level trends in the tropical eastern Pacific reflect the impact of multidecadal variability in the strength of Pacific trade winds (e.g.,

Merrifield 2011), while enhanced sea level change in the high latitude South Pacific can be attributed to regional warming (Llovel and Terray 2016; Volkov et al. 2017). Sea level change relative to land (i.e., the quantity measured by tide gauges; circles, Fig. 3.15b) is most relevant for societal impacts and can differ substantially from satellite-derived changes in tectonically active regions (e.g., Japan) and areas strongly affected by glacial isostatic adjustment (e.g., Alaska; Fig. 3.15b).

Due to long-term trends in GMSL (Fig. 3.15), annual sea level anomalies during 2021 were positive nearly everywhere (Fig. 3.16a). In the global tropics, the highest sea level anomalies were in the western Pacific and the eastern Indian Ocean (10–15 cm above the climatological average), whereas the lowest anomalies were in the northeastern Pacific and parts of the south-central Indian Ocean (0–5 cm below average). Sea level anomalies were positive across most of the subtropics, although the amounts varied regionally. The 2021 annual mean anomalies exceeded 15 cm in parts of the midlatitudes, such as in the extension regions of the Kuroshio and Gulf Stream Currents.

The double-dip La Niña events that developed during summer 2020 and again in August 2021 (see section 4b) explain the mostly consistent sea level pattern during both years, at least in the equatorial central Pacific (Fig. 3.16b). Year-to-year sea level increases exceeding 10 cm occurred in the tropical western Pacific, as well as in the eastern Indian Ocean, which were mostly continuing positive changes from the prior two years. In the South Pacific Convergence Zone (SPCZ) region (Brown et al. 2020), the 2021 sea levels were also 10–15 cm higher compared to 2020. The largest regions of decreasing sea levels during 2021 compared to 2020 were in the tropical western Indian Ocean as well as in the western, central, and eastern tropical North Pacific basin. Around Hawaii, the 10 cm decrease in sea level (2021 minus 2020) nearly cancelled the prior year-over-year increase. In the Atlantic Ocean, the 2021 minus 2020 sea level difference was mostly positive, although typically less than 5 cm in magnitude. Larger changes during 2021 occurred in the Gulf of Mexico (associated with the Loop Current) and in the regions most affected by mesoscale oceanic eddies (generally poleward of ±30° latitude). Overall, these sea level changes from 2020 to 2021 (Fig. 3.16b) are representative of the underlying OHCA changes in these locations (Fig. 3.4b).

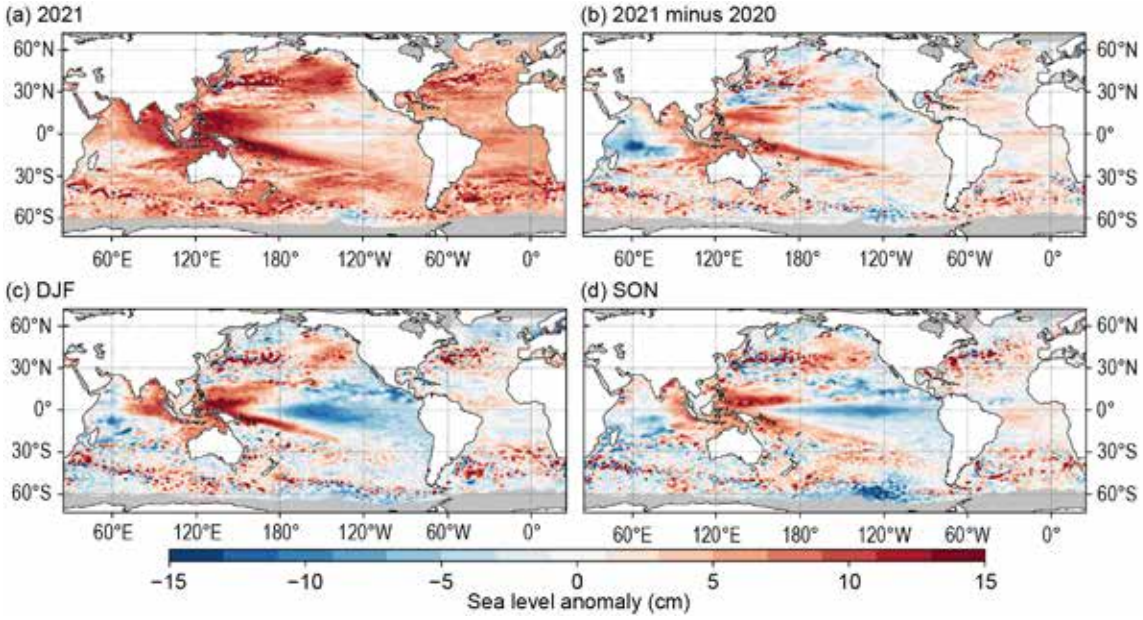

Fig. 3.16. (a) Annual average sea level anomaly during 2021 relative to average sea level at each location during 1993–2021. (b) Average 2021 minus 2020 sea level anomaly. (c) Average sea level anomaly during DJF 2021 relative to the 1993–2020 average. (d) Same as (c), but for SON. Units are given in cm. GMSL was subtracted from panels (c),(d) to emphasize regional, non-secular change. Altimetry data were obtained from the gridded, multi-mission product maintained by the Copernicus Marine and Environment Monitoring Service (CMEMS).

The double-dip La Niña (see section 4b) during 2021, and the respective continuation of below-average sea levels in the eastern half and above-normal value in the western half of the equatorial Pacific, limited the amount of intra-seasonal changes evident in the comparison of December–February (DJF) and September–November (SON) anomalies (Figs. 3.16c,d). In the Indian Ocean, the sea level pattern was also mostly similar at the beginning and end of 2021 (i.e., sea level anomalies increasing from west to east). Some of the highest regional sea level anomalies during 2021 occurred in Bay of Bengal, where satellite-observed seasonal anomalies were more than 15 cm above average during both DJF and SON. In the northwestern Atlantic Ocean, seasonal sea level anomalies were overall higher during SON compared to the beginning of the year, especially near the U.S. mid-Atlantic coast.

Ongoing trends, year-to-year variability, and seasonal changes in sea level impact coastal communities by increasing the magnitude and frequency of positive sea level extremes that contribute to flooding and erosion. Minor impacts tend to emerge when local water levels exceed the 99th percentile of daily sea level maxima (Sweet et al. 2014). Using 1993–2021 as the analysis epoch (consistent with the altimetry baseline), daily sea level maxima that exceed the 99th percentile—hereafter extreme sea level events—occurred more frequently in recent years compared to previous decades. Across 114 tide-gauge locations with sufficient data volume and quality for analysis, the median number of extreme sea level events per year and location increased from one during 1993–97 to four during 2017–21 (not shown). The 90th percentile of events per year and location increased from six during 1993–97 to 15 during 2017–21 (not shown).

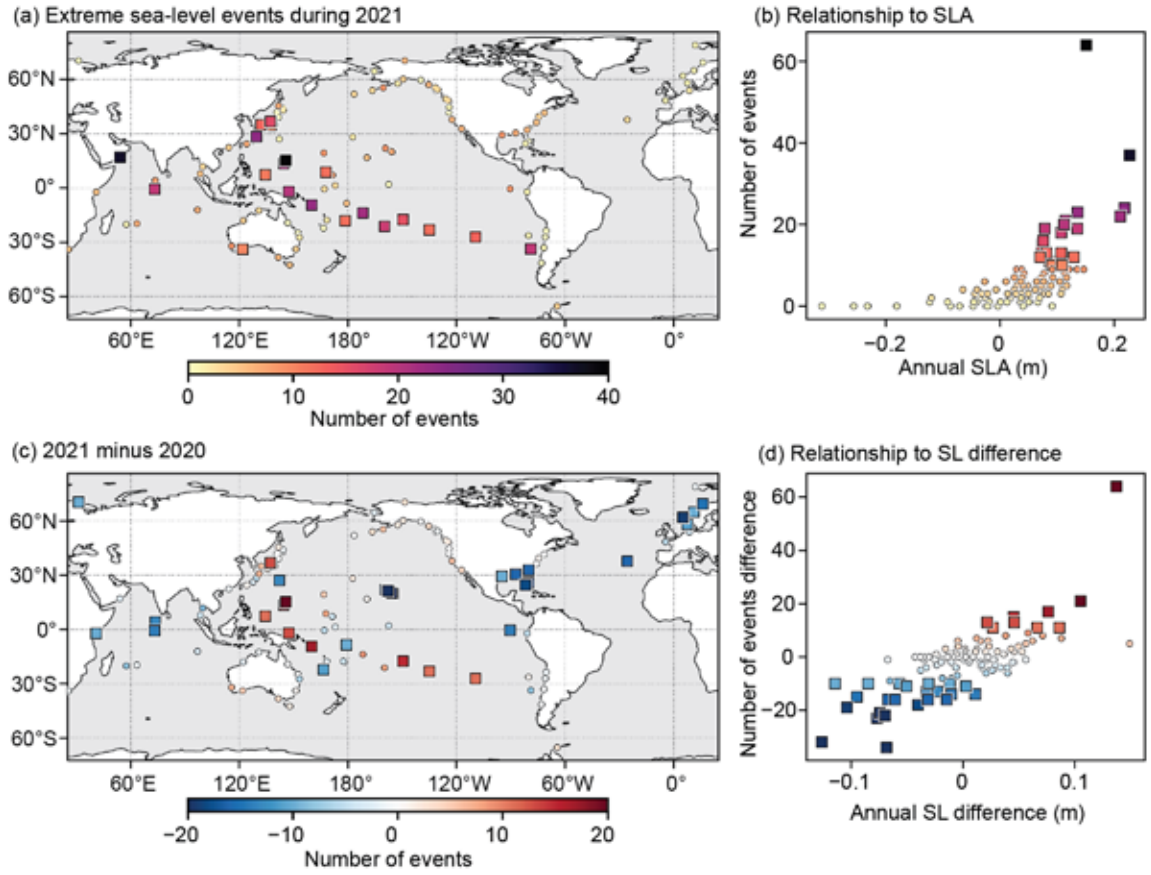

Fig. 3.17. (a) Number of extreme sea level events from tide gauges during 2021. (b) Counts in (a) as a function of annual sea level anomaly during 2021. Square markers in (a) and (b) highlight locations with more than 10 extreme events. (c) Change in number of extreme sea level events from 2020 to 2021. (d) Counts in (c) as a function of the change in annual sea level from 2020 to 2021. Square markers in (c) and (d) highlight locations where the magnitudes of changes in counts of extreme events were greater than 10. Counts of extreme sea level events were calculated from hourly tide gauge observations obtained from the University of Hawaii Sea Level Center Fast Delivery database. Only records with at least 80% completeness during 1993–2021 and 80% completeness during both 2020 and 2021, individually, were analyzed.

Twenty of the 114 locations experienced more than 10 extreme sea level events during 2021, which were especially concentrated in the tropical western Pacific and in a diagonal region of the South Pacific near the SPCZ (Fig. 3.17a) where annual sea level anomalies were largest (Figs. 3.16a, 3.17b). Many of these locations experienced increases of more than 10 extreme events per year from 2020 to 2021 (Fig. 3.17c), reflecting year-over-year increases in annual mean sea level (Figs. 3.16b, 3.17d). Twenty-four locations experienced at least 10 fewer extreme events per year in 2021 compared to 2020, which were concentrated in the western Indian Ocean, Hawaiian Islands, U.S. Gulf of Mexico and southeast Atlantic coasts, and northern Europe (Fig. 3.17c). In each of these regions, the annual mean sea level during 2021 was either mostly unchanged or lower compared to the prior year (Figs. 3.16b, 3.17d). Along the U.S. mid-Atlantic and New England coasts, the annual numbers of extreme events were similar during 2020 and 2021 (Fig. 3.17c), although most of the 2021 extremes occurred during SON when the regional sea level anomaly was 5–15 cm higher than earlier in the year (Figs. 3.16c,d). Of the 114 locations analyzed, Saipan experienced the greatest number (64) of extreme events during 2021 due—at least in part—to an annual mean sea level anomaly greater than 15 cm. Other locations experienced larger sea level anomalies but far fewer events, because it is the magnitude of the annual sea level anomaly relative to the typical range of hourly variability (including tides, synoptic variations, etc.) that most closely relates to the frequency of extreme events. In Saipan, 15 cm is more than 65% of the local standard deviation in hourly water levels—the highest percentage of locations analyzed.

g. Surface currents—R. Lumpkin, F. Bringas, and G. Goni

This section describes variations of ocean surface currents, transports, and associated features, such as rings, inferred from surface currents. Surface currents are obtained from in situ (a global array of drogued drifters and regional mooring arrays) and satellite (altimetry and wind stress) observations. Transports are derived from a combination of sea surface height anomaly (from altimetry) and climatological hydrography. See Lumpkin et al. (2011) for details of these calculations. Zonal surface current anomalies are calculated with respect to a 1993–2020 climatology and are discussed below for individual ocean basins.

1) PACIFIC OCEAN

In 2021, zonal geostrophic currents in the equatorial Pacific exhibited annual mean westward current anomalies of 6–8 cm s^{-1} from 150°E–100°W (Fig. 3.18a), 1°S–3.5°N, associated with the 2021 double-dip La Niña (see section 4b). In the same longitude range, westward

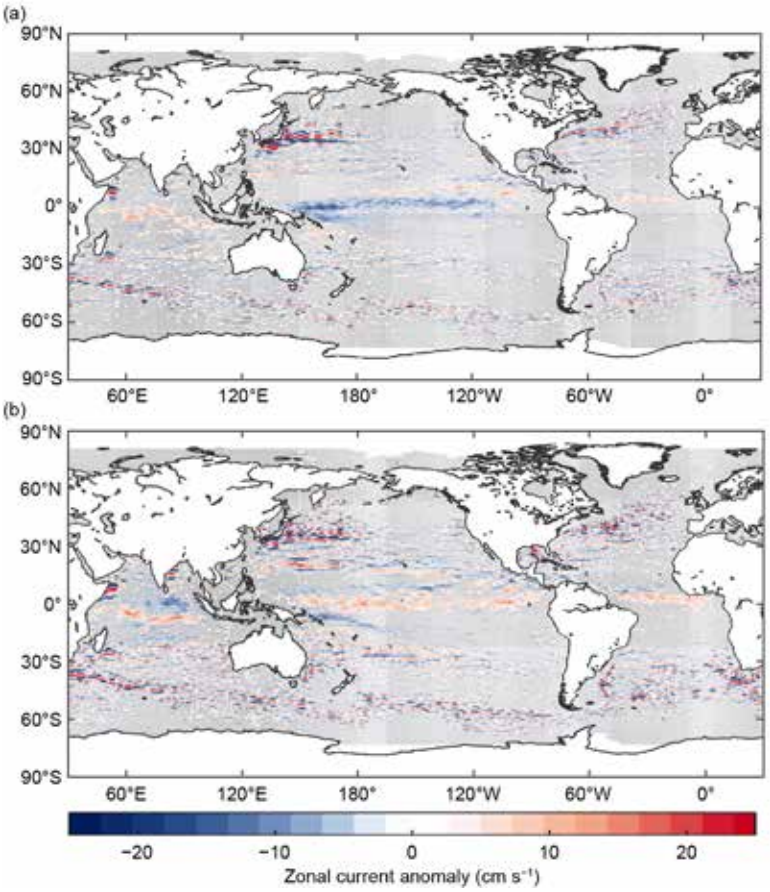

Fig. 3.18. Annually-averaged geostrophic zonal current anomalies (cm s^{-1}; positive is eastward, negative is westward) for (a) 2021 and (b) 2021 minus 2020 derived from a synthesis of drifters, altimetry, and winds. Gray stippling indicates where values are not significantly different from zero.

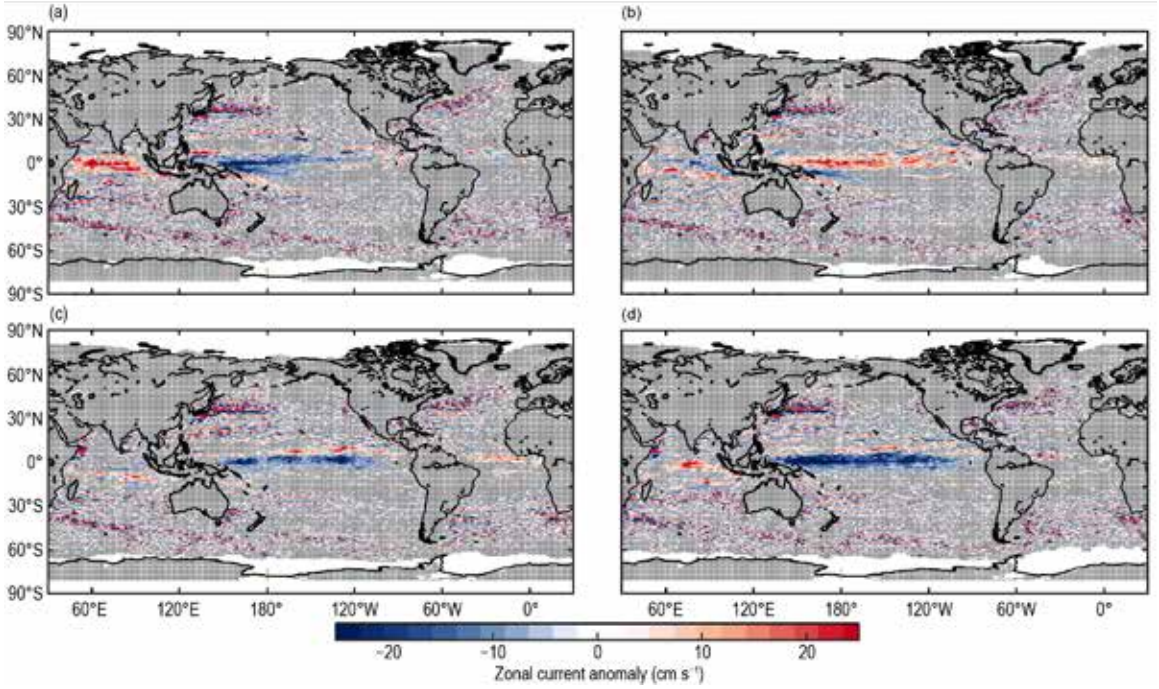

Fig. 3.19. Seasonally-averaged zonal geostrophic current anomalies with respect to seasonal climatology, for (a) Dec 2020–Feb 2021, (b) Mar–May 2021, (c) Jun–Aug 2021, and (d) Sep–Nov 2021. Gray stippling indicates where values are not significantly different from zero.

anomalies of 4–5 cm s^{-1} at 4°–6°S indicated a strengthened South Equatorial Current (SEC). The 2018–20 northward shift of the North Equatorial Countercurrent (NECC) was not observed in 2021. Because westward anomalies were larger through most of 2020, 2021 minus 2020 differences (Fig. 3.18b) show weak eastward equatorial anomalies.

Westward anomalies exceeding 20 cm s^{-1} were present in the western equatorial (1°S–1°N, 150°E–170°W) Pacific in December–February (Fig. 3.19a); in this longitude band, westward currents were anomalously strong from 7°S to 3°N. In March–May, eastward anomalies of 10–20 cm s^{-1} developed across the basin at 3°S to 2°N, leading the transition from La Niña to ENSO-neutral SST anomalies the following season (see section 4b). The equatorial anomalies reversed again in June–August, exceeding 10 cm s^{-1} westward from 1°S to 3°N across the basin with zonally-averaged maxima of 14 cm s^{-1} on the equator and at 2°N, again leading the development of La Niña SST anomalies the following season. North of this pattern, eastward anomalies of 5–8 cm s^{-1} were associated with an accelerated NECC during June–August. Both anomaly patterns persisted in September–November, with the westward equatorial anomalies strengthening to 20–25 cm s^{-1} at 0.5°S–1.5°N.

In the northwest Pacific, zonal current anomalies of ±20 cm s^{-1} bracketing 35.5°N (Fig. 3.18a) indicated a 2021 northward shift of up to 2° latitude of the Kuroshio extension, consistent with anomalously warm ocean heat content anomalies north of the climatological path of the Kuroshio (Fig. 3.4a) and perhaps associated with heat flux anomalies in the region (Fig. 3.11a).

2) INDIAN OCEAN

Annually averaged zonal currents in the Indian Ocean were close to their 1993–2020 climatological averages, with weak (2–4 cm s^{-1}) eastward anomalies from 8°S to the equator across most of the basin (Fig. 3.18a). Because eastward anomalies in this latitude range were significantly stronger (10–20 cm s^{-1}) in 2020, 2021 minus 2020 differences (Fig. 3.18b) exhibit negative anomalies of ~15 cm s^{-1} across the basin. During December–February (Fig. 3.19a), eastward anomalies of 10–20 cm s^{-1} were present across the basin from 2° to 6°S; these were replaced by westward

anomalies of 3–7 cm s^{-1} in March–May (Fig. 3.19b) that disappeared by June–August (Fig. 3.19c). Eastward anomalies of 10–20 cm s^{-1} developed in the central basin at 70°–85°E, 4.5°S–0.5°N in September–November (Fig. 3.19d), with peak values of 20 cm s^{-1} at 1°S reflecting an acceleration of the seasonal eastward Southwest Monsoon Current.

3) ATLANTIC OCEAN

Annual mean zonal currents in the tropical Atlantic Ocean in 2021 exhibited weak (4–5 cm s^{-1}) eastward anomalies from 3° to 4.5°N, indicating a southward shift of the NECC and the interface between it and the northern core of the South Equatorial Current (nSEC; see Lumpkin and Garzoli 2005) to its south. The core strength of the westward nSEC and other branches of the SEC were close to their climatological averages. Weak eastward anomalies were present in December–February and March–May, strengthened in June–August to a maximum of 10 cm s^{-1} at 3°N with anomalies > 5 cm s^{-1} at 1°–4.5°N, and weakened to near-zero values in September–November (Fig. 3.19).

Variability of key Atlantic Ocean currents is continuously monitored in near-real-time by leveraging relationships between in situ and satellite altimetry observations (https://www.aoml.noaa.gov/phod/indexes/index.php). In the South Atlantic, the number of rings shed by the Agulhas Current remained similar to the average number of shedding events in a given year during the 1993–2021 record. The annual transport of the Agulhas Current, an indicator of Indian-Atlantic Ocean interbasin water exchange, was slightly below the average by –1.5 Sv in a cross section at ~28°E and between 34° and 40°S and has remained within 1 std. dev. of the long-term average of 50.9 ± 3.2 Sv. In the southwestern Atlantic, the location of the Brazil-Malvinas Confluence has demonstrated a southward trend since 1993 at decadal time scales (cf. Lumpkin and Garzoli 2011; Goni et al. 2011), and was displaced to the south with respect to its 1993–2021 mean location for the fifth consecutive year. This southward trend is important since the location of the confluence indicates where waters of subtropical origin are entrained into a subpolar region. A northward shift of the confluence observed in 2016 (Fig. 3.20) appears to have been transient. During 2021, the confluence was on average 0.9 degrees of latitude south of its 1993–2020 mean location (37.8 ± 1.1)°S, a –0.5° shift compared to the previous year, and over 2 degrees of latitude south of its average location in the early 1990s (Fig. 3.20). This shift may be related to anomalously warm upper ocean heat content at this location driving a southward migration of the westerlies (see Figs. 3.4a, 3.13a). In the North Atlantic, the North Brazil Current (NBC) and associated rings serve as interhemispheric conduits for water masses and heat from the South Atlantic into the North Atlantic (Goni and Johns 2003). Some of their waters enter the Caribbean Sea while carrying low salinity Amazon River waters (Ffield 2007), which are known for creating barrier layers that can magnify hurricane intensification (e.g., Balaguru et al. 2012; Domingues et al. 2015). As in previous years, this current transport continues to show negative anomalies, possibly associated with fresh surface salinity anomalies in the NBC retroflection region (Fig. 3.7), while the number of rings do not show a departure from their mean values. Farther to the north, the Yucatan Current and Florida Current exhibited negative anomalies of –0.3 Sv and –0.5 Sv, respectively, with the transport in the Yucatan Current approximately 1 Sv below its long-term average during 2021 and relative low variability

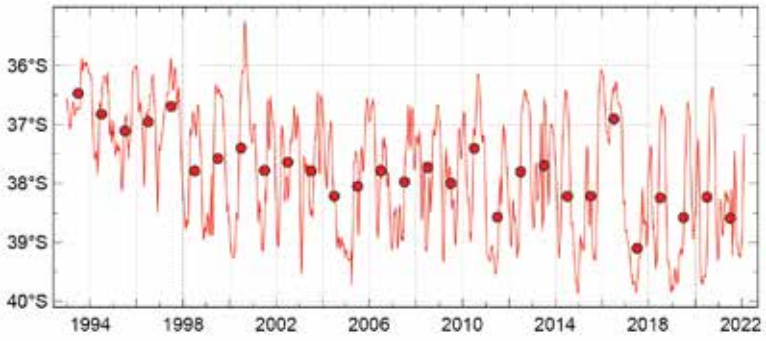

Fig. 3.20. Time series of the latitude of separation of the Brazil Current (BC) front from the continental shelf, defined as the intersection between the 1000 m bathymetry contour and the contour where the 10°C isotherm is 200 m deep. The red line is a 28-day running mean, red circles are annual mean values. The mean latitude of separation between 1993 and 2022 is (37.8 ± 1.1)°S. (Source: www.aoml.noaa.gov/phod/altimetry/cvar/mal/BM_ts.php)

during the last three years, with values within 1 std. dev. of its 27.5 ± 1.0 Sv average since 1993. This slight reduction in the 2021 Florida Current transport with respect to the period 1993–2020 is not significantly different from transport changes derived from cable measurements reported in the next section, for the period 1982–2021. The continuous lower-than-usual Florida Current transport is closely tied to higher coastal sea level and "sunny day" flooding events along the U.S. southeast coast (Ezer and Atkinson 2014; Domingues et al. 2016; Volkov et al. 2020). Further studies addressing the North Brazil Current to Florida Current connection may help develop early warnings for such flooding events.

h. Meridional overturning circulation and heat transport in the Atlantic Ocean—D. L. Volkov, S. Dong, J. Willis, W. Hobbs, W. Johns, D. A. Smeed, B. I. Moat, Y. Fu, S. Lozier, M. Kersalé, R. C. Perez, D. Rayner, E. Frajka-Williams, and G. Goni

The meridional overturning circulation (MOC) affects meridional large-scale transports of heat and freshwater that impact global and regional climate and weather patterns, sea level, and ecosystems. Several observational arrays exist across the Atlantic Ocean to monitor changes in the Atlantic MOC (AMOC) and meridional heat transport (AMHT; Frajka-Williams et al. 2019). Since the previous *State of the Climate in 2020* report (Volkov et al. 2021), the AMOC and AMHT estimates based on moored arrays (Fig. 3.21a) have been extended to March 2020 for the RAPID-MOCHA-WBTS array at 26.5°N and to May 2018 for the OSNAP array between 53° and 60°N (Frajka-Williams et al. 2021; Li et al. 2021a,b). No updates are presently available for the AMOC at 34.5°S, but the AMHT estimates at the SAMBA array based on direct observations have been published for the first time (Kersalé et al. 2021). In this report, we review updated AMOC/AMHT estimates from the moored arrays and present blended estimates based on combinations of satellite altimetry and in situ hydrographic data.

The subpolar North Atlantic is a key region for deep water formation, hence it plays an important role in the AMOC. A collaborative international effort to measure the AMOC here led to the establishment of the OSNAP array in 2014 (Lozier et al. 2017), which consists of two segments: OSNAP-West between Labrador and Greenland and OSNAP-East between Greenland and Scotland (Fig. 3.21a). The latest published AMOC/AMHT estimates span the first four years of observations (Li et al. 2021a,b; Fig. 3.21b), which will soon be extended to a nearly six-year record using the recently recovered data. Over the period from August 2014 to May 2018, the AMOC across the OSNAP array had a time-mean of 16.6 ± 0.7 Sv (1 Sv = 10^6 m^3 s^{-1}; the uncertainty is the standard error of the mean; Li et al. 2021a). The 30-day averages of the AMOC at the OSNAP array exhibit variability ranging from 8.2 to 24.5 Sv, with a standard deviation of 3.5 Sv. The OSNAP observations have revealed that the eastern subpolar basin (OSNAP-East) dominates the mean and variability of the AMOC across the entire subpolar North Atlantic. The OSNAP-East mean (16.8 ± 0.6 Sv) is more than six times greater than the OSNAP-West mean (2.6 ± 0.3 Sv). The AMOC across the entire OSNAP array is less than the sum across OSNAP-West and OSNAP-East because of cancellations between northward and southward transports (Lozier et al. 2019). The AMHT in 2014–18 had a time-mean of 0.50 ± 0.05 PW (1 PW = 10^{15} W), and was correlated at 0.8 with the AMOC (Fig. 3.21b). The remaining variance is attributed to the subpolar gyre circulation. Winter convection during 2014–18 in the interior subpolar basins had minimal impact on density changes in the deep western boundary currents (Li et al. 2021a). Contrary to previous modeling studies, no discernible relationship between western boundary changes and subpolar overturning variability has been found.

The longest-maintained trans-basin AMOC/AMHT observing array along approximately 26.5°N (RAPID-MOCHA-WBTS; Fig. 3.21a) has been updated through the spring of 2020 (Frajka-Williams et al. 2021; Fig. 3.21c). The mean AMOC and AMHT at 26.5°N for 2004–20 were 16.9 ± 0.7 Sv and 1.19 ± 0.06 PW, respectively. The mean AMOC and AMHT in 2019–20 were 15.4 ± 0.5 Sv and

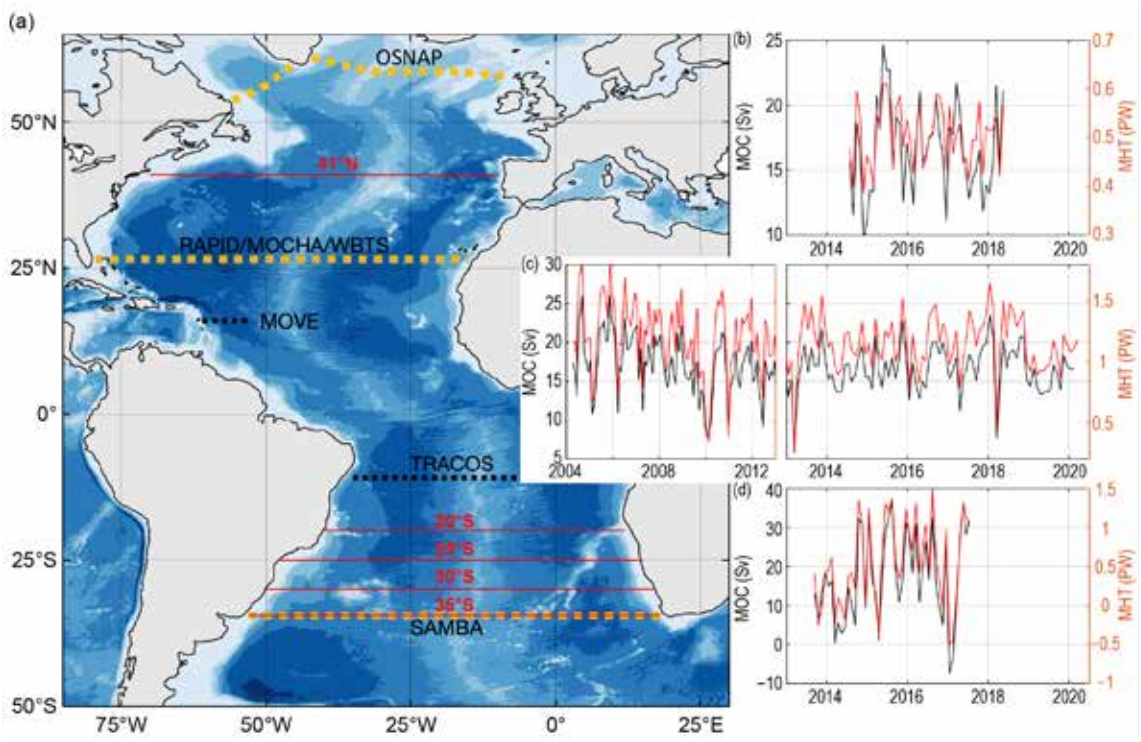

Fig. 3.21. (a) The Atlantic meridional overturning circulation (AMOC) observing system: moored arrays (dashed black and orange lines) and sections across which the AMOC is estimated by combining in situ measurements (Argo, XBT, bottom pressure) with satellite altimetry data (red lines). The moored arrays that have been updated since the *State of the Climate in 2020* report (orange dashed lines) include: OSNAP (Overturning in the Subpolar North Atlantic Program) in the subpolar North Atlantic, RAPID-MOCHA-WBTS (Rapid Climate Change/MOC and Heatflux Array/Western Boundary Time Series) at 26.5°N, and SAMBA (South Atlantic MOC Basin-wide Array) at 34.5°S. The arrays that have not yet been updated (black dashed lines) include: MOVE (Meridional Overturning Variability Experiment) at 16°N and TRACOS (Tropical Atlantic Circulation Overturning) at 11°S. (b) Monthly time series of the AMOC northward volume transport (black) and AMHT (red) across the OSNAP array. (c) Monthly time series of the AMOC northward volume transport (black) and AMHT (red) across the RAPID/MOCHA/WBTS array (the plot is split in two panels to zoom in on the time interval common for all arrays). (d) Monthly time series of the AMOC northward volume transport (black) and AMHT (red) across the SAMBA. Units for the AMOC/AMHT are Sv/PW.

1.03 ± 0.04 PW, lower than the 2004–20 mean values. The strongest AMOC/AMHT was observed during the first four years of observations. From April 2008 to March 2012, the AMOC was 2.7 Sv weaker on average than during the first four years of observations (Smeed et al. 2014), and it remained weaker thereafter (Smeed et al. 2018). By combining estimates of the RAPID-MOCHA-WBTS and OSNAP arrays, a time-mean heat divergence of 0.68 ± 0.14 PW during the 2014–18 period has been determined in the extratropical North Atlantic between the two arrays (Li et al. 2021b).

Interannual and longer variability of the AMOC/AMHT at 26.5°N is dominated by changes in the upper-ocean geostrophic flows between the Bahamas and Canary Islands (McCarthy et al. 2012). However, the Florida Current volume transport, which is measured by a submarine cable between Florida and the Bahamas and is part of the AMOC estimate at 26.5°N, has exhibited an intensification of its interannual variability since around 2014 (Dong et al. 2022; Volkov et al. 2020). In 2021, the Florida Current volume transport was 30.8 ± 0.5 Sv, which is slightly below its long-term (1982–2021) mean value of 31.8 ± 0.1 Sv, but not significantly different from the 2020 mean value of 31.2 ± 0.6 Sv.

A new method for combining satellite sea level observations with historical hydrographic measurements (CTD and Argo) and PIES data has been developed and used to derive the AMHT at 34.5°S (Kersalé et al. 2021; red curve in Fig. 3.21d). The average AMHT during 2013–17 was 0.5 ± 0.2 PW, with a peak-to-peak range of 4.6 PW and a daily standard deviation of 0.8 PW. The daily AMHT and AMOC at 34.5°S exhibit a strong positive correlation with the northward transport in the AMOC upper cell (r=0.96; black curve in Fig. 3.21d) and a modest negative correlation

with the southward volume transport in the AMOC abyssal cell (r= −0.52). The AMHT estimate seasonal cycle has a prevailing semi-annual period and a maximum equatorward heat transport in July–September and December–January. The four-year record (2013–17) reveals a weak positive AMHT trend of 0.14 ± 0.18 PW yr^{-1}, not statistically different from zero.

Combination of satellite altimetry and in situ hydrography data provides information on the state of the AMOC/AMHT in 2021. Updated AMOC/AMHT estimates at 41°N (Fig.3.22a), based on satellite altimetry and Argo measurements (Willis 2010; Hobbs and Willis 2012), are about 20% and 25% below their average values in 2021, respectively. The reduction in the AMOC was largely due to a weaker-than-normal upper ocean northward geostrophic transport. The reduction in the

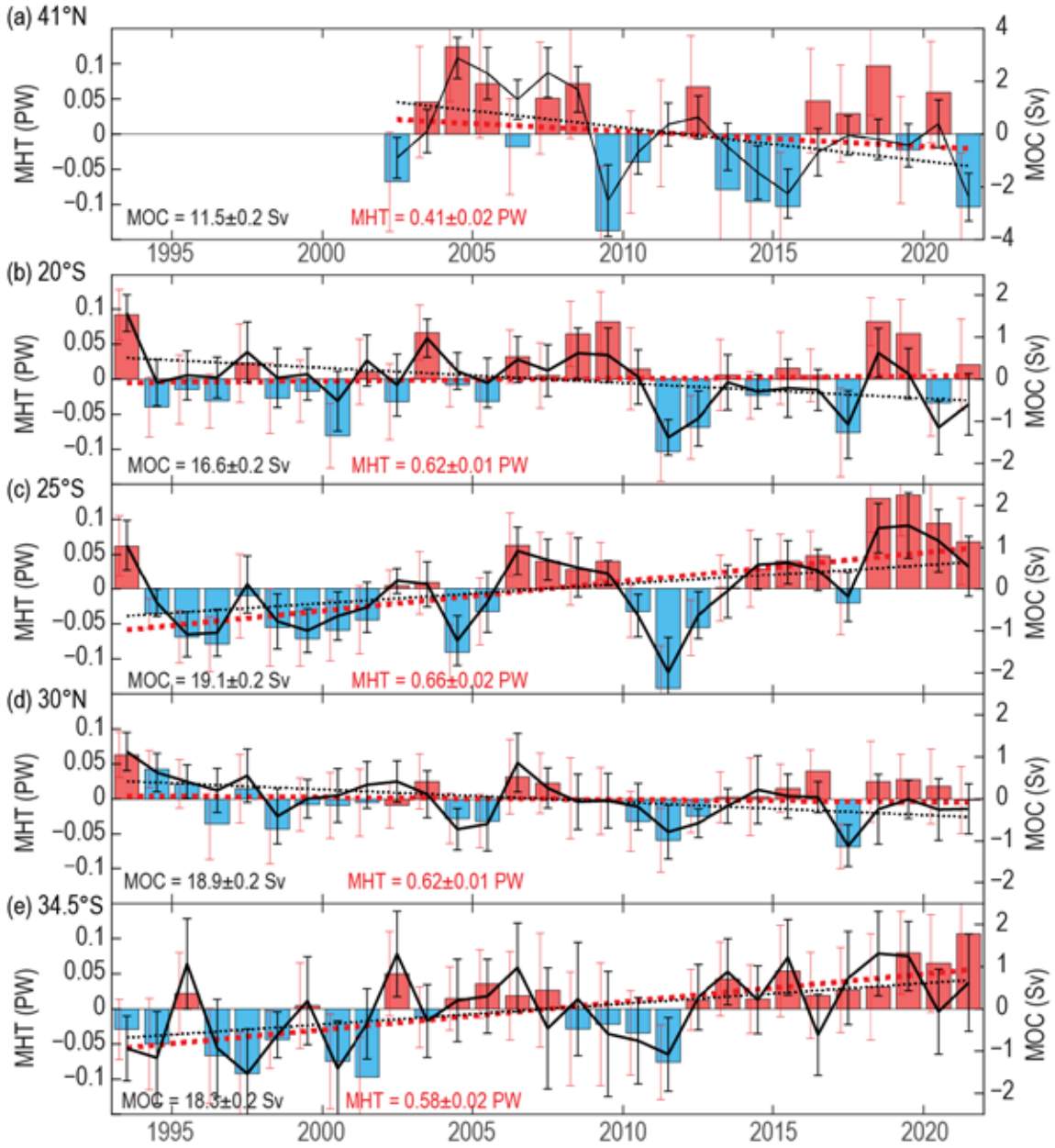

Fig. 3.22. The AMHT (colored bars) and the AMOC (black curves) anomalies obtained by combining satellite altimetry and in situ data at (a) 41°N, (b) 20°S, (c) 25°S, (d) 30°S, and (e) 34.5°S. The vertical error bars show standard errors (red) for the AMHT and (black) for the AMOC. The anomalies are computed with respect to the time-mean values shown in the plots. Linear trends (dashed red lines) for the AMHT are equal to: −0.002 ± 0.010 PW yr^{-1} at 41°N, 0.000 ± 0.003 PW yr^{-1} at 20°S, 0.004 ± 0.003 PW yr^{-1} at 25°S, 0.000 ± 0.002 PW yr^{-1} at 30°S, and 0.004 ± 0.002 PW yr^{-1} at 34.5°S. Linear trends (dashed black lines) for the AMOC are equal to: −0.13 ± 0.14 Sv yr^{-1} at 41°N, −0.04 ± 0.03 Sv yr^{-1} at 20°S, 0.05 ± 0.04 Sv yr^{-1} at 25°S, −0.03 ± 0.02 Sv yr^{-1} at 30°S, and 0.05 ± 0.04 Sv yr^{-1} at 34.5°S. The estimates at 41°N are based on satellite altimetry and Argo data (Willis 2010; Hobbs and Willis 2012), and the estimates at 20°S, 25°S, 30°S, and 34.5°S are based on satellite altimetry and the Global Temperature and Salinity Profile Program data (Dong et al. 2021).

AMHT, however, was due to a southward anomaly in Ekman transport, while the upper ocean geostrophic temperature transport had a positive anomaly. The geostrophic temperature transport anomaly was due to the upper 1000-m temperature. As evidenced by Argo data (not shown), this temperature in 2021 was higher than the 2002–21 average temperature. Therefore, even though there was less upper-ocean northward transport, there was greater net heat transport. It should be noted that these estimates for 2021 are still preliminary and may change after satellite altimetry and Argo data undergo additional validation, quality control, and improvements. Similar to the estimates at 26.5°N (Fig. 3.21c), the AMOC/AMHT at 41°N in 2009–21 were 10–20% lower than they were in 2004–08 without any indication of a rebound. While the AMOC and AMHT trends for 2002–21 are negative at 41°N (−0.13 ± 0.14 Sv yr^{-1} and −0.002 ± 0.009 PW yr^{-1}, respectively), they are not statistically significantly different from zero.

The AMOC/AMHT estimates at 20°S, 25°S, 30°S, and 34.5°S (Figs. 3.22b–e; updated from Dong et al. 2021) based on satellite altimetry and the Global Temperature and Salinity Profile Program (GTSPP; Sun et al. 2010) data were not significantly different from those in 2020. Meaningful positive AMHT trends exist at 25°S (0.004 ± 0.002 PW yr^{-1}) and 34.5°S (0.004 ± 0.003 PW yr^{-1}), while trends at 20°S and 30°S are statistically insignificant. The negative AMOC trends at 20°S and 30°S, and the positive AMOC trends at 25°S and 35°S, are all statistically significant. This result suggests that there is a long-term heat divergence between 30° and 25°S and heat convergence between 34.5° and 30°S and between 25° and 20°S. There is a possible northward propagation of the MHT anomalies in the South Atlantic. For example, mainly positive anomalies in 2003–07, negative anomalies in 2008–12, and positive anomalies 2013–21 at 34.5°S are observed at the lower latitudes about one year later.

In summary, AMOC and AMHT estimates based on moored and blended data continue to show highly variable transports across the Atlantic Ocean. While some of the long-term trends are found to be marginally significant, given the limited observational record, it is not yet possible to conclude that the AMOC is changing in response to climate change. It remains important to reconcile the AMOC and AMHT estimates based on the different methodologies used to compute them. This will help to improve the methodologies and reduce uncertainties in the estimates of oceanic transports. Sustained observations are necessary for detecting and understanding climate-relevant changes in the AMOC.

Sidebar 3.2: **IPCC AR6 assessment of the role of the oceans in the carbon cycle**—R. A. FEELY AND R. WANNINKHOF

The global ocean plays a major role in the global carbon cycle by absorbing a substantial fraction of the excess carbon dioxide (CO_2) that humans release into the atmosphere. As a result of humankind's collective input of CO_2 into the atmosphere, referred to as "anthropogenic CO_2" (C_{anth}) emissions, global average atmospheric CO_2 concentrations have risen from pre-industrial levels of about 278 parts per million (ppm) to ~415 ppm in 2021. The recent IPCC Working Group I contribution to the Sixth Assessment Report provides a comprehensive understanding of the drivers that affect how the carbon cycle in the ocean is changing and the role of human influence (IPCC 2021). Evidence from both global ocean biogeochemical models (GOBMs) and observations provide a "high confidence" that the ocean sink increased from 1.0 ± 0.3 PgC yr^{-1} in 1960–69 to 2.5 ± 0.3 PgC yr^{-1} in 2010–19, with the total cumulative uptake accounting for approximately 23% of the total anthropogenic CO_2 emissions over the entire period (Friedlingstein et al. 2020, 2022). The multi-decadal trends in the ocean carbon air–sea flux show an increase in the ocean sink with a "hiatus" in the 1990s (Fig. SB3.2). The hiatus appears to be associated with either decadal changes in Southern Ocean mixing and circulation processes (Le Quéré et al. 2007; Canadell et al. 2021), external forcing (McKinley et al. 2020), or a combination thereof. Over the last six decades the land and ocean C_{anth} sinks have been roughly consistent with the atmospheric CO_2 increase on decadal scales such that the fraction of anthropogenic CO_2 emissions that has been retained in the atmosphere has remained roughly constant at about 44% over the years.

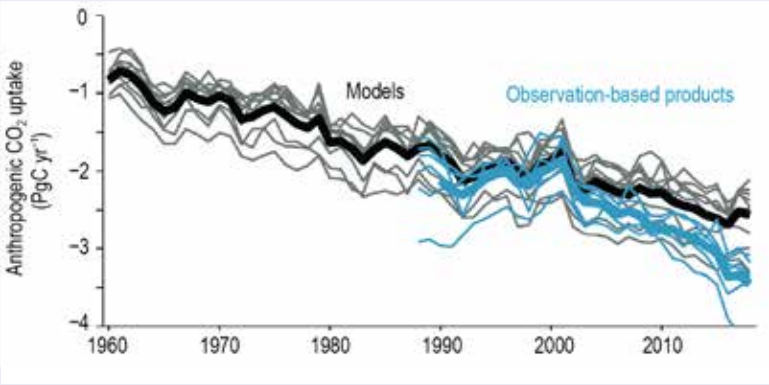

Fig. SB3.2. Comparison of trends for oceanic anthropogenic CO_2 uptake (PgC yr^{-1}) from GOBMs (1960–2018) and observations (1987–2018). The hiatus of the increasing oceanic sink in the 1990s appears to be related to decadal changes in the Southern Ocean (after Canadell et al. 2021).

The uptake of the excess CO_2 by the oceans involves a twofold process in which CO_2 is exchanged across the air–sea interface followed by mixing and transport in the ocean interior where it is stored in deep water masses via mixing and circulation processes on time scales of decades to centuries (DeVries et al. 2017, 2019; Gruber et al. 2019). Both GOBMs and observations indicate that uptake and CO_2 storage mainly occur in the oceanic midlatitude regions, where the mixing and ventilation of subtropical and subpolar surface water contribute to the formation and transport of Mode, Intermediate, and Deep waters that carry the anthropogenic CO_2 into the ocean interior. In contrast, outgassing of CO_2 mostly occurs in areas with upwelling such as eastern boundaries, the equatorial Pacific, and divergence zones in the Southern Ocean. The cumulative amount of anthropogenic CO_2 stored in the ocean interior since the start of the industrial revolution (≈1750) has been estimated to be approximately 170 ± 20 PgC through 2019 (Friedlingstein et al. 2020, 2022). It is anticipated that the ocean sink will continue to increase with increasing anthropogenic emission, but substantial changes to the multi-decadal trends in the ocean sinks are anticipated once these emissions are curtailed.

Different regions have been observed to impact interannual and decadal changes of the CO_2 flux variability in the global oceans. The high latitude (≈>45°) regions, mostly in the Southern Ocean, have the largest influence over the decadal-scale variations due to changes in wind forcing and circulation processes. For example, in the Pacific sector of the Southern Ocean, the rate of anthropogenic CO_2 storage increased from 8.8 ± 1.1 PgC $decade^{-1}$ during 1995–2005 to 11.7 ± 1.1 PgC $decade^{-1}$ during 2005–15 (Carter et al. 2017, 2019). On the other hand, the impact of ENSO in the tropical oceans has caused this portion of the oceans to have the largest influence over the interannual variability (Ishii et al. 2020).

Both observations and models suggest that increases in the seasonal amplitude of surface ocean pCO_2 due to uptake of anthropogenic CO_2 correspond to reductions in the buffering capacity of seawater. This decrease in buffer capacity is starting to have a large-scale impact on the carbonate chemistry of seawater (Fassbender et al. 2018; Landschützer et al. 2018; Jiang et al. 2019). Moreover, model results (Rodgers et al. 2020) suggest that re-emergence of previously stored anthropogenic CO_2 is changing the buffering capacity of the ocean mixed layer and consequently increasing the potential for reducing the ocean sink of C_{anth} over time.

Extensive carbonate chemistry and pH measurements throughout the global ocean have revealed that acidification of the surface ocean has resulted in an overall decline in the rate of pH change in the range of −0.017 to −0.027 $decade^{-1}$ over the last four decades. These rates are consistent with the increase in atmospheric CO_2 and amount to approximately a 4% increase in surface ocean hydrogen ion concentration per decade. The rate of pH decline is slowest in the western Pacific Warm Pool and subtropics (−0.010 to −0.019 $decade^{-1}$) and higher in the upwelling region of the tropical Pacific (−0.022 to −0.026). In the polar and subpolar regions rates of pH decline are more variable (−0.003 to −0.026); however, highly resolved long time series data are sparser there. These changes to the carbonate system result in a declining saturation state from −0.07 to −0.12 $decade^{-1}$ for the biogenic calcium carbonate mineral aragonite, which makes up the skeletal material of many calcifying organisms of economic importance. Within the ocean interior, changes in circulation and metabolic activity have also caused enhanced acidification in the deeper waters of the South Atlantic and North Pacific (Ríos et al. 2015; Sasano et al. 2015). These changes in the acidification of the ocean interior have resulted in a shoaling of the aragonite saturation horizon, where $\Omega_{ar} = 1.0$, ranging from 1–2 m yr^{-1} in the North Pacific (Feely et al. 2012) to as much as 10–15 m yr^{-1} in the Irminger and Iceland Seas (Olafsson et al. 2009; Perez et al. 2018).

i. Global ocean phytoplankton—B. A. Franz, I. Cetinić, M. Gao, D. A. Siegel, and T. K. Westberry

Marine phytoplankton contribute roughly 50% of global net primary production, generating much of the oxygen we breathe and serving the energy needs of oceanic ecosystems, while also providing a critical pathway for carbon sequestration to the deep oceans. The diversity, abundance, and distribution of phytoplankton are controlled by numerous biotic (zooplankton grazing and viruses) and abiotic factors, with the latter including nutrient and light availability that, in turn, are highly dependent on physical properties and processes such as ocean temperature and circulation (e.g., Behrenfeld et al. 2006). Spaceborne radiometers such as SeaWiFS (McClain 2004) and MODIS (Esaias et al. 1998) provide a synoptic view of spatial and temporal changes in phytoplankton, either through measurements of near-surface concentrations of the phytoplankton pigment chlorophyll-*a* (Chl*a*; mg m^{-3}) or phytoplankton carbon (C_{phy}; mg m^{-3}). Measurements of Chl*a* contain information pertaining to both biomass and phytoplankton physiology, while C_{phy} is a direct measurement of phytoplankton biomass. C_{phy} and Chl*a* often covary, but departures from this covariance can indicate changes in the physiological or compositional characteristics of phytoplankton communities (Dierssen 2010; Geider et al. 1997; Siegel et al. 2013; Westberry et al. 2016).

In this report, we evaluate the global distribution of phytoplankton over the one-year period from October 2020 through September 2021 (the analysis year) using remotely sensed Chl*a* and C_{phy} measurements from the continuous 24-year record that combines observations of SeaWiFS (1997–2010) and MODIS on Aqua (MODIS-A, 2002–present). The MODIS-A daytime SST (°C) is also assessed over a consistent time period to provide context on the physical state of the oceans. The Chl*a* product was derived using the Ocean Color Index algorithm of Hu et al. (2012), while C_{phy} was derived from the particle backscattering coefficient, b_{bp}, at 443 nm (Generalized Inherent Optical Properties algorithm; Werdell et al. 2013) and a linear relationship between b_{bp} and C_{phy} as described in Graff et al. (2015). In merging the time series of SeaWiFS and MODIS-A, differences between the sensors were assessed over the overlapping period from 2003 through 2008, and a small bias correction (± 1.8e-3 mg m^{-3} in Chl*a*, ± 4.1e-5 m^{-1} in b_{bp}) was estimated and applied per instrument per variable to ensure continuity.

Variations in the two phytoplankton distribution metrics were evaluated by subtracting monthly climatological means for MODIS-A (October 2002–September 2020) from their monthly mean values of MODIS-A Chl*a* and C_{phy} in the analysis year. These monthly anomalies were then averaged to produce the global Chl*a* and C_{phy} annual mean anomaly maps (Figs. 3.23a,b). Similar calculations were performed on MODIS-A SST data to produce an equivalent SST annual mean anomaly for the same time period (Fig. 3.23c). The permanently stratified ocean (PSO), used for the analysis depicted in Figs. 3.24 and 3.25, is defined as the region, spanning the tropical and subtropical oceans, where annual average SST is greater than 15°C and surface mixed layers are typically low in nutrients and shallower than the nutricline (black lines near 40°N and 40°S in Fig. 3.23; Behrenfeld et al. 2006).

The Chl*a* anomaly distribution for this year (Fig. 3.23a) is characterized by strongly elevated Chla concentrations in a boomerang pattern centered on the western equatorial Pacific, with values exceeding 40% of the climatological mean. This band of elevated chlorophyll sits along the edge of the anomalously low SST waters in the equatorial Pacific (Fig. 3.23c), indicative of the prevailing La Niña conditions during 2021 (see section 4b). In contrast, large regions of anomalously low Chl*a* concentrations (–20%) are observed over much of the North and South Pacific and the southern reaches of the Atlantic, extending to the boundaries of the PSO and beyond. These regions are generally characterized by anomalously warm SST, elevated 0.6° to 0.8°C (Fig. 3.23c). Within the PSO, such positive SST anomalies typically correspond to a shallower surface mixed layer (Deser et al. 2010), which increases effective light exposure of the phytoplankton within that layer and leads to a physiological response of decreased cellular chlorophyll concentration (Behrenfeld et al. 2015). PSO regions are typically nutrient-depleted, leading to further decoupling

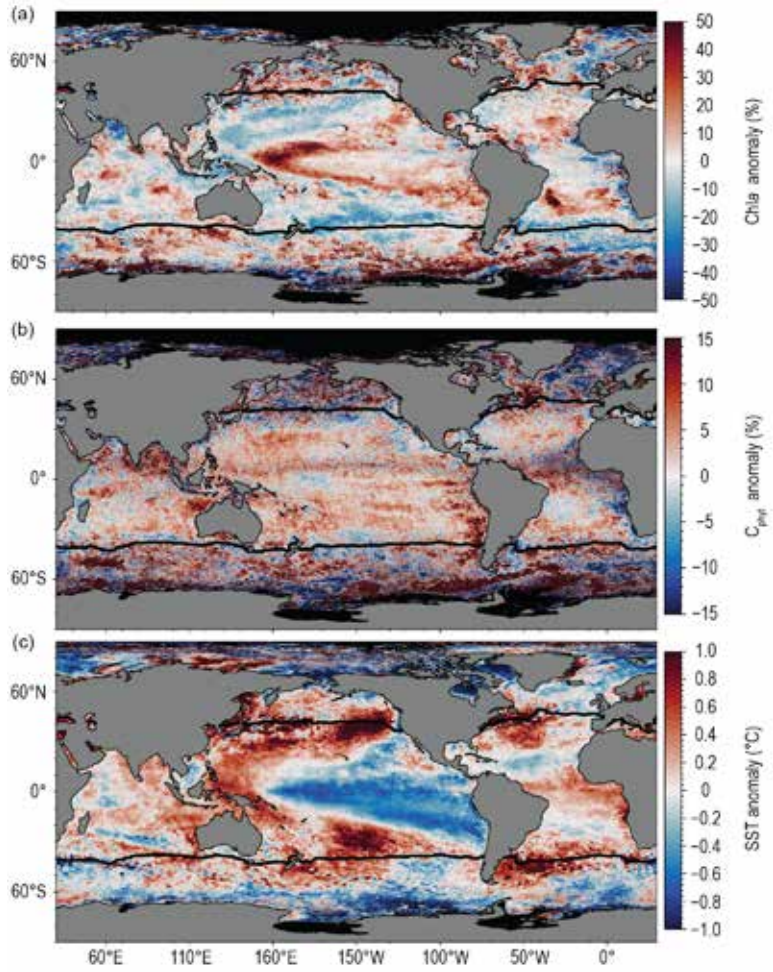

Fig. 3.23. Spatial distribution of average monthly (a) MODIS-A Chl*a* anomalies (%), (b) MODIS-A C_{phy} anomalies (%), and (c) MODIS-A SST anomalies (°C) for Oct 2020–Sep 2021, where monthly differences were derived relative to the MODIS-A 18-year climatological record (Oct 2002–Sep 2020). Chl*a* and C_{phy} are stated as % difference from climatology, while SST is shown as an absolute difference. Also shown in each panel is the location of the mean 15°C SST isotherm (black lines) delineating the permanently stratified ocean (PSO). Differences in the SST anomalies here versus in Fig. 3.1 are owing to differences in climatological periods, smoothing, and data sources.

of Chl*a* and C_{phy} anomalies in these warmer, stratified waters, as a result of further decreased cellular chlorophyll-to-carbon ratios (Westberry et al. 2016). Outside of the PSO, phytoplankton anomalies (Figs. 3.23a,b) showed greater spatial variability, including some large patches of highly elevated (> 50% in Chl*a*) phytoplankton biomass anomalies in the Southern Ocean, especially in the Pacific sector, as well as in the Labrador Sea (> 15 % in C_{phy}). In these higher-latitude, well-mixed waters, Chl*a* and C_{phy} anomalies generally covary, consistent with previous studies (e.g., Franz et al. 2021). The greater spatial variability typically observed poleward of the PSO is expected due to the episodic and intense nature of phytoplankton blooms in these regions, but the relatively poor spatial and temporal sampling at high latitudes due to clouds and low-light conditions also contributes to higher noise in the ocean color signal, thus limiting confidence in the interpretation of interannual changes.

Seasonal changes in phytoplankton biomass in the PSO typically display two annual peaks (Figs. 3.24a,b), reflecting vernal increases in biomass in the Northern (Figs. 3.24c,d) and Southern (Figs. 3.24 g,h) Hemispheres. Peaks in monthly climatological C_{phy} tend to lag peaks in Chl*a* by roughly two to three months, reflecting a reduction in phytoplankton chlorophyll-to-carbon ratios as the seasonal bloom progresses (e.g., Westberry et al. 2016). In 2021, the Northern Hemisphere Chl*a* peak occurred in March–April, followed by C_{phy} maximum in June (Fig. 3.24d), while the Southern Hemisphere peaks for Chl*a* and C_{phy} occurred in September–October and December,

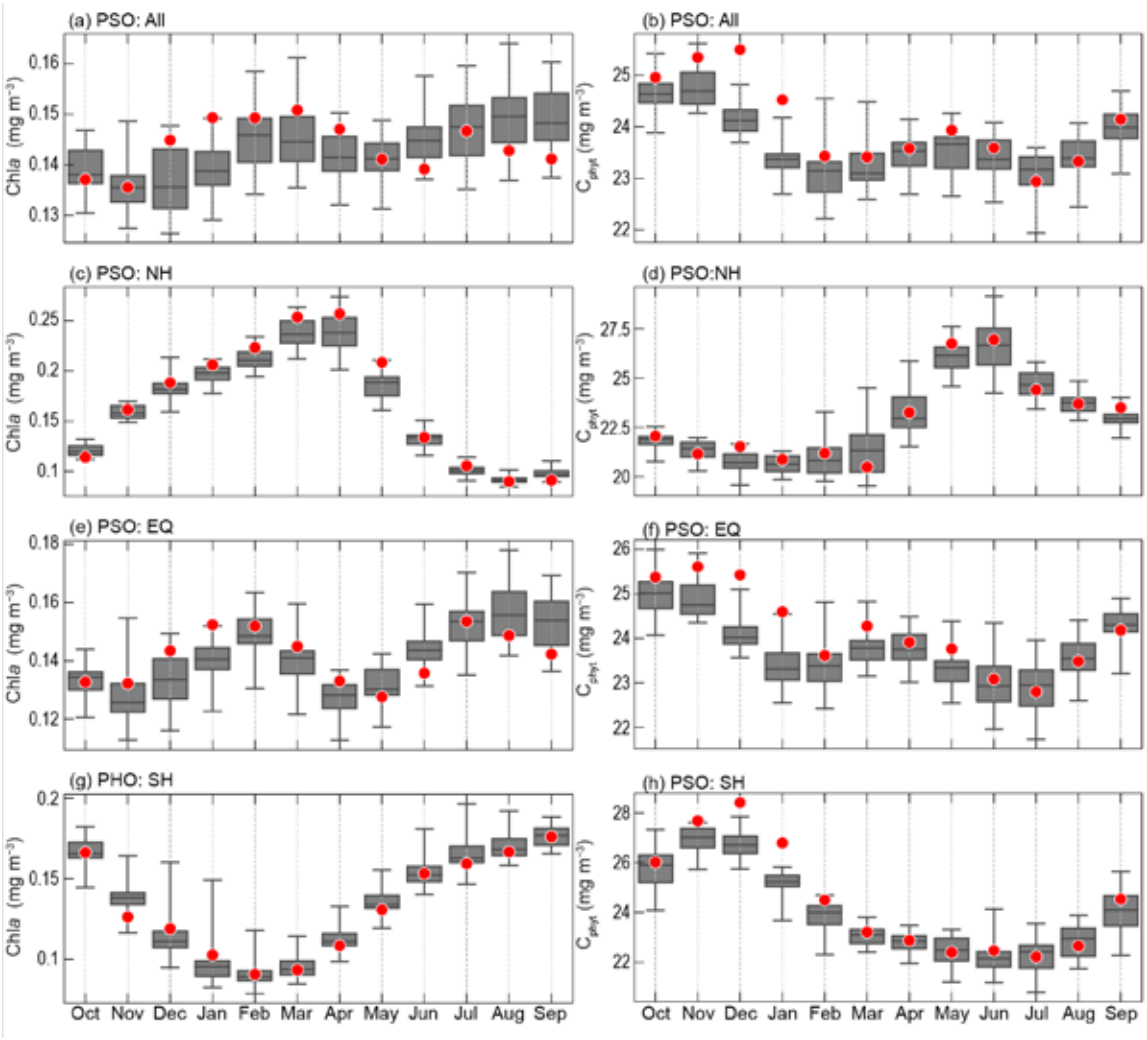

Fig. 3.24. Distribution of Oct 2020–Sep 2021 monthly means (red circles) for (a) MODIS-A Chl*a* and (b) MODIS-A C_{phy} for the permanently stratified ocean (PSO) region (see Fig. 3.23), superimposed on the climatological values as derived from the combined time series of SeaWiFS and MODIS-A over the 23-year period of 1998–2020. Gray boxes show the interquartile range of the climatology, with a black line for the median value and whiskers extending to minimum and maximum values. Subsequent panels show latitudinally segregated subsets of the PSO for the Northern Hemisphere (north of the tropics), NH (c),(d), tropical ±23.5° latitude subregion, EQ (e),(f), and Southern Hemisphere (south of the tropics), SH (g),(h). Units for (a), (c), (e), and (g) are Chl*a* (mg m^{-3}) and (b), (d), (f), and (h) are C_{phy} (mg m^{-3}).

respectively (Figs. 3.24g,h). Generally, monthly mean values of Chl*a* and C_{phy} fell within the range of climatological norms in both hemispheres, with the exception of anomalously high C_{phy} concentrations in the equatorial and Southern Hemisphere regions of the PSO, December to January. In 2021 the largest peak in Chl*a* for the global PSO (February–March) is driven by the vernal increase in the Northern Hemisphere and increased Chl*a* in the equatorial region. In contrast, the dominant peak in global PSO is typically associated with the trend in the Southern Hemisphere, which is the case for C_{phy} this year, but not for Chl*a*.

Over the 24-year time series of spatially averaged monthly mean Chl*a* within the PSO (Fig. 3.25a), concentrations vary by ±15% (±0.02 mg m^{-3}) around a long-term average of 0.142 mg m^{-3} (Fig. 3.25a). This variability includes significant seasonal cycles in Chl*a* distributions and responses to climatic events, as has been observed previously (e.g., Behrenfeld et al. 2006; Franz et al. 2021). C_{phy} over the same 24-year period varies by ±8% (±2 mg m^{-3}) around an average of 23.7 mg m^{-3} (Fig. 3.25c). Seasonal cycles in C_{phy} are more clearly defined than those of Chl*a*, consistent with the assertion that C_{phy} better represents variability of phytoplankton biomass, independent of the confounding influence of physiology.

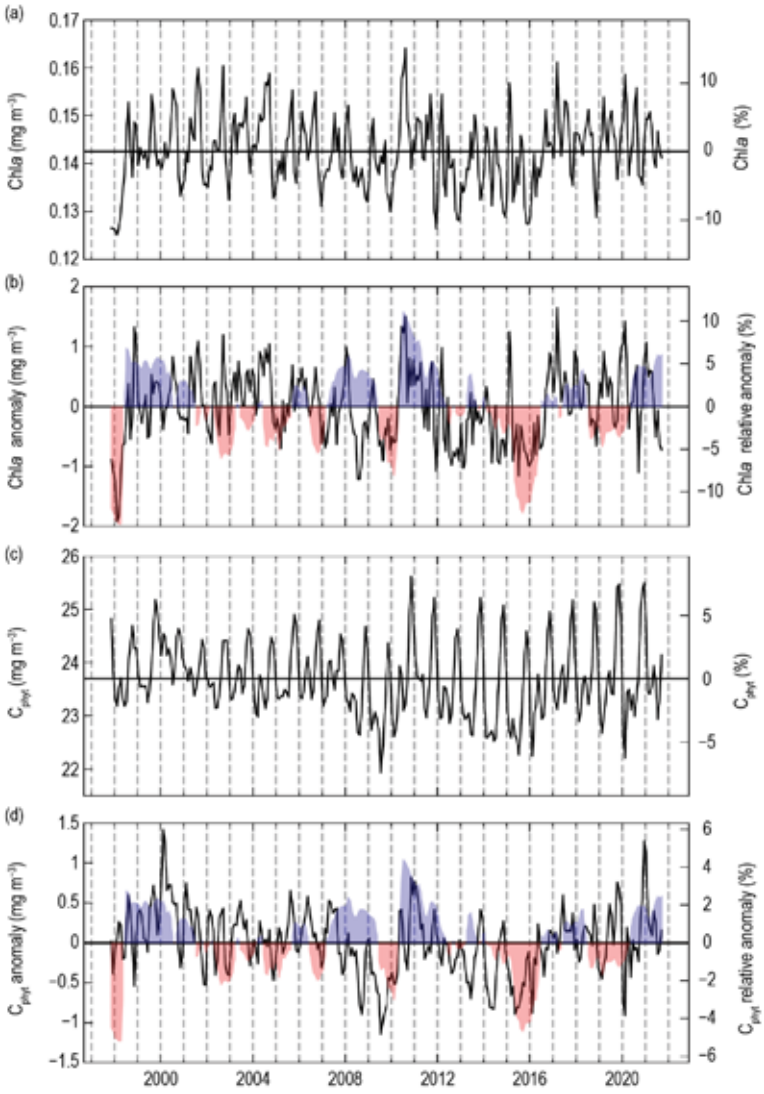

Fig. 3.25. 24-year, multi-mission record of Chl*a* (mg m^{-3}) and C_{phy} (mg m^{-3}) averaged over the PSO. (a) Monthly Chla, with the horizontal line indicating the multi-mission mean Chl*a* concentration for the entire PSO region. (b) Monthly Chl*a* anomalies after subtraction of the 23-year multi-mission climatological mean (Fig. 3.24a). Shaded blue and red colors show the Multivariate ENSO Index, inverted and scaled to match the range of the Chl*a* and C_{phy} anomalies, where blue indicates La Niña conditions and red indicate El Niño conditions.

Chl*a* monthly anomalies within the PSO (Fig. 3.25b) vary by as much as 10% (±0.015 mg m^{-3}) over the multi-mission time series, with the largest deviations generally associated with ENSO events (Pearson correlation coefficient, r = −0.37), as demonstrated by the correspondence of Chl*a* anomaly variations with the Multivariate ENSO Index (MEI; Wolter and Timlin 1998; presented in the inverse to illustrate the covariation). Over the analysis year, monthly Chl*a* anomalies within the PSO varied by ±7%, rising to a peak in January before falling to a minimum at the end of the analysis period. C_{phy} anomalies, which are slightly less correlated with MEI (r = −0.34) due to the inherent lag between environmental change and growth, also peaked in December–January at ~5% or 1.2 mg m^{-3}, reaching one of the highest positive values in our 24-year record (second only to the C_{phy} peak during the La Niña event of 2000). C_{phy} anomalies declined over the remainder of the year, but generally remained positive.

Through the continuous observation of ocean color, we are able to track variability in the global distribution of phytoplankton that drive biogeochemical processes, govern the role of the oceans in the global carbon cycle, and through their productivity exert a controlling influence on marine ecosystems, food webs, and fisheries. Subtle changes in Chl*a* and C_{phy} allow us to distinguish climate driven variability in phytoplankton biomass from changes in physiology and community response. Future satellite missions, such as the upcoming hyperspectral Plankton, Aerosol, Cloud, ocean Ecosystem (PACE) mission, should enable a more precise identification of phytoplankton absorption features (Werdell et al. 2019) and separation of those features from non-algal optical contributions (e.g., Pahlevan et al. 2021; Siegel et al. 2005), and thereby facilitate the assessment of changes in phytoplankton species or community composition (e.g., Kramer et al. 2022; Lange et al. 2020) that will further advance our ability to disentangle the impacts of climate forcing on global phytoplankton communities.

Acknowledgments

- Sandra Bigley provided invaluable editorial support for Chapter 3. Internal reviewers, external reviews, and report editors all provided comments that helped to improve the chapter.
- Argo data used in the chapter were collected and made freely available by the International Argo Program and the national programs that contribute to it. (https://argo.ucsd.edu, https://www.ocean-ops.org). The Argo Program is part of the Global Ocean Observing System. Many authors of the chapter are supported by NOAA Research, the NOAA Global Ocean Monitoring and Observing Program, or the NOAA Ocean Acidification Program.
- L. Cheng is supported by National Natural Science Foundation of China (42076202) and Strategic Priority Research Program of the Chinese Academy of Sciences (XDB42040402).
- R. E. Killick is supported by the Met Office Hadley Centre Climate Programme funded by BEIS and Defra. PMEL contribution numbers 5214, 5215, 5216, 5217, and 5247.

Appendix 1: Chapter 3 – Acronyms

ACC	Antarctic Circumpolar Current
AMOC	Atlantic meridional overturning circulation
AMHT	Atlantic meridional heat transport
BASS	Blended Analysis of Surface Salinity
C_{anth}	anthropogenic CO_2
CERES	Clouds and the Earth's Radiant Energy System
Chl*a*	chlorophyll-*a*
CO_2	carbon dioxide
COARE	Coupled Ocean-Atmosphere Response Experiment
C_{phy}	phytoplankton carbon
DJF	December–February
DOISST	Daily Optimum Interpolation SST version 2.1
E	evaporation
E–*P*	evaporation minus precipitation
EBAF	Energy Balanced and Filled
ENSO	El Niño–Southern Oscillation
ERSSTv5	Extended Reconstruction Sea Surface Temperature version 5
FC	Florida Current
FLASHFlux	Fast Longwave And Shortwave Radiative Fluxes
GMSL	global mean sea level
GPCP	Global Precipitation Climatology Project
GRACE	Gravity Recovery and Climate Experiment
GRACE-FO	Gravity Recovery and Climate Experiment Follow-On
HadSST	Hadley Centre SST
IO	Indian Ocean
IOD	Indian Ocean dipole
ITCZ	Intertropical Convergence Zone
JJA	June–August
LH	latent heat
LW	longwave
MAM	March–May
MEI	Multivariate ENSO Index
MHW	marine heat wave
MOC	meridional overturning circulation
MODIS	Moderate Resolution Imaging Spectroradiometer
MODIS-A	MODIS on *Aqua*
NAC	North Atlantic Current
NECC	North Equatorial Countercurrent
NH	Northern Hemisphere
NPG	North Pacific Gyre
NPP	net primary production
OAFlux	Objectively Analyzed air-sea Fluxes
OHCA	ocean heat content anomaly
OSNAP	Overturning in the Subpolar North Atlantic Program

P	precipitation
PACE	Plankton, Aerosol, Cloud, ocean Ecosystem
P–*E*	precipitation minus evaporation
ppm	parts per million
PSO	permanently stratified ocean
RAPID/MOCHA/WBTS	Rapid Climate Change/MOC and Heatflux Array/Western Boundary Time Series
SAMBA	South Atlantic MOC Basin-wide Array
SEC	South Equatorial Current
SH	sensible heat flux
SH	Southern Hemisphere
SMAP	Soil Moisture Active Passive
SMOS	Soil Moisture and Ocean Salinity
SOCAT	Surface Ocean CO_2 Atlas
SON	September–November
SPCZ	South Pacific Convergence Zone
SSM/I	Special Sensor Microwave/Imager
SSS	sea surface salinity
SST	sea surface temperature
SSTA	sea surface temperature anomaly
std. dev.	standard deviation
SW	shortwave
TRACOS	Tropical Atlantic Circulation and Overturning at 11°S
XBT	eXpendable BathyThermograph

References

Abraham, J. P., and Coauthors, 2013: A review of global ocean temperature observations: Implications for ocean heat content estimates and climate change. *Rev. Geophys.*, **51**, 450–483, https://doi.org/10.1002/rog.20022.

Adler, R. F., and Coauthors, 2018: The Global Precipitation Climatology Project (GPCP) monthly analysis (new version 2.3) and a review of 2017 global precipitation. *Atmosphere*, **9**, 138, https://doi.org/10.3390/atmos9040138.

Babcock, R. C., and Coauthors, 2019: Severe continental-scale impacts of climate change are happening now: Extreme climate events impact marine habitat forming communities along 45% of Australia's coast. *Front. Mar. Sci.*, **6**, 411, https://doi.org/10.3389/fmars.2019.00411

Balaguru, K., P. Chang, R. Saravanan, L. R. Leung, Z. Xu, M. Li, and J. S. Hsieh, 2012: Ocean barrier layers' effect on tropical cyclone intensification. *Proc. Natl. Acad. Sci. USA*, **109**, 142343–142347, https://doi.org/10.1073/pnas.1201364109.

Barnoud, A., and Coauthors, 2021: Contributions of altimetry and Argo to nonclosure of the global mean sea level budget since 2016. *Geophys. Res. Lett.*, **48**, e2021GL092824, https://doi.org/10.1029/2021GL092824.

Baumgartner, A., and E. Reichel, 1975: *The World Water Balance*, Elsevier, 179 pp.

Behrenfeld, M. J., and Coauthors, 2006: Climate-driven trends in contemporary ocean productivity. *Nature*, **444**, 752–755, https://doi.org/10.1038/nature05317.

——, and Coauthors, 2015: Revaluating ocean warming impacts on global phytoplankton. *Nat. Climate Change*, **6**, 323–330, https://doi.org/10.1038/nclimate2838.

Boyer, T. P., and Coauthors, 2018: *World Ocean Database 2018*. A.V. Mishonov, Ed., NOAA Atlas NESDIS 87, 207 pp.

Broecker, W. S., 1991: The Great Ocean Conveyor. *Oceanography*, **4**, 79–89, https://doi.org/10.5670/oceanog.1991.07.

Brown, J. R., and Coauthors, 2020: South Pacific convergence zone dynamics, variability and impacts in a changing climate. *Nat. Rev. Earth Environ.*, **1**, 530–543, https://doi.org/10.1038/s43017-020-0078-2.

Caesar, L., S. Rahmstorf, A. Robinson, G. Feulner, and V. Saba, 2018: Observed fingerprint of a weakening Atlantic Ocean overturning circulation. *Nature*, **556**, 191–196, https://doi.org/10.1038/s41586-018-0006-5.

Canadell, J. G., and Coauthors, 2021: Global carbon and other biogeochemical cycles and feedbacks. *Climate Change 2021: The Physical Science Basis*, V. Masson-Delmotte et al., Eds., Cambridge University Press, 673–816, https://doi.org/10.1017/9781009157896.007.

Carter, B. R., and Coauthors, 2017: Two decades of Pacific anthropogenic carbon storage and ocean acidification along Global 4 Ocean Ship-based Hydrographic Investigations Program sections P16 and P02. *Global Biogeochem. Cycles*, **31**, 306–327, https://doi.org/10.1002/2016GB005485.

——, and Coauthors, 2019: Pacific anthropogenic carbon between 1991 and 2017. Global Biogeochem. Cycles, 33, 102597–102617, https://doi.org/10.1029/2018GB006154.

Castro de la Guardia, L., X. Hu, and P. G. Myers, 2015: Potential positive feedback between Greenland Ice Sheet melt and Baffin Bay heat content on the west Greenland shelf. *Geophys. Res. Lett.*, **42**, 4922–4930, https://doi.org/10.1002/2015GL064626.

Chambers, D. P., A. Cazenave, N. Champollion, H. Dieng, W. Llovel, R. Forsberg, K. von Schuckmann, and Y. Wada, 2017: Evaluation of the global mean sea level budget between 1993 and 2014. *Surv. Geophys.*, **38**, 309–327, https://doi.org/10.1007/s10712-016-9381-3.

Chen, J., B. Tapley, C. Wilson, A. Cazenave, K. W. Seo, and J. S. Kim, 2020: Global ocean mass change from GRACE and GRACE follow-on and altimeter and Argo measurements. *Geophys. Res. Lett.*, **47**, e2020GL090656, https://doi.org/10.1029/2020GL090656.

Cheng, L., J. Zhu, R. Cowley, T. Boyer, and S. Wijffels, 2014: Time, probe type, and temperature variable bias corrections to historical expendable bathythermograph observations. *J. Atmos. Oceanic Technol.*, **31**, 1793–1825, https://doi.org/10.1175/JTECH-D-13-00197.1.

——, and Coauthors, 2020: Record-setting ocean warmth continued in 2019. *Adv. Atmos. Sci.*, **37**, 137–142, https://doi.org/10.1007/s00376-020-9283-7.

Deser, C., M. A. Alexander, S. P. Xie, and A. S. Phillips, 2010: Sea surface temperature variability: Patterns and mechanisms. *Annu. Rev. Mar. Sci.*, **2**, 115–143, https://doi.org/10.1146/annurev-marine-120408-151453.

DeVries, T., M. Holzer, and F. Primeau, 2017: Recent increase in oceanic carbon uptake driven by weaker upper-ocean overturning. *Nature*, **542**, 215–218, https://doi.org/10.1038/nature21068.

——, and Coauthors, 2019: Decadal trends in the ocean carbon sink. *Proc. Natl. Acad. Sci. USA*, **116**, 112646–112651, https://doi.org/10.1073/pnas.1900371116.

Dierssen, H. M., 2010: Perspectives on empirical approaches for ocean color remote sensing of chlorophyll in a changing climate. *Proc. Natl. Acad. Sci. USA*, **107**, 172073–172078, https://doi.org/10.1073/pnas.0913800107.

Dima, M., and G. Lohmann, 2010: Evidence for two distinct modes of large-scale ocean circulation changes over the last century. *J. Climate*, **23**, 5–16, https://doi.org/10.1175/2009JCLI2867.1.

Domingues, R., and Coauthors, 2015: Upper ocean response to Hurricane Gonzalo (2014): Salinity effects revealed by sustained and targeted observations from underwater gliders. *Geophys. Res. Lett.*, **42**, 7131–7138, https://doi.org/10.1002/2015GL065378.

——, M. Baringer, and G. Goni, 2016: Remote sources for year-to-year changes in the seasonality of the Florida Current transport. *J. Geophys. Res. Oceans*, **121**, 7547–7559, https://doi.org/10.1002/2016JC012070.

Dong, S., G. Goni, R. Domingues, F. Bringas, M. Goes, J. Christophersen, and M. Baringer, 2021: Synergy of in-situ and satellite ocean observations in determining meridional heat transport in the Atlantic Ocean. *J. Geophys. Res. Oceans*, **126**, e2020JC017073, https://doi.org/10.1029/2020JC017073.

——, D. L. Volkov, G. Goni, K. Pujiana, F. Tagklis, and M. Baringer, 2022: Remote impact of the equatorial Pacific on Florida Current transport. *Geophys. Res. Lett.*, **49**, e2021GL096944, https://doi.org/10.1029/2021GL096944.

Durack, P. J., and S. E. Wijffels, 2010: Fifty-year trends in global ocean salinities and their relationship to broad-scale warming. *J. Climate*, **23**, 4342–4362, https://doi.org/10.1175/2010JCLI3377.1.

——, ——, and R. J. Matear, 2012: Ocean salinities reveal strong global water cycle intensification during 1950 to 2000. *Science*, **336**, 455–458, https://doi.org/10.1126/science.1212222.

Edwards, T. L., and Coauthors, 2021: Projected land ice contributions to twenty-first-century sea level rise. *Nature*, **593**, 74–82, https://doi.org/10.1038/s41586-021-03302-y.

Esaias, W. E., and Coauthors, 1998: An overview of MODIS capabilities for ocean science observations. *IEEE Trans. Geosci. Remote Sens.*, **36**, 1250–1265, https://doi.org/10.1109/36.701076.

Eyring, V., S. Bony, G. A. Meehl, C. A. Senior, B. Stevens, R. J. Stouffer, and K. E. Taylor, 2016: Overview of the Coupled Model Intercomparison Project Phase 6 (CMIP6) experimental design and organization. *Geosci. Model Dev.*, **9**, 1937–1958, https://doi.org/10.5194/gmd-9-1937-2016.

Ezer, T., and L. P. Atkinson, 2014: Accelerated flooding along the U.S. East Coast: On the impact of sea-level rise, tides, storms, the Gulf Stream, and the North Atlantic Oscillations. *Earth's Future*, **2**, 362–382, https://doi.org/10.1002/2014EF000252.

Fairall, C. W., E. F. Bradley, J. E. Hare, A. A. Grachev, and J. B. Edson, 2003: Bulk parameterization of air–sea fluxes: Updates and verification for the COARE algorithm. *J. Climate*, **16**, 571–591, https://doi.org/10.1175/1520-0442(2003)016<0571:BPOASF>2.0.CO;2.

Fassbender, A. J., K. B. Rodgers, H. I. Palevsky, and C. L. Sabine, 2018: Seasonal asymmetry in the evolution of surface ocean pCO_2 and pH thermodynamic drivers and the influence on sea-air CO_2 flux. *Global Biogeochem. Cycles*, **32**, 1476–1497, https://doi.org/10.1029/2017GB005855.

Fasullo, J. T., and R. S. Nerem, 2018: Altimeter-era emergence of the patterns of forced sea-level rise in climate models and implications for the future. *Proc. Natl. Acad. Sci. USA*, **115**, 122944–122949, https://doi.org/10.1073/pnas.1813233115.

——, ——, and B. Hamlington, 2016: Is the detection of accelerated sea level rise imminent? *Sci. Rep.*, **6**, 31245, https://doi.org/10.1038/srep31245.

Feely, R. A., and Coauthors, 2012: Decadal changes in the aragonite and calcite saturation state of the Pacific Ocean. Global Biogeochem. Cycles, 26, 2011GB004157, https://doi.org/10.1029/2011GB004157.

Ffield, A., 2007: Amazon and Orinoco River plumes and NBC rings: Bystanders or participants in hurricane events? *J. Climate*, **20**, 316–333, https://doi.org/10.1175/JCLI3985.1.

Fofonoff, N. P., and E. L. Lewis, 1979: A practical salinity scale. *J. Oceanogr. Soc. Japan*, **35**, 63–64, https://doi.org/10.1007/BF02108283.

Font, J., and Coauthors, 2013: SMOS first data analysis for sea surface salinity determination. *Int. J. Remote Sens.*, **34**, 3654–3670, https://doi.org/10.1080/01431161.2012.716541.

Fore, A. G., S. H. Yueh, W. Q. Tang, B. W. Stiles, and A. K. Hayashi, 2016: Combined active/passive retrievals of ocean vector wind and sea surface salinity with SMAP. *IEEE Trans. Geosci. Remote Sens.*, **54**, 7396–7404, https://doi.org/10.1109/TGRS.2016.2601486.

Forster, P., and Coauthors, 2021: The Earth's energy budget, climate feedbacks, and climate sensitivity. *Climate Change 2021: The Physical Science Basis*, V. Masson-Delmotte et al., Eds., Cambridge University Press, 923–1054, https://doi.org/10.1017/9781009157896.009.

Fox-Kemper, B., and Coauthors, 2021a: Ocean, cryosphere and sea level change. *Climate Change 2021: The Physical Science Basis*, V. Masson-Delmotte et al. Eds., Cambridge University Press, 1211–1362, https://doi.org/10.1017/9781009157896.011.

——, and Coauthors, 2021b: Ocean, cryosphere and sea level change supplementary material. *Climate Change 2021: The Physical Science Basis*, V. Masson-Delmotte et al. Eds., Cambridge University Press, https://www.ipcc.ch/report/ar6/wg1/, in press.

Frajka-Williams, E., and Coauthors, 2019: Atlantic meridional overturning circulation: Observed transports and variability. *Front. Mar. Sci.*, **6**, 260, https://doi.org/10.3389/fmars.2019.00260.

——, B. I. Moat, D. A. Smeed, D. Rayner, W. E. Johns, M. O. Baringer, D. Volkov, and J. Collins, 2021: Atlantic meridional overturning circulation observed by the RAPID-MOCHA-WBTS (RAPID-Meridional Overturning Circulation and Heatflux Array-Western Boundary Time Series) array at 26N from 2004 to 2020 (v2020.1). British Oceanographic Data Centre, Natural Environment Research Council, accessed 2 December 2021, https://doi.org/10.5285/cc1e34b3-3385-662b-e053-6c86abc03444.

Franz, B. A., I. Cetinic, J. P. Scott, D. A. Siegel, and T. K. Westberry, 2021: Global ocean phytoplankton [in "State of the Climate in 2020"]. *Bull. Amer. Meteor. Soc.*, **102** (8), S179–S193, https://doi.org/10.1175/BAMS-D-21-0083.1.

Friedlingstein, P., and Coauthors, 2020: Global carbon budget 2020. *Earth Syst. Sci. Data*, **12**, 3269–3340, https://doi.org/10.5194/essd-12-3269-2020.

——, and Coauthors, 2022: Global carbon budget 2021. *Earth Syst. Sci. Data*, **14**, 1917–2005, https://doi.org/10.5194/essd-14-1917-2022.

Geider, R. J., H. L. MacIntyre, and T. M. Kana, 1997: Dynamic model of phytoplankton growth and acclimation: Responses of the balanced growth rate and the chlorophyll *a*:carbon ratio to light, nutrient limitation and temperature. *Mar. Ecol. Prog. Ser.*, **148**, 187–200, https://doi.org/10.3354/meps148187.

Gelderloos, R., F. Straneo, and C. A. Katsman, 2012: Mechanisms behind the temporary shutdown of deep convection in the Labrador Sea: Lessons from the great salinity anomaly years 1968–71. *J. Climate*, **25**, 6743–6755, https://doi.org/10.1175/JCLI-D-11-00549.1.

Goni, G. J., and W. E. Johns, 2003: Synoptic study of warm rings in the North Brazil Current retroflection region using satellite altimetry. *Interhemispheric Water Exchange in the Atlantic Ocean*, G. J. Goni, and P. Malanotte-Rizzoli, Eds., Elsevier Oceanography Series, Vol. 68, Elsevier, 335–356, https://doi.org/10.1016/S0422-9894(03)80153-8.

——, and Coauthors, 2009: Applications of satellite-derived ocean measurements to tropical cyclone intensity forecasting. *Oceanography*, **22**, 190–197, https://doi.org/10.5670/oceanog.2009.78.

——, F. Bringas, and P. N. Di Nezio, 2011: Observed low frequency variability of the Brazil Current front. *J. Geophys. Res.*, **116**, C10037, https://doi.org/10.1029/2011JC007198.

Good, S. A., M. J. Martin, and N. A. Rayner, 2013: EN4: Quality controlled ocean temperature and salinity profiles and monthly objective analyses with uncertainty estimates. *J. Geophys. Res. Atmos.*, **118**, 6704–6716, https://doi.org/10.1002/2013JC009067.

Gordon, A. L., 1986: Interocean exchange of thermocline water. *J. Geophys. Res.*, **91**, 5037–5046, https://doi.org/10.1029/JC091iC04p05037.

Gouretski, V., and L. Cheng, 2020: Correction for systematic errors in the global dataset of temperature profiles from mechanical bathythermographs. *J. Atmos. Oceanic Technol.*, **37**, 841–855, https://doi.org/10.1175/JTECH-D-19-0205.1.

Graff, J. R., and Coauthors, 2015: Analytical phytoplankton carbon measurements spanning diverse ecosystems. *Deep-Sea Res. I*, **102**, 16–25, https://doi.org/10.1016/j.dsr.2015.04.006.

Gruber, N., and Coauthors, 2019: The oceanic sink for anthropogenic CO_2 from 1994 to 2007. *Science*, **363**, 1193–1199, https://doi.org/10.1126/science.aau5153.

Hakuba, M. Z., T. Frederikse, and F. W. Landerer, 2021: Earth's energy imbalance from the ocean perspective (2005–2019). *Geophys. Res. Lett.*, **48**, e2021GL093624, https://doi.org/10.1029/2021GL093624.

Hamlington, B. D., J. T. Fasullo, R. S. Nerem, K. Kim, and F. W. Landerer, 2019: Uncovering the pattern of forced sea level rise in the satellite altimeter record. *Geophys. Res. Lett.*, **46**, 4844–4853, https://doi.org/10.1029/2018GL081386.

——, C. G. Piecuch, J. T. Reager, H. Chandanpurkar, T. Frederikse, R. S. Nerem, J. T. Fasullo, and S.-H. Cheon, 2020: Origin of interannual variability in global mean sea level. *Proc. Natl. Acad. Sci. USA*, **117**, 132983–132990, https://doi.org/10.1073/pnas.1922190117.

Han, W., G. A. Meehl, D. Stammer, A. Hu, B. Hamlington, J. Kenigson, H. Palanisamy, and P. Thompson, 2017: Spatial patterns of sea level variability associated with natural internal climate modes. *Surv. Geophys.*, **38**, 217–250, https://doi.org/10.1007/s10712-016-9386-y.

Held, I. M., and B. J. Soden, 2006: Robust responses of the hydrological cycle to global warming. J. Climate, 19, 5686–5699, https://doi.org/10.1175/JCLI3990.1

Hobbs, W. R., and J. K. Willis, 2012: Midlatitude North Atlantic heat transport: A time series based on satellite and drifter data. J. Geophys. Res., 117, C01008, https://doi.org/10.1029/2011JC007039.

Holte, J., L. D. Talley, J. Gilson, and D. Roemmich, 2017: An Argo mixed layer climatology and database. *Geophys. Res. Lett.*, **44**, 5618–5626, https://doi.org/10.1002/2017GL073426.

Hu, C., Z. Lee, and B. A. Franz, 2012: Chlorophyll a algorithms for oligotrophic oceans: A novel approach based on three-band reflectance difference. *J. Geophys. Res.*, **117**, C01011, https://doi.org/10.1029/2011JC007395.

Hu, Z.-Z., A. Kumar, Y. Xue, and B. Jha, 2014: Why were some La Niñas followed by another La Niña? *Climate Dyn.*, **42**, 1029–1042, https://doi.org/10.1007/s00382-013-1917-3.

Huang, B., and Coauthors, 2015: Extended Reconstructed Sea Surface Temperature version 4 (ERSST.v4), Part I. Upgrades and intercomparisons. *J. Climate*, **28**, 911–930, https://doi.org/10.1175/JCLI-D-14-00006.1.

——, and Coauthors, 2017: Extended Reconstructed Sea Surface Temperature version 5 (ERSSTv5), upgrades, validations, and intercomparisons. *J. Climate*, **30**, 8179–8205, https://doi.org/10.1175/JCLI-D-16-0836.1.

——, and Coauthors, 2020: Uncertainty estimates for sea surface temperature and land surface air temperature in NOAAGlobalTemp version 5. *J. Climate*, **33**, 1351–1379, https://doi.org/10.1175/JCLI-D-19-0395.1.

——, C. Liu, V. Banzon, E. Freeman, G. Graham, B. Hankins, T. Smith, and H.-M. Zhang, 2021a: Improvements of the daily optimum interpolation sea surface temperature (DOISST) version 2.1. *J. Climate*, **34**, 2923–2939, https://doi.org/10.1175/JCLI-D-20-0166.1.

——, Z. Wang, X. Yin, A. Arguez, G. Graham, C. Liu, T. Smith, H.-M. Zhang, 2021b: Prolonged marine heatwaves in the Arctic: 1982–2020. *Geophys. Res. Lett.*, **48**, e2021GL095590, https://doi.org/10.1029/2021GL095590.

IPCC, 2013: *Climate Change 2013: The Physical Science Basis*. T. F. Stocker et al., Eds., Cambridge University Press, 1535 pp.

——, 2018: *Global Warming of 1.5°C*. V. Masson-Delmotte et al., Eds., IPCC, 616 pp., https://www.ipcc.ch/sr15/.

——, 2019: *IPCC Special Report on the Ocean and Cryosphere in a Changing Climate*, H.-O. Pörtner et al. Eds., IPCC, 755 pp., https://www.ipcc.ch/srocc/.

——, 2021: *Climate Change 2021: The Physical Science Basis*. V. Masson-Delmotte et al., Eds., Cambridge University Press, 3949 pp., https://doi.org/10.1017/9781009157896.

Ishii, M., Y. Fukuda, S. Hirahara, S. Yasui, T. Suzuki, and K. Sato, 2017: Accuracy of global upper ocean heat content estimation expected from present observational datasets. *SOLA*, **13**, 163–167, https://doi.org/10.2151/sola.2017-030.

——, and Coauthors, 2020: Ocean acidification from below in the tropical Pacific. Global Biogeochem. Cycles, 34, e2019GB006368, https://doi.org/10.1029/2019GB006368.

Jiang, L.-Q., B. R. Carter, R. A. Feely, S. K. Lauvset, and A. Olsen, 2019: Surface ocean pH and buffer capacity: Past, present and future. *Sci. Rep.*, **9**, 18624, https://doi.org/10.1038/s41598-019-55039-4.

Johnson, G. C., and J. M. Lyman, 2012: Sea surface salinity [in "State of the Climate in 2011"]. Bull. Amer. Meteor. Soc., 93 (7), S68–S69, https://doi.org/10.1175/2012BAMSStateoftheClimate.1.

——, and ——, 2020: Warming trends increasingly dominate Global Ocean. *Nat. Climate Change*, **10**, 757–761, https://doi.org/10.1038/s41558-020-0822-0.

——, ——, J. K. Willis, T. Boyer, J. Antonov, S. A. Good, C. M. Domingues, and N. Bindoff, 2014: Ocean heat content [in "State of the Climate in 2013"]. *Bull. Amer. Meteor. Soc.*, **95** (7), S54–S57, https://doi.org/10.1175/2014BAMSStateoftheClimate.1.

——, and Coauthors, 2015: Ocean heat content [in "State of the Climate in 2014"]. Bull. Amer. Meteor. Soc., 96 (7), S64–S66, https://doi.org/10.1175/2015BAMSStateoftheClimate.1.

——, and Coauthors, 2021: Ocean heat content [in "State of the Climate in 2020"]. *Bull. Amer. Meteor. Soc.*, **102** (8), S156–S159, https://doi.org/10.1175/BAMS-D-21-0083.1.

Josey, S. A., and Coauthors, 2018: The recent Atlantic cold anomaly: Causes, consequences, and related phenomena. *Annu. Rev. Mar. Sci.*, **10**, 475–501, https://doi.org/10.1146/annurev-marine-121916-063102.

Kato, S., and Coauthors, 2018: Surface irradiances of edition 4.0 clouds and the Earth's Radiant Energy System (CERES) energy balanced and filled (EBAF) data product. J. Climate, 31, 4501–4527, https://doi.org/10.1175/JCLI-D-17-0523.1.

Kennedy, J. J., 2013: A review of uncertainty in in situ measurements and data sets of sea-surface temperature. *Rev. Geophys.*, **51**, 1–32, https://doi.org/10.1002/2013RG000434.

——, N. A. Rayner, C. P. Atkinson, and R. E. Killick, 2019: An ensemble data set of sea surface temperature change from 1850: The Met Office Hadley Centre HadSST.4.0.0.0 data set. *J. Geophys. Res. Atmos.*, **124**, 7719–7763, https://doi.org/10.1029/2018JD029867.

Kent, E. C., and Coauthors, 2017: A call for new approaches to quantifying biases in observations of sea surface temperature. *Bull. Amer. Meteor. Soc.*, **98**, 1601–1616, https://doi.org/10.1175/BAMS-D-15-00251.1.

Kersalé, M., and Coauthors, 2021: Multi-year estimates of daily heat transport by the Atlantic meridional overturning circulation at 34.5°S. J. Geophys. Res. Oceans, 126, e2020JC016947, https://doi.org/10.1029/2020JC016947.

Kramer, S. J., D. A. Siegel, S. Maritorena, and D. Catlett, 2022: Modeling surface ocean phytoplankton pigments from hyperspectral remote sensing reflectance on global scales. *Remote Sens. Environ.*, **270**, 112879, https://doi.org/10.1016/j.rse.2021.112879.

Landschützer, P., N. Gruber, D. C. E. Bakker, I. Stemmler, and K. D. Six, 2018: Strengthening seasonal marine CO_2 variations due to increasing atmospheric CO_2. *Nat. Climate Change*, **8**, 146–150, https://doi.org/10.1038/s41558-017-0057-x.

Lange, P. K., and Coauthors, 2020: Radiometric approach for the detection of picophytoplankton assemblages across oceanic fronts. *Opt. Express*, **28**, 252682–252705, https://doi.org/10.1364/OE.398127.

Laufkötter, C., J. Zscheischler, and T. L. Frölicher, 2020: High-impact marine heatwaves attributable to human-induced global warming. *Science*, **369**, 1621–1625, https://doi.org/10.1126/science.aba0690.

Le Quéré, C., and Coauthors, 2007: Saturation of the Southern Ocean CO_2 sink due to recent climate change. *Science*, **316**, 1735–1738, https://doi.org/10.1126/science.1136188.

Leuliette, E. W., and J. K. Willis, 2011: Balancing the sea level budget. *Oceanography*, **24**, 122–129, https://doi.org/10.5670/oceanog.2011.32.

Le Vine, D. M., E. P. Dinnat, G. S. E. Lagerloef, P. de Matthaeis, S. Abraham, C. Utku, and H. Kao, 2014: Aquarius: Status and recent results. *Radio Sci.*, **49**, 709–720, https://doi.org/10.1002/2014RS005505.

Levitus, S., and Coauthors, 2012: World ocean heat content and thermosteric sea level change (0–2000 m), 1955–2010. *Geophys. Res. Lett.*, **39**, L10603, https://doi.org/10.1029/2012GL051106.

Li, F., and Coauthors, 2021a: Subpolar North Atlantic western boundary density anomalies and the meridional overturning circulation. *Nat. Commun.*, **12**, 3002, https://doi.org/10.1038/s41467-021-23350-2.

——, and Coauthors, 2021b: Observation-based estimates of heat and freshwater exchanges from the subtropical North Atlantic to the Arctic. *Prog. Oceanogr.*, **197**, 102640, https://doi.org/10.1016/j.pocean.2021.102640.

Li, X., Z.-Z. Hu, and B. Huang, 2020: Subannual to interannual variabilities of SST in the North Atlantic Ocean. *J. Climate*, **33**, 5547–5564, https://doi.org/10.1175/JCLI-D-19-0556.1.

——, ——, Y.-H. Tseng, Y. Liu, and P. Liang, 2022: A historical perspective of the La Niña event in 2020/21. *J. Geophys. Res. Atmos.*, 127, e2021JD035546, https://doi.org/10.1029/2021JD035546.

Llovel, W., and L. Terray, 2016: Observed southern upper-ocean warming over 2005–2014 and associated mechanisms. *Environ. Res. Lett.*, **11**, 124023, https://doi.org/10.1088/1748-9326/11/12/124023.

Loeb, N. G., and Coauthors, 2018: Clouds and the Earth's Radiant Energy System (CERES) Energy Balanced and Filled (EBAF) Top-of-Atmosphere (TOA) edition-4.0 data product. *J. Climate*, **31**, 895–918, https://doi.org/10.1175/JCLI-D-17-0208.1.

——, G. C. Johnson, T. J. Thorsen, J. M. Lyman, F. G. Rose, and S. Kato, 2021: Satellite and ocean data reveal marked increase in Earth's heating rate. *Geophys. Res. Lett.*, **48**, e2021GL093047, https://doi.org/10.1029/2021GL093047.

Lozier, M. S., and Coauthors, 2017: Overturning in the subpolar North Atlantic program: A new international ocean observing system. *Bull. Amer. Meteor. Soc.*, **98**, 737–752, https://doi.org/10.1175/BAMS-D-16-0057.1.

——, and Coauthors, 2019: A sea change in our view of overturning in the subpolar North Atlantic. *Science*, **363**, 516–521, https://doi.org/10.1126/science.aau6592.

Lumpkin, R., and S. L. Garzoli, 2005: Near-surface circulation in the tropical Atlantic Ocean. *Deep-Sea Res. I*, **52**, 495–518, https://doi.org/10.1016/j.dsr.2004.09.001.

——, and ——, 2011: Interannual to decadal changes in the western South Atlantic's surface circulation. *J. Geophys. Res.*, **116**, C01014, https://doi.org/10.1029/2010JC006285.

——, G. Goni, and K. Dohan, 2012: Surface currents [in "State of the Climate in 2011"]. Bull. Amer. Meteor. Soc., 93 (7), S75–S78, https://doi.org/10.1175/2012BAMSStateoftheClimate.1.

Lyman, J. M., and G. C. Johnson, 2014: Estimating global ocean heat content changes in the upper 1800 m since 1950 and the influence of climatology choice. *J. Climate*, **27**, 1946–1958, https://doi.org/10.1175/JCLI-D-12-00752.1.

Mantua, N. J., and S. R. Hare, 2002: The Pacific decadal oscillation. *J. Oceanogr.*, **58**, 35–44, https://doi.org/10.1023/A:1015820616384.

Marti, F., and Coauthors, 2022: Monitoring the ocean heat content change and the Earth energy imbalance from space altimetry and space gravimetry. *Earth Syst. Sci. Data*, **14**, 229–249, https://doi.org/10.5194/essd-14-229-2022.

McCarthy, G., and Coauthors, 2012: Observed interannual variability of the Atlantic Meridional Overturning Circulation at 26.5°N. *Geophys. Res. Lett.*, **39**, L19609, https://doi.org/10.1029/2012GL052933.

McClain, C. R., C. R. McClain, G. C. Feldman, and S. B. Hooker, 2004: An overview of the SeaWiFS Project and strategies for producing a climate research quality global ocean bio-optical time series. *Deep-Sea Res. II*, **51**, 5–42, https://doi.org/10.1016/j.dsr2.2003.11.001.

McKinley, G. A., A. R. Fay, Y. A. Eddebbar, L. Gloege, and N. S. Lovenduski, 2020: External forcing explains recent decadal variability of the ocean carbon sink. AGU Adv., 1, e2019AV000149, https://doi.org/10.1029/2019AV000149.

Merrifield, M., 2011: A shift in western tropical Pacific sea level trends during the 1990s. *J. Climate*, **24**, 4126–4138, https://doi.org/10.1175/2011JCLI3932.1.

Nerem, R. S., B. D. Beckley, J. T. Fasullo, B. D. Hamlington, D. Masters, and G. T. Mitchum, 2018: Climate-change-driven accelerated sea-level rise detected in the altimeter era. *Proc. Natl. Acad. Sci. USA*, **115**, 2022–2025, https://doi.org/10.1073/pnas.1717312115.

Okumura, Y. M., and C. Deser, 2010: Asymmetry in the duration of El Niño and La Niña. *J. Climate*, **23**, 5826–5843, https://doi.org/10.1175/2010JCLI3592.1.

Olafsson, J., S. R. Olafsdottir, A. Benoit-Cattin, M. Danielsen, T. S. Arnarson, and T. Takahashi, 2009: Rate of Iceland Sea acidification from time series measurements. *Biogeosciences*, **6**, 2661–2668, https://doi.org/10.5194/bg-6-2661-2009.

Oliver, E. C., J. A. Benthuysen, N. L. Bindoff, A. J. Hobday, N. J. Holbrook, C. N. Mundy, and S. E. Perkins-Kirkpatrick, 2017: The unprecedented 2015/16 Tasman Sea marine heatwave. *Nat. Commun.*, **8**, 16101, https://doi.org/10.1038/ncomms16101.

Pahlevan, N., B. Smith, C. Binding, D. Gurlin, L. Li, M. Bresciani, and C. Giardino, 2021: Hyperspectral retrievals of phytoplankton absorption and chlorophyll-a in inland and nearshore coastal waters. *Remote Sens. Environ.*, **253**, 112200, https://doi.org/10.1016/j.rse.2020.112200.

Palmer, M. D., K. Haines, S. F. B. Tett, and T. J. Ansell, 2007: Isolating the signal of ocean global warming. *Geophys. Res. Lett.*, **34**, L23610, https://doi.org/10.1029/2007GL031712.

——, G. R. Harris, and J. M. Gregory, 2018: Extending CMIP5 projections of global mean temperature change and sea level rise due to thermal expansion using a physically-based emulator. *Environ. Res. Lett.*, **13**, 084003, https://doi.org/10.1088/1748-9326/aad2e4.

Perez, F. F., and Coauthors, 2018: Meridional overturning circulation conveys fast acidification to the deep Atlantic Ocean. *Nature*, **554**, 515–518, https://doi.org/10.1038/nature25493.

Perkins-Kirkpatrick, S. E., A. D. King, E. A. Cougnon, N. J. Holbrook, M. R. Grose, E. C. J. Oliver, S. C. Lewis, and F. Pourasghar, 2019: The role of natural variability and anthropogenic climate change in the 2017/18 Tasman Sea marine heatwave. *Bull. Amer. Meteor. Soc.*, **100**, S105–S110, https://doi.org/10.1175/BAMS-D-18-0116.1.

Purkey, S. G., and G. C. Johnson, 2010: Warming of global abyssal and deep Southern Ocean waters between the 1990s and 2000s: Contributions to global heat and sea level rise budgets. *J. Climate*, **23**, 6336–6351, https://doi.org/10.1175/2010JCLI3682.1.

Reagan, J., T. Boyer, C. Schmid, and R. Locarnini, 2020: Subsurface salinity [in "State of the Climate in 2019"]. *Bull. Amer. Meteor. Soc.*, **101** (8), S144–S148, https://doi.org/10.1175/2020BAMSStateoftheClimate.1.

——, ——, ——, and ——, 2021: Subsurface salinity [in "State of the Climate in 2020"]. *Bull. Amer. Meteor. Soc.*, **102** (8), S162–S164, https://doi.org/10.1175/BAMS-D-21-0083.1.

Ren, L., K. Speer, and E. P. Chassignet, 2011: The mixed layer salinity budget and sea ice in the Southern Ocean. *J. Geophys. Res.*, **116**, C08031, https://doi.org/10.1029/2010JC006634.

Ríos, A. F., and Coauthors, 2015: Decadal acidification in the water masses of the Atlantic Ocean. *Proc. Natl. Acad. Sci. USA*, **112**, 9950–9955, https://doi.org/10.1073/pnas.1504613112.

Riser, S. C., and Coauthors, 2016: Fifteen years of ocean observations with the global Argo array. *Nat. Climate Change*, **6**, 145–153, https://doi.org/10.1038/nclimate2872.

Rodgers, K. B., and Coauthors, 2020: Reemergence of anthropogenic carbon into the ocean's mixed layer strongly amplifies transient climate sensitivity. *Geophys. Res. Lett.*, **47**, e2020GL089275, https://doi.org/10.1029/2020GL089275.

Roemmich, D., and J. Gilson, 2009: The 2004–2008 mean and annual cycle of temperature, salinity, and steric height in the global ocean from the Argo Program. *Prog. Oceanogr.*, **82**, 81–100, https://doi.org/10.1016/j.pocean.2009.03.004.

——, and Coauthors, 2019: On the future of Argo: A global, full-depth, multi-disciplinary array. *Front. Mar. Sci.*, **6**, 439, https://doi.org/10.3389/fmars.2019.00439.

Saji, N. H., B. N. Goswami, P. N. Vinayachandran, and T. Yamagata, 1999: A dipole mode in the tropical Indian Ocean. *Nature*, **401**, 360–363, https://doi.org/10.1038/43854.

Sasano, D., Y. Takatani, N. Kosugi, T. Nakano, T. Midorikawa, and M. Ishii, 2015: Multidecadal trends of oxygen and their controlling factors in the western North Pacific. *Global Biogeochem. Cycles*, **29**, 935–956, https://doi.org/10.1002/2014GB005065.

Scannell, H. A., G. C. Johnson, L. Thompson, J. M. Lyman, and S. C. Riser, 2020: Subsurface evolution and persistence of marine heatwaves in the Northeast Pacific. *Geophys. Res. Lett.*, **47**, e2020GL090548, https://doi.org/10.1029/2020GL090548.

Schlesinger, M. E., and N. Ramankutty, 1994: An oscillation in the global climate system of period 65–70 years. *Nature*, **367**, 723–726, https://doi.org/10.1038/367723a0.

Schmidtko, S., K. J. Heywood, A. F. Thompson, and S. Aoki, 2014: Multidecadal warming of Antarctic waters. *Science*, **346**, 1227–1231, https://doi.org/10.1126/science.1256117.

Schmitt, R. W., 1995: The ocean component of the global water cycle. *Rev. Geophys.*, **33**, 1395–1409, https://doi.org/10.1029/95RG00184.

Sherwood, S. C., and Coauthors, 2020: An assessment of Earth's climate sensitivity using multiple lines of evidence. Rev. Geophys., 58, e2019RG000678, https://doi.org/10.1029/2019RG000678.

Siegel, D. A., S. Maritorena, N. B. Nelson, M. J. Behrenfeld, and C. R. McClain, 2005: Colored dissolved organic matter and its influence on the satellite-based characterization of the ocean biosphere. *Geophys. Res. Lett.*, **32**, L20605, https://doi.org/10.1029/2005GL024310.

——, and Coauthors, 2013: Regional to global assessments of phytoplankton dynamics from the SeaWiFS mission. *Remote Sens. Environ.*, **135**, 77–91, https://doi.org/10.1016/j.rse.2013.03.025.

Skliris, N., R. Marsh, S. A. Josey, S. A. Good, C. Liu, and R. P. Allan, 2014: Salinity changes in the World Ocean since 1950 in relation to changing surface freshwater flux. *Climate Dyn.*, **43**, 709–736, https://doi.org/10.1007/s00382-014-2131-7.

——, J. D. Zika, G. Nurser, S. A. Josey, and R. Marsh, 2016: Global water cycle amplifying at less than the Clausius-Clapeyron rate. *Sci. Rep.*, **6**, 38752, https://doi.org/10.1038/srep38752.

Smeed, D. A., and Coauthors, 2014: Observed decline of the Atlantic meridional overturning circulation 2004–2012. *Ocean Sci.*, **10**, 29–38, https://doi.org/10.5194/os-10-29-2014.

——, and Coauthors, 2018: The North Atlantic Ocean is in a state of reduced overturning. *Geophys. Res. Lett.*, **45**, 1527–1533, https://doi.org/10.1002/2017GL076350.

Smith, C., Z. R. J. Nicholls, K. Armour, W. Collins, P. Forster, M. Meinshausen, M. D. Palmer, and M. Watanabe, 2021: The Earth's energy budget, climate feedbacks, and climate sensitivity supplementary material. *Climate Change 2021: The Physical Science Basis*, V. Masson-Delmotte et al., Eds., Cambridge University Press, https://www.ipcc.ch/report/ar6/wg1/, in press.

Smith, R. S., and J. M. Gregory, 2009: A study of the sensitivity of ocean overturning circulation and climate to freshwater input in different regions of the North Atlantic. *Geophys. Res. Lett.*, **36**, L15701, https://doi.org/10.1029/2009GL038607.

Stackhouse, P. W., D. P. Kratz, G. R. McGarragh, S. K. Gupta, and E. B. Geier, 2006: Fast Longwave and Shortwave Flux (FLASHFlux) products from CERES and MODIS measurements. *12th Conf. on Atmospheric Radiation*, Amer. Meteor. Soc., Madison, WI, P1.10, https://ams.confex.com/ams/Madison2006/techprogram/paper_113479.htm.

Stouffer, R. J., and Coauthors, 2006: Investigating the causes of the response of the thermohaline circulation to past and future climate changes. *J. Climate*, **19**, 1365–1387, https://doi.org/10.1175/JCLI3689.1.

Sun, C., and Coauthors, 2010: The data management system for the global temperature and salinity profile programme. *Proc. OceanObs'09: Sustained Ocean Observations and Information for Society*, Vol. 2, J. Hall, D. E. Harrison, and D. Stammer, Eds., ESA Publ.WPP-306, https://doi.org/10.5270/OceanObs09.cwp.86.

Sweet, W.V., J. Park, J. J. Marra, C. Zervas, and S. Gill, 2014: Sea level rise and nuisance flood frequency changes around the United States. NOAA Tech. Rep. NOS CO-OPS 073, 58 pp., https://tidesandcurrents.noaa.gov/publications/NOAA_Technical_Report_NOS_COOPS_073.pdf.

Volkov, D. L., S.-K. Lee, F. W. Landerer, and R. Lumpkin, 2017: Decade-long deep-ocean warming detected in the subtropical South Pacific. *Geophys. Res. Lett.*, **44**, 927–936, https://doi.org/10.1002/2016GL071661.

——, R. Domingues, C. S. Meinen, R. Garcia, M. Baringer, G. Goni, and R. H. Smith, 2020: Inferring Florida current volume transport from satellite altimetry. J. Geophys. Res. Oceans, 125, e2020JC016763, https://doi.org/10.1029/2020JC016763.

——, and Coauthors, 2021: Meridional overturning circulation and heat transport in the Atlantic Ocean [in "State of the Climate in 2020"]. *Bull. Amer. Meteor. Soc.*, **102** (8), S176–S179, https://doi.org/10.1175/BAMS-D-21-0083.1.

von Schuckmann, K., J.-B. Sallée, D. Chambers, P.-Y. Le Traon, C. Cabanes, F. Gaillard, S. Speich, and M. Hamon, 2014: Consistency of the current global ocean observing systems from an Argo perspective. *Ocean Sci.*, **10**, 547–557, https://doi.org/10.5194/os-10-547-2014.

Von Storch, H., and F. W. Zwiers, 1999: *Statistical Analysis in Climate Research*. Cambridge University Press, 484 pp..

Wang, J., and B. Yang, 2017: Internal and external forcing of multidecadal Atlantic climate variability over the past 1,200 years. *Nat. Geosci.*, **10**, 512–517, https://doi.org/10.1038/ngeo2962.

Werdell, P. J., and Coauthors, 2013: Generalized ocean color inversion model for retrieving marine inherent optical properties. *Appl. Opt.*, **52**, 2019–2037, https://doi.org/10.1364/AO.52.002019.

——, and Coauthors, 2019: The Plankton, Aerosol, Cloud, Ocean Ecosystem mission: Status, science, advances. *Bull. Amer. Meteor. Soc.*, **100**, 1775–1794, https://doi.org/10.1175/BAMS-D-18-0056.1.

Westberry, T. K., and Coauthors, 2016: Annual cycles of phytoplankton biomass in the subarctic Atlantic and Pacific Ocean. *Global Biogeochem. Cycles*, **30**, 175–190, https://doi.org/10.1002/2015GB005276.

Willis, J. K., 2010: Can in situ floats and satellite altimeters detect long-term changes in Atlantic Ocean overturning? *Geophys. Res. Lett.*, **37**, L06602, https://doi.org/10.1029/2010GL042372.

——, D. Roemmich, and B. Cornuelle, 2004: Interannual variability in upper ocean heat content, temperature, and thermosteric expansion on global scales. *J. Geophys. Res.*, **109**, C12036, https://doi.org/10.1029/2003JC002260.

Wolter, K., and M. S. Timlin, 1998: Measuring the strength of ENSO events: How does 1997/98 rank? *Weather*, **53**, 315–324, https://doi.org/10.1002/j.1477-8696.1998.tb06408.x.

Wu, L. X., and Coauthors, 2012: Enhanced warming over the global subtropical western boundary currents. *Nat. Climate Change*, **2**, 161–166, https://doi.org/10.1038/nclimate1353.

Wüst, G., 1936: Oberflächensalzgehalt, Verdunstung und Niederschlag auf dem Weltmeere. *Länderkundliche Forschung: Festschrift zur Vollendung des sechzigsten Lebensjahres Norbert Krebs*, J. Engelhorns Nachfahren, 347–359.

Xie, P., and Coauthors, 2014: An in situ-satellite blended analysis of global sea surface salinity. *J. Geophys. Res. Oceans*, **119**, 6140–6160, https://doi.org/10.1002/2014JC010046.

Yang, H., G. Lohmann, W. Wei, M. Dima, M. Ionita, and J. Liu, 2016: Intensification and poleward shift of subtropical western boundary currents in a warming climate. *J. Geophys. Res. Oceans*, **121**, 4928–4945, https://doi.org/10.1002/2015JC011513.

Yu, L., 2011: A global relationship between the ocean water cycle and near-surface salinity. *J. Geophys. Res.*, **116**, C10025, https://doi.org/10.1029/2010JC006937.

——, and R. A. Weller, 2007: Objectively analyzed air–sea heat fluxes for the global ice-free oceans (1981–2005). *Bull. Amer. Meteor. Soc.*, **88**, 527–540, https://doi.org/10.1175/BAMS-88-4-527.

Zebiak, S. E., 1993: Air-sea interaction in the equatorial Atlantic region. *J. Climate*, **6**, 1567–1568, https://doi.org/10.1175/1520-0442(1993)006<1567:AIITEA>2.0.CO;2.

Zhang, R., and Coauthors, 2019: A review of the role of the Atlantic meridional overturning circulation in Atlantic multidecadal variability and associated climate impacts. *Rev. Geophys.*, **57**, 316–375, https://doi.org/10.1029/2019RG000644.

Zweng, M. M., and Coauthors, 2018: *Salinity. Vol. 2, World Ocean Atlas 2018*, NOAA Atlas NESDIS 82, 50 pp., https://data.nodc.noaa.gov/woa/WOA18/DOC/woa18_vol2.pdf.